

















## A Comprehensive Reanalysis of K2-18 b’s JWST NIRISS+NIRSpec Transmission Spectrum

STEPHEN P. SCHMIDT <sup>1,\*</sup> RYAN J. MACDONALD <sup>2,†</sup> SHANG-MIN TSAI <sup>3</sup> MICHAEL RADICA <sup>4,5,‡</sup>  
LE-CHRIS WANG <sup>1</sup> EVA-MARIA AHRER <sup>6</sup> TAYLOR J. BELL <sup>7</sup> CHLOE FISHER <sup>8</sup> DANIEL P. THORNGREN <sup>1</sup>  
NICHOLAS WOGAN <sup>9</sup> ERIN M. MAY <sup>10</sup> PIERO FERRARI <sup>11</sup> KATHERINE A. BENNETT <sup>12</sup> ZAFAR RUSTAMKULOV <sup>12</sup>  
MERCEDES LÓPEZ-MORALES <sup>13</sup> AND DAVID K. SING <sup>1,12</sup>

<sup>1</sup>William H. Miller III Department of Physics and Astronomy, Johns Hopkins University, Baltimore, MD 21218, USA

<sup>2</sup>Department of Astronomy, University of Michigan, 1085 S. University Ave., Ann Arbor, MI 48109, USA

<sup>3</sup>Department of Earth and Planetary Sciences, University of California, Riverside, CA, USA

<sup>4</sup>Department of Astronomy & Astrophysics, University of Chicago, 5640 South Ellis Avenue, Chicago, IL 60637, USA

<sup>5</sup>Institut Trottier de Recherche sur les Exoplanètes and Département de Physique, Université de Montréal, 1375 Avenue Thérèse-Lavoie-Roux, Montréal, QC, H2V 0B3, Canada

<sup>6</sup>Max Planck Institute for Astronomy, Heidelberg, 69117, Germany

<sup>7</sup>BAER Institute, NASA Ames Research Center, Moffet Field, CA 94035, USA

<sup>8</sup>Astrophysics, University of Oxford, Denys Wilkinson Building, Keble Road, Oxford, OX1 3RH, United Kingdom

<sup>9</sup>NASA Ames Research Center, Moffett Field, CA 94035, US

<sup>10</sup>Johns Hopkins APL, Laurel, MD 20723, USA

<sup>11</sup>Radboud University, Institute for Molecules and Materials, FELIX Laboratory, Nijmegen, The Netherlands

<sup>12</sup>Morton K. Blaustein Department of Earth & Planetary Sciences, Johns Hopkins University, Baltimore, MD 21218, USA

<sup>13</sup>Space Telescope Science Institute, 3700 San Martin Drive, Baltimore, MD 21218, USA

Submitted to AAS Journals

### ABSTRACT

Sub-Neptunes are the most common type of planet in our galaxy. Interior structure models suggest that the coldest sub-Neptunes could host liquid water oceans underneath their hydrogen envelopes—sometimes called “hycean” planets. JWST transmission spectra of the  $\sim 250$  K sub-Neptune K2-18 b were recently used to report detections of CH<sub>4</sub> and CO<sub>2</sub>, alongside weaker evidence of (CH<sub>3</sub>)<sub>2</sub>S (dimethyl sulfide, or DMS). Atmospheric CO<sub>2</sub> was interpreted as evidence for a liquid water ocean, while DMS was highlighted as a potential biomarker. However, these notable claims were derived using a single data reduction and retrieval modeling framework, which did not allow for standard robustness tests. Here we present a comprehensive reanalysis of K2-18 b’s JWST NIRISS SOSS and NIRSpec G395H transmission spectra, including the first analysis of the second-order NIRISS SOSS data. We incorporate multiple well-tested data reduction pipelines and retrieval codes, spanning 60 different data treatments and over 250 atmospheric retrievals. We confirm the detection of CH<sub>4</sub> ( $\approx 4\sigma$ ), with a volume mixing ratio of  $\log \text{CH}_4 = -1.15^{+0.40}_{-0.52}$ , but we find no statistically significant or reliable evidence for CO<sub>2</sub> or DMS. Finally, we quantify the observed atmospheric composition using photochemical-climate and interior models, demonstrating that our revised composition of K2-18 b can be explained by an oxygen-poor mini-Neptune without requiring a liquid water surface or life.

**Keywords:** Exoplanets(498) — Exoplanet atmospheres(487) — Exoplanet structure(495) — Habitable planets(695) — Mini Neptunes(1063) — Exoplanet atmospheric composition(2021)

Corresponding author: Stephen Schmidt  
[sschmi42@jh.edu](mailto:sschmi42@jh.edu)

† NHFP Sagan Fellow

‡ NSERC Postdoctoral Fellow

\* NSF Graduate Research Fellow

## 1. INTRODUCTION

James Webb Space Telescope (JWST) transmission spectroscopy has revealed the atmospheric composition of dozens of transiting exoplanets in the three years since its launch. The most amenable planets to atmospheric characterization are hot H<sub>2</sub>-dominated giant exoplanets. Major JWST results from such hot giant planets include detections of SO<sub>2</sub> (e.g., Rustamkulov et al. 2023; Alderson et al. 2023; Dyrek et al. 2024; Powell et al. 2024; Sing et al. 2024; Welbanks et al. 2024), which provides direct evidence for photochemistry in exoplanetary atmospheres (e.g., Tsai et al. 2023), and the direct detection of aerosol species (Grant et al. 2023; Dyrek et al. 2024; Inglis et al. 2024). JWST is also enabling initial forays into population-level trends across properties of giant exoplanet atmospheres (e.g., Fu et al. 2025), which will provide deeper insights as more transmission spectra are analyzed in the coming years.

While JWST transmission spectra have succeeded in probing the giant exoplanet atmospheres, decisive results have been more elusive for the small and cold ends of the exoplanet population. For super-Earths and terrestrial worlds ( $R_p < 1.7 R_\oplus$ ), JWST transmission spectra largely rule out thick H<sub>2</sub>-dominated atmospheres (e.g., Lustig-Yaeger et al. 2023; Lim et al. 2023; Alderson et al. 2024; Radica et al. 2024a) or are degenerate with unocculted stellar active regions (e.g., Moran & Stevenson et al. 2023; May & MacDonald et al. 2023). However, sub-Neptunes<sup>1</sup>, planets with radii  $1.7 R_\oplus < R < 3.5 R_\oplus$ , likely possess significant atmospheres dominated by relatively light molecules (e.g., H<sub>2</sub> or H<sub>2</sub>O), which aids their atmospheric detectability. While searches for atmospheres on several sub-Neptunes have yielded non-detections (e.g. Wallack et al. 2024) or weak evidence (e.g., Damiano et al. 2024; Cadieux et al. 2024), an emerging population now has definitive atmospheric detections. To date, JWST has detected atmospheres on four sub-Neptunes: GJ 3470 b (Beatty et al. 2024), GJ 9827 d (Piaulet-Ghorayeb et al. 2024), TOI-270 d (Benneke et al. 2024; Holmberg & Madhusudhan 2024), and K2-18 b (Madhusudhan et al. 2023). Of these planets, the cold ( $\sim 250$  K) sub-Neptune K2-18 b has attracted significant observational and theoretical interest in its atmospheric composition and interior structure.

The K2-18 system was identified as a potential transiting exoplanet system in the first campaign of NASA’s K2 mission (Montet et al. 2015). Further transit obser-

vations by Spitzer (Benneke et al. 2017) and radial velocity follow-up (Cloutier et al. 2017; Sarkis et al. 2018) confirmed K2-18 b as a habitable zone planet, with a refined radial velocity extraction method further improving its mass precision (Radica et al. 2022a). The system is now known to host at least two planets (Cloutier et al. 2019; Radica et al. 2022a), though only K2-18 b transits its early M dwarf host star. The combination of its cool temperature (255 K, assuming an albedo of 0.3; Benneke et al. 2019), relatively large planetary radius ( $2.61 R_\oplus$ ), and small stellar radius ( $0.4445 R_\odot$ ) has led to K2-18 b being one of the best targets for the atmospheric characterization of a potentially habitable exoplanet.

Initial transmission spectroscopy observations of K2-18 b with the Hubble Space Telescope (HST) yielded a detection of a H<sub>2</sub>-dominated atmosphere, with evidence of either gas phase H<sub>2</sub>O or CH<sub>4</sub>. The HST Wide Field Camera 3 (WFC3) transmission spectrum of K2-18 b was initially interpreted as showing a  $> 3\sigma$  detection of H<sub>2</sub>O (Tsiaras et al. 2019; Benneke et al. 2019; Madhusudhan et al. 2020). However, later work by Barclay et al. (2021) argued that the low-resolution WFC3 data could alternatively be explained by CH<sub>4</sub>, due to the similar shapes of H<sub>2</sub>O and CH<sub>4</sub> absorption over the 1.1–1.7  $\mu\text{m}$  WFC3 bandpass. These competing interpretations of K2-18 b’s atmospheric composition resulted in an inability to definitively constrain the nature of its atmosphere and interior through HST observations alone.

Atmospheric and interior models of K2-18 b have ignited a vigorous debate on the nature of this world. Early atmospheric models disfavored a water reservoir below the H<sub>2</sub>-dominated atmosphere as the source of the apparent H<sub>2</sub>O vapor (Scheucher et al. 2020), while general circulation models pointed towards a misinterpretation of the HST data as caused by CH<sub>4</sub> rather than H<sub>2</sub>O (Blain et al. 2021). Interior structure models of K2-18 b highlighted that the pressure-temperature profile could allow a habitable liquid water ocean beneath a thin H<sub>2</sub> atmosphere (Madhusudhan et al. 2020; Piette & Madhusudhan 2020; Nixon & Madhusudhan 2021) — sometimes termed a “hycean” planet. Sustaining such a liquid water ocean requires the planet to have a H<sub>2</sub>-rich atmosphere, an iron-rock core comprising  $> 10\%$  of the planet’s mass, and a H<sub>2</sub>O layer with a mass fraction from 10–90% (Madhusudhan et al. 2021). Such an ocean can be considered a habitable surface, which renders K2-18 b an object of potential astrobiological interest in the search for extraterrestrial life.

Recently, the first JWST transmission spectrum of K2-18 b revealed multiple prominent atmospheric absorption features (Madhusudhan et al. 2023). The NIRISS SOSS and NIRSpec G395H observations (span-

<sup>1</sup> We use “sub-Neptune” when categorizing planets by size (c.f. super-Earth), and “mini-Neptune” when categorizing planets by interior structure (c.f. hycean).

ning 0.8–5.3  $\mu\text{m}$ ) were explained by strong atmospheric  $\text{CH}_4$  bands (detected at  $5\sigma$ ), a peak near 4.3  $\mu\text{m}$  attributed to  $\text{CO}_2$  (at  $3\sigma$ ), and “potential signs” of  $(\text{CH}_3)_2\text{S}$  (dimethyl sulfide, or DMS). The JWST detection of  $\text{CH}_4$ , and non-detection of  $\text{H}_2\text{O}$ , revealed that the previous inference of  $\text{H}_2\text{O}$  from HST was indeed a case of mistaken identity. Madhusudhan et al. (2023) reported an atmospheric composition of  $\sim 1\%$   $\text{CH}_4$  and  $\sim 1\%$   $\text{CO}_2$ , which is challenging to explain under standard thermochemistry for a mini-Neptune with a deep atmosphere. They also reported a non-detection of  $\text{NH}_3$ , a gas that would generally be expected in a mini-Neptune at K2-18 b’s temperature, with an upper limit of  $\approx 30$  ppm. Madhusudhan et al. (2023) argued that these two lines of evidence point towards a water ocean beneath the  $\text{H}_2$ -dominated outer layer, since an ocean would increase the  $\text{CO}_2/\text{CH}_4$  ratio and deplete  $\text{NH}_3$  (Hu et al. 2021; Tsai et al. 2021a).

Subsequent modeling efforts have argued that the JWST observations of K2-18 b do not require a habitable liquid water ocean. Shorttle et al. (2024) proposed that the  $\text{NH}_3$  non-detection can be explained by a deep  $\text{H}_2$  envelope above a magma ocean, which allows efficient dissolution of nitrogen. Yang & Hu (2024) found that the  $\text{CO}_2/\text{CH}_4$  ratio of  $\sim 1$  from Madhusudhan et al. (2023) can also be explained by a gas-rich mini-Neptune enriched in water vapor in the deep atmosphere. Wogan et al. (2024) used photochemical and climate models to investigate three scenarios for K2-18 b: (i) a lifeless hycean planet, (ii) an ‘inhabited’ hycean planet with a substantial biological  $\text{CH}_4$  flux into the atmosphere, and (iii) a  $100\times$  solar metallicity mini-Neptune. They ruled out the first scenario (which would have  $< 1$  ppm of  $\text{CH}_4$ ), such that the  $\sim 1\%$   $\text{CH}_4$  abundance inferred from JWST could be explained by either a methane-producing biosphere or, alternatively, a metal-enriched mini-Neptune. Wogan et al. (2024) argued that the mini-Neptune scenario is more plausible *a priori*, since this explanation works ‘out of the box’ without requiring one to postulate the existence of life. Most recently, Cooke & Madhusudhan (2024) investigated the same three scenarios, arguing that the  $\text{CO}_2$  abundance found by Madhusudhan et al. (2023) favors the ‘inhabited’ hycean scenario over a mini-Neptune.

The astrobiological assessment of  $\text{H}_2$ -dominated sub-Neptunes such as K2-18 b is at an early stage, and hence any claims of life must be tempered with extreme caution. Madhusudhan et al. (2023) highlighted a low-significance inference of DMS ( $\sim 1\sigma$  from their best-fitting model) as potential evidence for life, given DMS is significantly produced by marine phytoplankton on Earth (Charlson et al. 1987; Barnes et al. 2006).

However, the recent detection of DMS on a comet by Hänni et al. (2024) demonstrates that DMS can also be produced in abiotic environments. Further, Tsai et al. (2024) demonstrated that a DMS flux equivalent to  $\sim 20$  times that produced by Earth’s marine life would be required for DMS to reach detectable levels on a hycean planet with K2-18 b-like conditions. Recently, Glein (2024) recently showed that  $\text{CO}_2$ -consuming and  $\text{CH}_4$ -producing life is energetically viable on K2-18 b, if one assumes a hycean scenario and the atmospheric abundances reported in Madhusudhan et al. (2023).

The plausibility of the hycean interpretation for K2-18 b relies critically on the retrieved chemical abundances reported by Madhusudhan et al. (2023). However, to date, there has been no independent analysis of the original JWST transmission spectrum of K2-18 b. The gold standard for interpreting JWST spectra of exoplanet atmospheres is to apply multiple data reduction techniques and retrieval codes to confirm the reproducibility and robustness of the results — this philosophy has been broadly adopted by the exoplanet community (e.g., Coulombe et al. 2023; Taylor et al. 2023; Grant et al. 2023; Powell et al. 2024; Gressier et al. 2024; Banerjee et al. 2024; Piaulet-Ghorayeb et al. 2024; Welbanks et al. 2024). However, the K2-18 b analysis by Madhusudhan et al. (2023) investigated only a single reduction and retrieval model framework. Performing several reductions on the same data set quantifies the impact of choices such as outlier rejection, noise correction, and limb darkening treatments that occur when using independent pipelines. Similarly, performing retrievals with different codes quantifies how model-level assumptions (e.g., opacity sources, aerosol parameterization) propagate into atmospheric inferences. Atmospheric inferences that withstand these tests are considered robust. On the other hand, severe inconsistencies (e.g., a molecular detection seen only with one reduction), demonstrate that the statistical evidence for such an atmospheric inference must be carefully assessed. Here, we provide the first comprehensive analysis of K2-18 b’s JWST NIRISS SOSS and NIRSpec G395H transmission spectra, using multiple data reduction and retrieval codes, to offer an updated assessment of K2-18 b’s atmospheric composition and possible interior structures.

Our study is structured as follows. We describe our new K2-18 b data reductions in Sections 2 and 3 for NIRISS SOSS and NIRSpec G395H, respectively. Our retrieval analysis and atmospheric composition constraints are presented in Section 4. We model plausible atmospheric and interior structures for K2-18 b in Section 5. Finally, we summarize our results and discuss the implications in Section 6.

## 2. NIRISS DATA REDUCTIONS

The K2-18 system was observed by JWST’s Near Infrared Imager and Slitless Spectrograph (NIRISS; [Doyon et al. 2012, 2023](#)) instrument using the Single Object Slitless Spectroscopy (SOSS; [Albert et al. 2023](#)) mode from 13:49:20 UTC to 19:36:05 UTC (for a total of 4.9 hours) on June 1, 2023 as part of JWST GO Program 2722 (PI: N. Madhusudhan). The observation, which covered one transit of K2-18 b, used the  $R \sim 700$  GR700XD grism, CLEAR filter, SUBSTRIP256 subarray, and NISRAPID readout pattern. The exposure consisted of 648 integrations with 4 groups per integration, and there were no mirror tilt events or high-gain antenna movements during the observation. The first spectral order yielded a wavelength coverage of 0.85–2.85  $\mu\text{m}$  which, when combined with the second order’s wavelength coverage of 0.6–1.4  $\mu\text{m}$ , results in a total uninterrupted wavelength coverage of 0.6–2.85  $\mu\text{m}$ .

We perform two reductions with two independent pipelines: FIREFLY and exoTEDRF<sup>2</sup>. To allow a transparent comparison between our reduction approaches and [Madhusudhan et al. \(2023\)](#) (who used the JExoRES pipeline [Holmberg & Madhusudhan 2023](#)), we provide an overview of the most important reduction-level configuration choices for NIRISS in Table 1 and show additional diagnostic plots for our reductions in Appendix C.

### 2.1. FIREFLY

We use the FIREFLY pipeline ([Rustamkulov et al. 2022, 2023](#)), which has been recently updated to better support NIRISS/SOSS observations (e.g., [Liu & Wang et al. in prep](#), [Wang et al. in prep](#)), to re-reduce the K2-18 NIRISS/SOSS observations. We start from the raw, uncalibrated files on MAST and followed the `rwst` pipeline for group-level and instrument corrections. We start by performing the saturation and superbias steps, but we skip the dark current step. To correct the  $1/f$  noise at the group level, we first subtract the zodiacal background at each group. This is done by scaling the flux jump caused by the reflection of zodiacal light off the pick-off mirror in the STScI SOSS background model to the flux jump present in the observed data and adding a constant offset to match the flux level of the model SOSS background before and after the jump to the observed data. We then mask out the bright spectral trace and notable zeroth order contaminants present in the

frame and performed  $1/f$  destriping by subtracting the median of each PSF-masked and background-subtracted column. In addition, we subtract each image from the temporal median, which we create as a running median of a 7 frame window, to reveal any remaining  $1/f$  noise and subtract it. This removes high frequency structure while preserving the slowly changing source flux. Because the background levels are real counts and not the detector’s bias level, we add the background back after subtracting the  $1/f$  noise in order to ensure that the `rwst` pipeline’s bias correction and up-the-ramp fitting procedures are unaffected. We perform the default linearity and ramp fitting step, but we skip the jump step. For the wavelength calibration and order tracing, we use `pastasoss` ([Baines et al. 2023](#)), which predicts the GR700XD PSF positions and the wavelength solutions accordingly with sub-pixel accuracy based on the position of pupil wheels. We apply an integration-level  $1/f$  subtraction and clean  $> 5\sigma$  outlier bad/hot pixels.

We then perform Stage 3, FIREFLY’s stellar and spectral extraction step. We apply a  $> 15\sigma$  temporal outlier cut, remove the background for the final time, and perform an additional  $1/f$  noise removal at the integration level. Both the background removal and  $1/f$  noise subtraction follow the same algorithm as the group level. To extract the white light curves, we sum all the flux in order 1 and the flux from wavelengths within [0.6, 0.85]  $\mu\text{m}$  for order 2. We align frames and conduct box extractions on each order with aperture widths that minimize the scatter of the white light curve for each order—30 pixels for order 1 and 23 pixels for order 2.

We model the transit light curves with the `batman` Python package ([Kreidberg 2015](#)). We note a spot-crossing event in the NIRISS light curve, so we trim out those integrations accordingly. Informed by the Bayesian Information Criterion (BIC), we choose the systematics vector to be composed solely of a linear trend for both order 1 and order 2. We fit for the orbital parameters:  $a/R_*$ , the stellar radius-scaled semimajor axis;  $b$ , the impact parameter; and  $T_0$ , the center-of-transit time. We find that our fitted values are consistent with those reported by [Madhusudhan et al. \(2023\)](#); we therefore fix the orbital parameters to theirs for a consistent comparison. We jointly fit the transit light curves and the systematics using the Markov Chain Monte Carlo (MCMC) sampler `emcee` ([Foreman-Mackey et al. 2013](#)), as implemented in the `lmfit` Python package ([Newville et al. 2024](#)). We show the white light curve fits for the NIRISS SOSS orders 1 and 2 separately in Figure 1, with the spot-crossing event highlighted.

For limb darkening, we perform a two-step process. We first fit the white light curve and spectrophotomet-

<sup>2</sup> We do not perform NIRISS reductions with the `Eureka!` pipeline, as support for this instrument mode is currently pending.

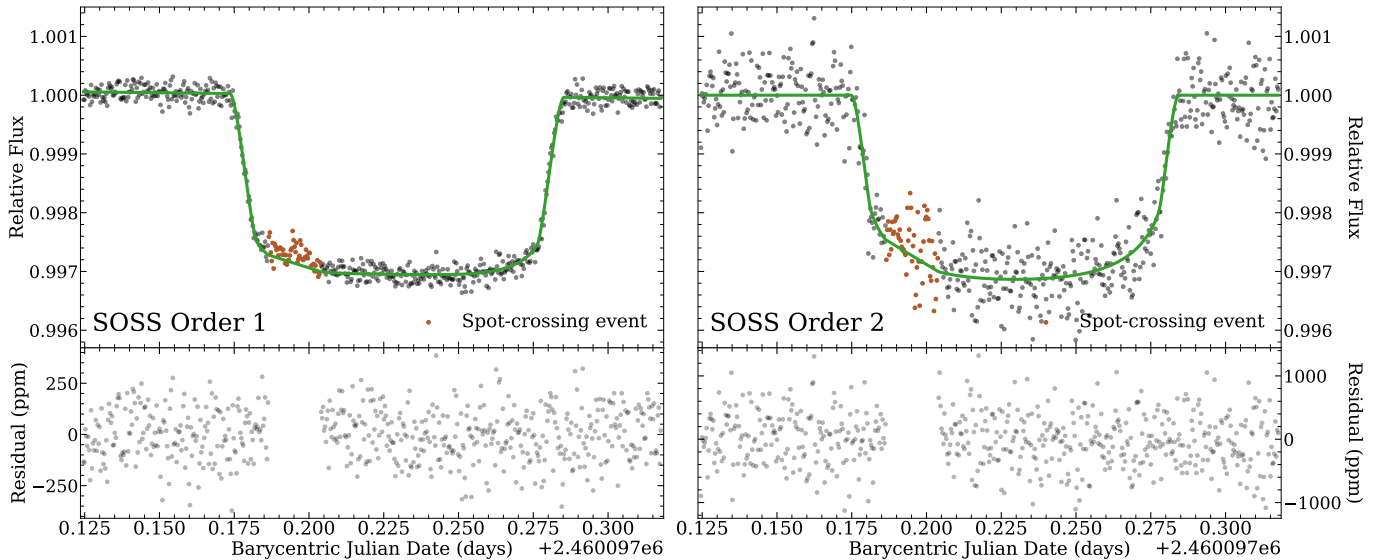


**Figure 1.** JWST NIRISS SOSS data and white light curve fit for K2-18b from the FIREFLY reduction. Left: first order data. Right: second order data. The photometric data points (points, top panels) are compared with the best fit light curve (green lines), resulting in a 124 ppm residual scatter for order 1 and 414 ppm for order 2 (bottom panels). Integrations during a spot-crossing event are highlighted (brown points), which are trimmed in the white and spectroscopic light curve fits.

ric limb darkening coefficients, before fixing them to a 3D Stagger grid stellar atmosphere model (Magic et al. 2015) with an offset. We experiment with both the Kipping (2013)  $\{q_1, q_2\}$  and the conventional quadratic  $u_+ = u_1 + u_2$  and  $u_- = u_1 - u_2$  limb darkening parametrizations. Since both approaches result in virtually identical transmission spectra, we adopt  $\{u_+, u_-\}$  for each of our fits (as  $q_2$  tends to be close to zero and less informative about the effects of limb darkening on the transit’s shape). Combining the fitted  $u_+$  and  $u_-$  from order 1 and order 2, we find that these fitted limb-darkening coefficients trace well the limb darkening coefficients from the Stagger grid of 3D stellar atmosphere models, with an offset of  $-0.14843$  for  $u_+$  and  $-0.07728$  for  $u_-$ . We therefore fix these offset model limb darkening coefficients for our spectrophotometric fit.

We fit the spectroscopic light curves at a two-pixel binning level (the same binning strategy as Madhusudhan et al. 2023) as well as at resolving powers  $R \approx 25$  and  $R \approx 100$ . We use two-pixel binning for NIRISS SOSS rather than one-pixel binning as its PSF is two pixels wide. As with the white light curve fit, we fix the orbital parameters to those used by Madhusudhan et al. (2023). For the spectroscopic light curve fits, we use the `lmfit` Python package to perform the Levenberg-Marquardt algorithm to fit the radius ratio for the spectrophotometric light curves as well as a linear systematic term for each bin. We account for red noise by inflating error bars in quadrature for wavelength bins where the Allan variance is above log linear. This does not impact the

error bars for most points, but for those that are, it is typically by a factor of no more than two.

## 2.2. *exoTEDRF*

We also reduced the time series observations using the publicly available `exoTEDRF` pipeline (Feinstein et al. 2023; Radica et al. 2023; Coulombe et al. 2023; Cadieux et al. 2024; Radica 2024), starting from the raw, uncalibrated files available on MAST. We closely follow the procedure laid out in Radica et al. (2024b), and we summarize the most pertinent points here. In `stage1` we correct the column-correlated  $1/f$  noise at the group level, using the `scale-achromatic` method. Before ramp fitting, we perform a time-domain outlier rejection (Radica et al. 2024b), using a threshold of  $10\sigma$ . We perform a piece-wise correction of the SOSS background (Lim et al. 2023; Fournier-Tondreau et al. 2024a), using the standard SOSS background model provided by STScI<sup>3</sup>, and a pre- and post-step scaling factor of 0.95784 and 0.92449 respectively relative to the background model. Finally, we extract the stellar spectra using a simple box aperture extraction with a width of 30 pixels, since the order self-contamination is expected to be negligible (Darveau-Bernier et al. 2022; Radica et al. 2022b).

For the light curve analysis, we first construct two separate white light curves by summing all the flux in

<sup>3</sup> <https://jwst-docs.stsci.edu/jwst-near-infrared-imager-and-slitless-spectrograph/niriss-observing-strategies/niriss-soss-recommended-strategies#gsc.tab=0>

**Table 1.** NIRISS Reduction Configuration Comparison

Step	FIREFLY (this work)	ExoTDRF (this work)	Madhusudhan et al. (2023)
<b>Stage 1</b>			
Saturation	Default	Default	Default
Superbias	Default	Default	Default
Dark current	Skipped	Default	Skipped
Background subtraction (group level)	Single-component STScI background model	Two-component STScI background model	Two-component STScI background model
1/f subtraction (group level)	Yes	scale-achromatic	Yes
Linearity	Default	Default	Default
Jump	Skipped	exoTDRF-custom, 10 $\sigma$ in time	Default, 5 $\sigma$
Ramp fitting	Default	Default	Default
<b>Stage 2</b>			
Wavelength calibration	pastasoss	Cross correlation with PHOENIX stellar model	?
1/f subtraction (integration-level)	Yes	No	Yes
Bad pixel cleaning	> 5 $\sigma$ outlier pixels	> 5 $\sigma$ outlier pixels in space and time	?
Order tracing	pastososs	edgetrigger	similar to edgetrigger
<b>Stage 3</b>			
Temporal outliers	> 15 $\sigma$	> 5 $\sigma$	?
1D Spectrum Extraction	Box extraction, 30 pixel aperture for order 1, 23 pixel aperture for order 2	Box extraction, 30 pixel aperture	Multi-order Horne (1986) spatial profile-based extraction, 35 pixel aperture
Exclusions	None	None	Columns with > 20% masked flux
<b>Stage 4</b>			
Light curve model	batman	batman	SPOTROD
Spot-crossing event treatment	Integrations trimmed	Gaussian in light curve model	4-parameter spot model in light curve model
Limb darkening	Fixed to Stagger model with offsets based on white light curve fit	Fit for each bin	Binned to $R \sim 20$ , fit in each bin
LD parameterization	{ $u_+$ , $u_-$ }	{ $u_1$ , $u_2$ }	{ $q_1$ , $q_2$ }
Systematic trends	linear	linear	linear
Code used for white light curve posterior	emcee	emcee	MultiNest
Binning method	2-pixel, $R \approx 25$ , and $R \approx 100$	2-pixel, $R \approx 25$ , and $R \approx 100$	2-pixel level
Code used for spectro-photometric fit	Levenberg-Marquardt; lmfit	MCMC; emcee	Levenberg-Marquardt
Error bar inflation	Red noise via Allan variance	Additive error inflation	?
Code Availability	Not Public	exoTDRF GitHub	Not Public

NOTE—“Default” refers to the default handling of the step in the *jwst* pipeline. The system parameters ( $a/R_*$ ,  $i$ , and  $T_0$ ) are consistent across each reduction, though they were calculated in Madhusudhan et al. (2023) based on their reduction up to that point. This is not an exhaustive list of reduction steps. “?” indicates reduction configuration settings not mentioned in Madhusudhan et al. (2023).

order 1, and wavelengths  $\lambda \in (0.6, 0.85]$  for order 2. We then jointly fit the white light curves using the flexible *exoUPRF* library (Radica 2024) following the procedure in Radica et al. (2024b,a). The fitted light curve model is composed of an astrophysical component (i.e., a *batman* transit model), and a systematics component. For the astrophysical component, we share the orbital parameters (i.e., time of mid-transit, orbital inclination and scaled semi-major axis, as well as the orbital eccentricity and argument of periastron) between the two orders, but separately fit the scaled planet radius and two parameters of the quadratic limb darkening law to

each. The systematics component consists of a linear trend with time, fit independently to each order, as well as a scalar jitter term added in quadrature to the flux errors. Finally, we note a star spot crossing event approximately 45 minutes before mid transit. Instead of commonly-used prescriptions like *spotrod* (Béky et al. 2014; Madhusudhan et al. 2023; Fournier-Tondreau et al. 2024a) we simply model the spot crossing using a Gaussian profile, which has been shown to produce equally accurate fits to spot crossing events in transit light curves (Roy et al. in prep). We fit the amplitude of the Gaussian independently to each order, but share the width

and position of the Gaussian between the two. In all, our white light fit has 19 free parameters, and we use wide, uninformative priors for each parameter. For the fits, we use the affine-invariant sampler `emcee` with 40 chains and using 50000 steps per chain. We discard the first 80% as burn-in.

We then fit the spectrophotometric light curves at three different resolutions — in bins with widths of two pixels (since the size of the SOSS point spread function is roughly two pixels in the dispersion direction), and constant resolutions of  $R \approx 100$  and  $R \approx 25$ . For the spectrophotometric fits, we fix the orbital parameters to those used by Madhusudhan et al. (2023) to allow a consistent comparison between the two works. We also test fixing the orbital parameters to the updated solution presented in Radica et al. (2022a), but find there to be negligible changes in the resulting transmission spectra. We also fix the location and width of the Gaussian spot model to our best-fitting white light curve values, but fit the amplitude for each wavelength bin. Finally, we freely fit the quadratic limb darkening parameters, systematic slope, and additive jitter term to each bin, resulting in a total of eight free parameters.

### 3. NIRSPEC DATA REDUCTIONS

The K2-18 system was also observed by JWST’s Near Infrared Spectrograph (NIRSpec; Ferruit et al. 2012; Birkmann et al. 2014) instrument using the  $R \sim 2700$  G395H grating from 18:37:38 UTC on January 20, 2023 to 01:11:32 UTC on January 21, 2023 as part of the same JWST GO Program as the NIRISS data. This observation, which also covered one full transit of K2-18 b, used the Bright Object Time Series (BOTS) mode with the F290LP filter, SUB2048 subarray, and NRSRAPID readout pattern. The spectra were dispersed over two detectors: NRS1, whose wavelength range covers 2.73–3.72  $\mu\text{m}$ , and NRS2, whose wavelength range covers 3.82–5.17  $\mu\text{m}$ . In total, the NIRSpec observation covers 2.73–5.17  $\mu\text{m}$  with a gap from 3.72–3.82  $\mu\text{m}$ .

We perform a total of four NIRSpec reductions: one with the FIREFLy pipeline, one with the ExoTEDRF pipeline, and two with the Eureka! pipeline. We summarize the most relevant choices made in each reduction, as well as a comparison to the reduction choices made in Madhusudhan et al. (2023)’s JExoRES NIRSpec reduction, in Table 2. As with NIRISS, we show several additional diagnostic figures for our reductions in Appendix C.

#### 3.1. FIREFLy

We also used the FIREFLy pipeline to conduct a full time-series analysis of the K2-18 NIRSpec/G395H data. Starting with the `uncal` data files, we use Stage 1 of the `rwst` pipeline for group-level detector and instrument corrections. We apply the data quality initialization and saturation steps to the `uncal` data files, but like the FIREFLy reduction of May & MacDonald et al. (2023) (and unlike the FIREFLy reduction of Moran & Stevenson et al. 2023) we do not apply a superbias scaling step. Instead, we use the default `rwst` superbias file. We also use the default background subtraction. We apply the reference pixel correction and linearity step, but not the dark current step. We also skip the jump step to avoid cosmic ray false positives due to a less well-constrained ramp linear slope, as typically occurs with data sets with fewer than 25 groups per integration. We apply a group-level  $1/f$  subtraction and finish Stage 1 with the standard ramp fitting and gain-scale steps. Moving to Stage 2 of the `rwst` pipeline, we next apply integration-level detector and instrument corrections. We skip the flat fielding step, only applying the assign World Coordinate System (WCS) step before moving to Stage 3, the FIREFLy pipeline’s stellar extraction step.

We clean bad pixels, which we determine by flagging pixels with sharp variance spikes of over  $100\sigma$  and other known bad pixels in NIRSpec G395H, using `lacosmic` (van Dokkum 2001) as the first part of the stellar extraction. We apply an integration-level  $1/f$  noise subtraction with a PSF mask, measure x- and y-shifts, and extract the 1D stellar spectrum as a box extraction using a standard NIRSpec/G395H trace. We use an aperture full-width of 5.2 pixels for NRS1 and 2.41 pixels for NRS2, as they minimize the scatter of the out-of-transit white light curve.

We also use `batman` to fit the cleaned spectrophotometric light curves. We bin the data in four ways: resolving powers  $R \approx 100$ ,  $R \approx 200$ , and  $R \approx 300$ , and at native pixel resolution. For each binning regime, we trim the first 575 columns of NRS1, first 8 columns of NRS2, and last 18 columns of NRS2. We fit for the mid-transit time  $T_0$ , scaled semimajor axis  $a/R_*$ , and impact parameter  $b$  in NRS1 and NRS2, and find that the weighted average orbital parameters  $a/R_* = 80.27 \pm 0.98$ ,  $b = 0.621 \pm 0.013$ , and  $T_0 = 0.46946 \pm 0.00004$  are consistent with those reported by Madhusudhan et al. (2023). We therefore fix the orbital parameters to theirs and fit the white light curve for the radius ratio  $R_p/R_*$ , quadratic limb darkening parameters  $u_+$  and  $u_-$ , and a linear term in time using the `emcee` Python package. For consistency with Madhusudhan et al. (2023), we experiment with including both a linear and quadratic term

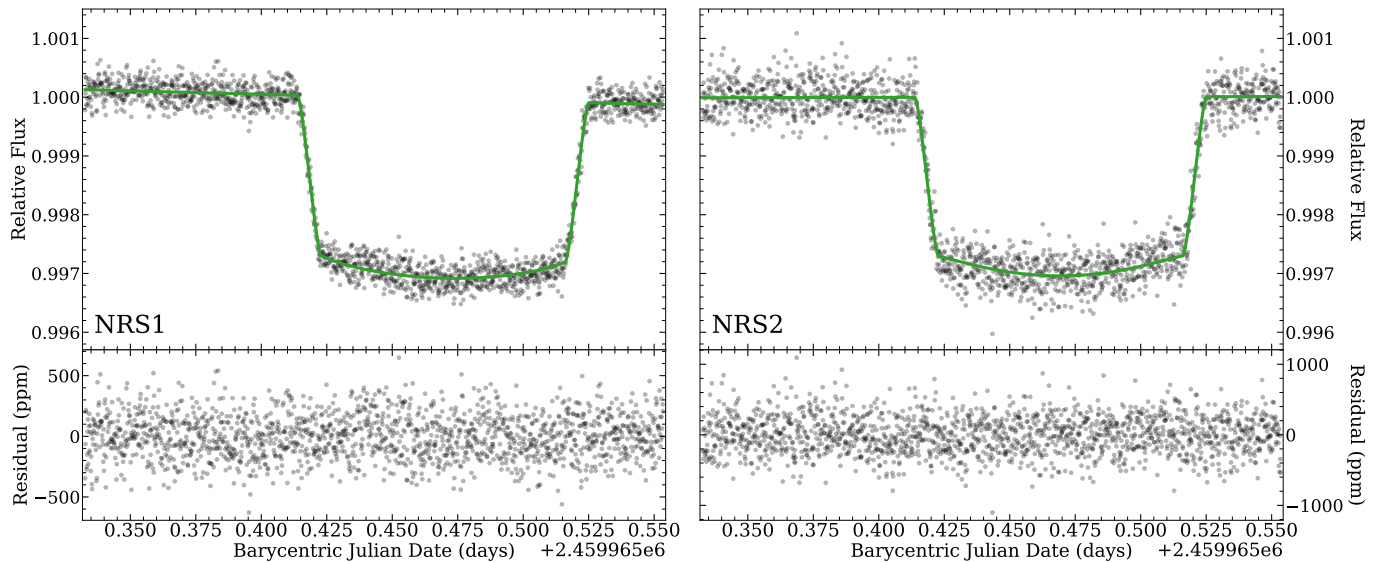


**Figure 2.** JWST NIRSpec G395H data and white light curve fit for K2-18b from the FIREFLY reduction. Left: NRS1 detector data. Right: NRS2 detector data. The photometric data points (points, top panels) are compared with the best fit light curve (green lines), resulting in a 180 ppm residual scatter for NRS1 and 269 ppm for NRS2 (bottom panels).

in time, but we find that only a linear term is favored; we therefore choose to only include a linear term. We show the results of our white light curve fit in Figure 2.

As with NIRISS, we use the `lmfit` Python package to perform the Levenberg-Marquardt algorithm to fit the radius ratio for the spectrophotometric light curves. For this fit we fix the limb darkening parameters and linear systematic term to the fitted white light curve values in addition to the already fixed orbital parameters. We elect to fix the spectrophotometric limb darkening values to the white light curve values as limb darkening is not expected to be strongly wavelength dependent at the redder wavelengths of NIRSpec (May & MacDonald et al. 2023; Moran & Stevenson et al. 2023). We account for red noise by inflating error bars in quadrature for wavelength bins where the Allan variance is above log linear. For most points this does not result in error bar inflation, and for points that are inflated, it is typically by a factor of no more than two. We show the spectroscopic light curve fits and residuals for each bin of our  $R \approx 100$  reduction in Appendix B. With both NIRISS and NIRSpec data in hand, we compare the low-resolution data-variants from each reduction code in Figure 3 ( $R \approx 25$  for NIRISS;  $R \approx 100$  for NIRSpec) and directly compare our pixel-level data, binned to the same resolution as Madhusudhan et al. (2023), in Figure 4.

### 3.2. *exoTEDRF*

To reduce the NIRSpec/G395H observations, we also use the `exoTEDRF` pipeline (Radica et al. 2023; Feinstein et al. 2023; Radica 2024), which has recently been up-

dated to support NIRSpec observations (Radica 2024, Ahrer et al. submitted). We start from the raw, uncalibrated data files and follow the procedure outlined in Ahrer et al. (submitted). For completeness, we summarize the key points here. We perform standard saturation and superbias corrections on the data frames (e.g., Alderson et al. 2023) before correcting the background and  $1/f$  noise at the group-level, using the `median` method and a trace mask width of 16 pixels. As with SOSS, we perform a time-domain outlier flagging (Radica et al. 2024b) with a rejection threshold of  $12\sigma$ . We then repeat the background and  $1/f$  correction at the integration-level, after ramp fitting, in order to remove any remaining traces of the background flux. We then interpolate all pixels which have a non-zero data quality flag, or are flagged as  $10\sigma$  temporal outliers using a median of the surrounding pixels in space and time, respectively. For the spectral extraction, we use the `edgetrigger` algorithm (Radica et al. 2022b) to determine the centroids of the NRS1 and NRS2 spectral traces, and then perform a box aperture extraction with a width of eight pixels.

We follow the same light curve fitting procedure as with the SOSS light curves — jointly fitting the NRS1 and NRS2 white light curves, sharing the planet’s orbital parameters between the two and independently fitting for chromatic parameters like the scaled planet radius, limb darkening and systematics. There is no spot crossing in the NIRSpec light curves, and so we do not include a Gaussian spot model. However, we keep the linear slope and error inflation term added in quadrature to the flux errors that were included in the SOSS fits. In



**Table 2.** NIRSpec Reduction Configuration Comparison

Step	FIREFLY (this work)	ExoTDRF (this work)	Eureka! A (this work)	Eureka! B (this work)	Madhusudhan et al. (2023)
<b>Stage 1</b>					
Saturation	Default	Default	Default	Default	Default
Superbias	Default	Default	Default	Eureka! custom	Default
Dark current	Skipped	Default	Default	Default	Default
Background subtraction (group level)	FIREFLY custom	exoTDRF custom	Eureka! custom	Eureka! custom	JExoRES custom
1/f subtraction (group level)	FIREFLY custom	exoTDRF custom	Eureka! custom	Eureka! custom	JExoRES custom
Linearity	Default	Default	Default	Default	Default
Jump	Skipped	exoTDRF custom, 12 $\sigma$ in time	Skipped	Default, 15 $\sigma$	Default, 5 $\sigma$
Ramp fitting	Default	Default	Default	Default	Default
<b>Stage 2</b>					
Wavelength calibration	Default	Cross correlation with PHOENIX model	Default	Default	Default
1/f correction (integration level)	Yes	Yes	No	No	No
<b>Stage 3</b>					
Bad pixel mask & temporal outliers	lacosmic & known bad pixels	Outliers > 10 $\sigma$ in time and > 10 $\sigma$ in space	Outliers > 3 $\sigma$ in time and > 5 $\times$ median in space	Outliers > 4 $\sigma$ in time and > 2.5 $\sigma$ in space	Data Quality flags only
1D Spectrum extraction	Box extraction with 5.2 pixel (for NRS1) & 2.41 pixel (for NRS2) aperture	Box extraction with <b>edgetrigger</b> -defined centroids	Horne (1986) spatial profile-based extraction, 3 pixel half width	Horne (1986) spatial profile-based extraction, 4 pixel half width	Horne (1986) spatial profile-based extraction with 3 principal component PSF
Exclusions	None	$\geq 5\sigma$ outliers	$\geq 4\sigma$ outliers	$\geq 4\sigma$ outliers	Columns with > 20% masked flux
<b>Stage 4</b>					
Trim	First 575 integrations in NRS1; first 8 & last 18 integrations in NRS2	None	None	First 25 integrations	First 5 minutes
Light curve model	<b>batman</b>	<b>batman</b>	<b>batman</b>	<b>batman</b>	SPOTROD
Starspot treatment	None	None	None	None	4-parameter spot model
Limb darkening	Fixed to fitted white light curve values for the respective detector	Fit for each bin	MPS-ATLAS model set 2, calculated with <b>exotic-1d</b>	PHOENIX model, calculated with <b>exotic-1d</b>	Binned to $R \sim 20$ , then fit in each bin and all pixels within the bin
LD parameterization	$\{u_+, u_-\}$	$\{u_1, u_2\}$	$\{u_1, u_2\}$	Quadratic	$\{q_1, q_2\}$
Systematic trends	Linear	Linear	Linear	Linear in time and linear correlation with position & spatial PSF width	Quadratic and linear
Code used for white light curve posterior	<b>emcee</b>	<b>emcee</b>	<b>emcee</b>	<b>dynesty</b>	<b>MultiNest</b>
Binning method	Pixel-level, $R \approx 100$ , $R \approx 200$ , and $R \approx 300$	Pixel-level, $R \approx 100$ , $R \approx 200$ , and $R \approx 300$	Pixel-level, $R \approx 100$ , $R \approx 200$ , and $R \approx 300$	Pixel-level, $R \approx 100$ , $R \approx 200$ , and $R \approx 300$	Pixel-level
Code used for spectro-photometric fit	Levenberg-Marquardt algorithm; <b>lmfit</b>	MCMC; <b>emcee</b>	MCMC; <b>emcee</b>	Nested Sampling; <b>dynesty</b>	Levenberg-Marquardt algorithm
Error bar inflation	Red noise via Allan variance	Jitter term	White noise term	White noise term	?
Code Availability	Not Public	<a href="#">exoTDRF GitHub</a>	<a href="#">Eureka! GitHub</a>	<a href="#">Eureka! GitHub</a>	Not Public

NOTE—“Default” refers to the default handling of the step in the **jwst** pipeline. The system parameters ( $a/R_*$ ,  $i$ , and  $T_0$ ) are the same for each reduction, and are calculated in Madhusudhan et al. (2023). This is not an exhaustive list of reduction steps. “?” indicates reduction configuration settings not mentioned in Madhusudhan et al. (2023).

all, our white light curve fits have 15 free parameters. We again use **emcee** for the fits, using the same amount of chains, steps, and burn in as above.

As with SOSS, we fix the orbital parameters to the values used by Madhusudhan et al. (2023) (there is, once

again, no difference in the resulting spectra using the Radica et al. (2022a) orbital solution), and fit the spectrophotometric light curves at four different resolutions, the pixel level (that is, one light curve per detector column),  $R \approx 300$ ,  $R \approx 200$ , and  $R \approx 100$ .

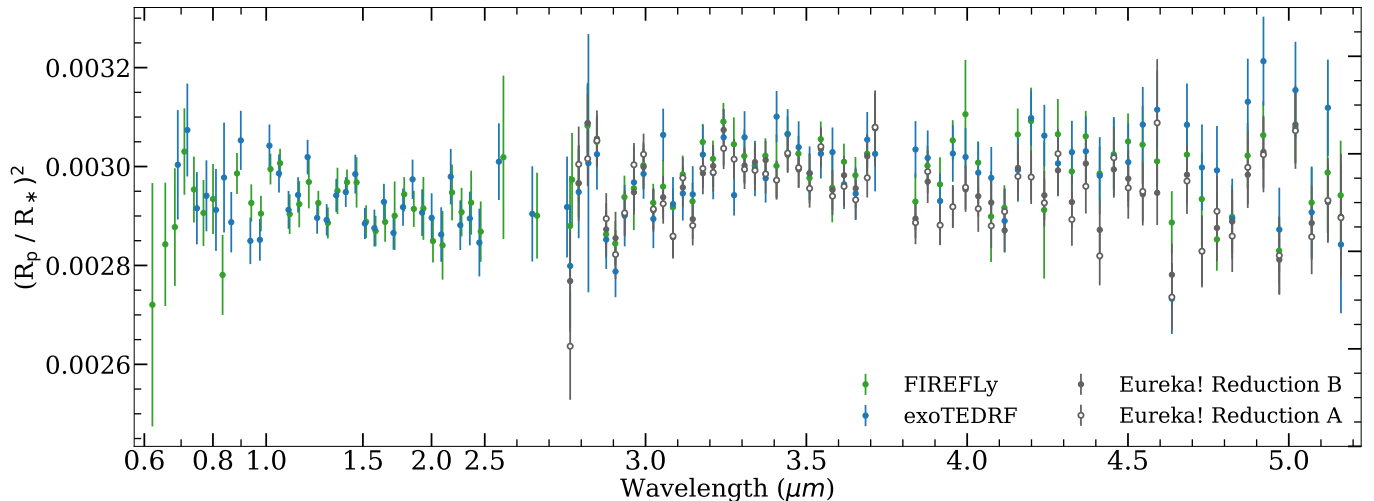


**Figure 3.** Four independently-reduced JWST transmission spectra of K2-18 b. NIRISS SOSS and NIRSpec G395H data sets reduced using the FIREFLY pipeline (green error bars; Rustamkulov et al. 2022, 2023, Liu & Wang et al. in prep, Wang et al. in prep) are compared with the same data reduced with the exoTEDRF pipeline (blue error bars; Radica 2024; Radica et al. 2023; Feinstein et al. 2023) and two NIRSpec G395H reductions using the Eureka! pipeline (error bars with grey (B)/white (A) central points; Bell et al. 2022). NIRISS data are shown at  $R \approx 25$  and NIRSpec data are shown at  $R \approx 100$ . The four reductions demonstrate broad agreement.

### 3.3. Eureka! Reductions

We conduct two independent reductions of the NIRSpec data using the open-source python package Eureka! (Bell et al. 2022) to test the extent to which the reduction choices within the same pipeline can yield differing final results. The Eureka! control and parameter files we used for each reduction, allowing replication of our results, are available for download on Zenodo: doi:10.5281/zenodo.14735688.

For our first Eureka! reduction, which we henceforth refer to as reduction “A”, we start with the uncalibrated files and run Stage 1 and Stage 2 which are wrapped around the jwst pipeline. We use the default steps in both stages with the exception of the jump step and the photom step, which we skip. We also use Eureka!’s group-level background subtraction and a custom bias scale factor (using a smoothing filter with a window length of 30 and group 1) in Stage 1<sup>4</sup>.

In Stage 3 we extract the stellar time-series spectra. First we correct the curved trace of the spectra and perform a background subtraction where we used the median of the entire frame, excluding the area within 5 pixels of the center of the trace. Prior to the calculation of the median background, we perform two iterations of outlier masking using thresholds of  $3\sigma$  along the time and 5 times the median along the spatial axis. We use an aperture of 7 pixels, corresponding to a 3-pixel half

width, to extract the time-series spectra with the optimal extraction (Horne 1986).

We generate pixel-level and binned light curves in Stage 4 of Eureka! following the same binning scheme as FIREFLY. We use a  $3\sigma$ -clipping at a 10-pixel-rolling-median to reduce the number of outliers. We fit the light curves by fixing the system parameters to the ones reported in Madhusudhan et al. (2023) to allow for direct comparison and the MCMC python package emcee. We opt to use a quadratic limb-darkening law, where we fix one parameter ( $u_1$ ) to limb darkening parameters generated using the exotic-ld Python package (Grant & Wakeford 2024) and the MPS-ATLAS (set 2) stellar atmosphere model grid (Kostogryz et al. 2023). We use a simple linear trend in time to account for a systematic trend in our light curves.

Our second Eureka! reduction, which we will henceforth refer to as reduction “B”, used version 0.11.dev446+gf5d684ee.d20240712; we started with the \_uncal files produced with SDP-VER 2023.3b, and we used version 1.15.1 of the jwst pipeline with CRDS version 11.17.26 and CRDS context jwst\_1252. Our reduction procedure largely followed the Eureka! reduction described in Schlawin et al. (2024); we summarize the important details below.

We increase the stage 1 jump step rejection threshold to 15, use Eureka!’s custom bias correction (computed using a smoothing filter of length 15 on group 1), and subtract the median background flux per column and per group after having first masked pixels near the

<sup>4</sup> See also Moran & Stevenson et al. 2023

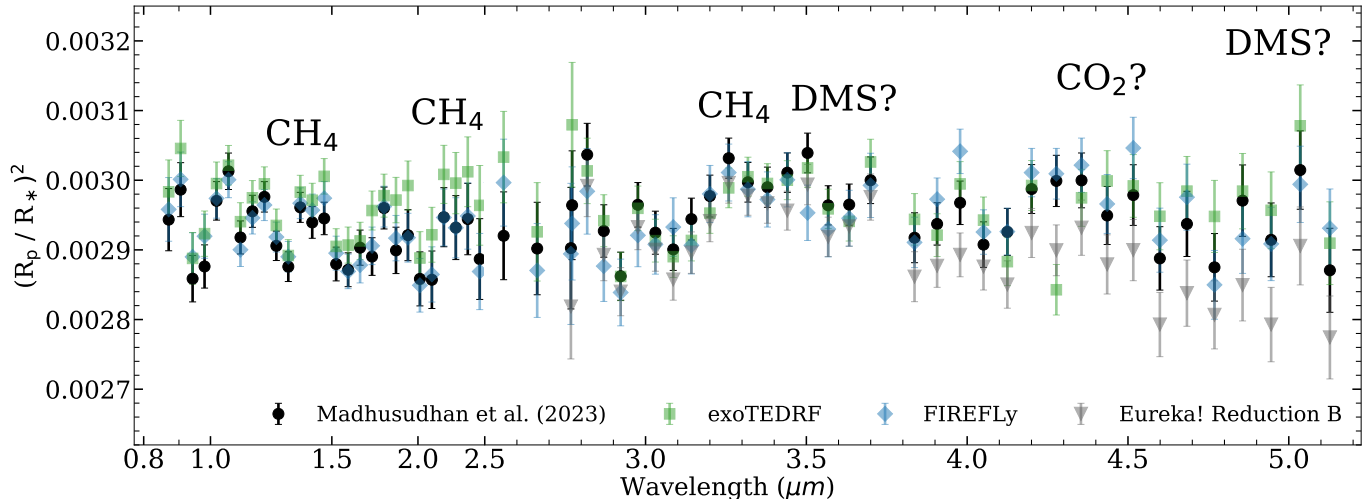


**Figure 4.** Comparison between our transmission spectra and the reduction from Madhusudhan et al. (2023). Three of our reductions, which were performed at the pixel level and then binned to  $R \approx 55$ , are shown: exoTEDRF (green squares), FIREFLY (blue diamonds), and the NIRSpec-only Eureka! reduction B (gray downward-pointing triangles). We show only Eureka! reduction B, since reduction A was performed at  $R = 100$ . We compare these binned pixel-level data to the low-resolution data from Madhusudhan et al. (2023), which were obtained using the JExoRES pipeline (black error bars; Holmberg & Madhusudhan 2023). The Madhusudhan et al. (2023) data were binned directly from their pixel-level data, so we bin our pixel-level data using the same binning approach. These  $R \approx 55$  datasets are purely for visual comparison with Madhusudhan et al. (2023), and are not used for retrievals later in our study. Wavelength locations of  $\text{CH}_4$ ,  $\text{CO}_2$ , and DMS absorption featured are annotated.

spectral trace. In stage 2, we skip the flat fielding, photometric calibration, and extract\_1d steps. In stage 3, we first mask all pixels labeled ‘DO\_NOT\_USE’ in the data quality array, and we then straighten the trace so that the center of the stellar PSF is centered on the subarray (using only integer-pixel shifts). We then  $4\sigma$  clip background pixels along the time axis and  $2.5\sigma$  along the spatial axis and then subtract the mean background flux per column and per integration computed using only the pixels  $\geq 6$  px away from the center of the spectral trace. Next, we perform optimal spectral extraction (Horne 1986) using a cleaned median integration to compute the spatial profile with a 4-pixel half width. In stage 4, we manually mask several pixel columns (18 in NRS1 and 9 in NRS2) that exhibit unusually high noise levels compared to their neighbors, likely due to unmasked bad pixels in an earlier stage. We then spectrally bin the data into multiple different spectral resolutions and mask any integration that was a  $\geq 4\sigma$  outlier with respect to a 20-integration wide boxcar filter, likely due to a missed cosmic ray.

When fitting the light curves, our astrophysical model consists of a batman transit model with quadratic limb-darkening coefficients fixed to a PHOENIX limb-darkening model computed by exotic-1d (Husser et al. 2013). We first verify that our broadband light curves are consistent with the orbital parameters reported by Madhusudhan et al. (2023), and then we fix our orbital param-

eters to those of Madhusudhan et al. (2023). Our systematic model consists of a linear trend in time and a linear correlation with the position and the width of the spatial PSF. We also fit for a white noise multiplier to account for any excess white noise in the data beyond the estimated photon noise. We trimmed the first 25 integrations to remove any initial detector settling. To estimate the best fit model values and their corresponding uncertainties, we use the dynesty dynamic nested sampling algorithm (Speagle 2020) with 121 live points, ‘multi’ bounds, the ‘rwalk’ sampling algorithm, and a convergence criterion of  $\Delta \log \mathcal{Z} \leq 0.01$ , where  $\mathcal{Z}$  is the Bayesian evidence.

#### 4. ATMOSPHERIC RETRIEVAL ANALYSIS OF K2-18 b’s TRANSMISSION SPECTRUM

Here we detail our atmospheric interpretation of K2-18 b’s JWST transmission spectrum. Our central goal is to quantify the sensitivity of atmospheric inferences to both data-level and model-level choices, establishing which atmospheric properties are robust and which are not. To this end, we conduct an extensive atmospheric retrieval analysis across the 60 possible combinations of re-analyzed NIRISS and NIRSpec data produced in this study. We use two independent retrieval codes to verify the robustness of our results. In total, our analysis comprises over 250 retrievals. We describe our retrieval configurations in Section 4.1 and our results in Section 4.2.

#### 4.1. Retrieval Configuration

We employ two open source retrieval codes, POSEIDON and BeAR, to explore the range of atmospheric properties consistent with the revised K2-18 b’s transmission spectra derived above. We additionally show retrieval results using the data from Madhusudhan et al. (2023) in Appendix A. Our retrieval configurations are constructed to encompass the parameter space explored by Madhusudhan et al. (2023), while also considering additional factors (such as planetary mass uncertainties and including the 2<sup>nd</sup> order NIRISS SOSS data). Our model settings, retrieval configurations, and a comparison with Madhusudhan et al. (2023) are summarized in Table 3.

##### 4.1.1. POSEIDON

We first retrieved K2-18 b’s transmission spectrum using the retrieval code POSEIDON<sup>5</sup> (MacDonald & Madhusudhan 2017; MacDonald 2023). POSEIDON is widely applied to interpret JWST transmission spectra, including hot Jupiters (e.g., Grant et al. 2023; Fournier-Tondreau et al. 2024b), sub-Neptunes (Piaulet-Ghorayeb et al. 2024), super-Earths (e.g., Moran & Stevenson et al. 2023; May & MacDonald et al. 2023), and terrestrial worlds (e.g., Lim et al. 2023; Cadieux et al. 2024). Here we use POSEIDON to conduct a systematic retrieval survey of the sensitivity of K2-18 b’s atmospheric inferences to 60 different data variants (reduction codes and/or data spectral resolution). Our POSEIDON retrieval configuration is constructed to be as close as possible to that described in Madhusudhan et al. (2023), allowing a fair comparison, but we emphasize and justify below several areas where we adopted different model choices.

Our atmosphere model for K2-18 b assumes a H<sub>2</sub>-He background gas (with a solar ratio of He/H<sub>2</sub> = 0.17; Asplund et al. 2009), commensurate with its planetary radius and mass ( $\approx 2.6 R_{\oplus}$  and  $\approx 8.6 M_{\oplus}$ , respectively). We construct atmospheres ranging from 10<sup>-8</sup>–10 bar with 100 layers spaced uniformly in log-pressure under hydrostatic equilibrium. We adopt 10<sup>-8</sup> bar as the lowest atmosphere pressure (vs. the 10<sup>-6</sup> bar limit implied by Madhusudhan et al. 2023) to reduce the risk of strong bands saturating the atmosphere. We solve hydrostatic equilibrium using a boundary condition where the freely retrieved reference pressure corresponds to the radial distance where  $r = 2.61 R_{\oplus}$  (the radius from Benneke et al. 2019). The atmospheric pressure-temperature (P-

T) profile is freely retrieved following the prescription in Madhusudhan & Seager (2009). We consider the same potential molecular species as Madhusudhan et al. (2023), which includes the major O-, C-, and N-bearing species expected at K2-18 b’s equilibrium temperature (255 K; Benneke et al. 2019): H<sub>2</sub>O, CH<sub>4</sub>, NH<sub>3</sub>, HCN, CO, and CO<sub>2</sub>; as well as several disequilibrium species proposed as biosignatures in cool sub-Neptunes (Madhusudhan et al. 2021): C<sub>2</sub>H<sub>6</sub>S (DMS), CS<sub>2</sub>, CH<sub>3</sub>Cl, OCS, and N<sub>2</sub>O. We fit the volume mixing ratios of these gases independently, with their number densities then determined via the ideal gas law. Given the large uncertainties on K2-18 b’s mass ( $8.63 \pm 1.35 M_{\oplus}$ ; Cloutier et al. 2019), we prescribe the planet’s mass as a free parameter using a Gaussian prior (Madhusudhan et al. 2023 fixed K2-18 b’s mass), allowing mass uncertainties to propagate into the retrieved atmospheric composition (Batalha et al. 2019a). Finally, we consider aerosols following the inhomogeneous cloud and haze parameterization of MacDonald & Madhusudhan (2017).

We calculate model spectra by solving the equation of radiative transfer in a cylindrical coordinate system for 100 incident stellar rays attenuated by atmospheric opacity along the line of sight. The POSEIDON opacity database recently underwent a major update in POSEIDON v1.2 (Mullens et al. 2024), including a state-of-the-art new ExoMol CH<sub>4</sub> line list (Yurchenko et al. 2024). Our POSEIDON opacities are pre-computed at a high resolution ( $\Delta\nu = 0.01 \text{ cm}^{-1}$ , equivalent to  $R = \lambda/\Delta\lambda = 10^6$  at 1  $\mu\text{m}$ ) for a grid of temperatures and pressures using the open source Python package Cthulhu<sup>6</sup> (Agrawal & MacDonald 2024). Our K2-18 b retrievals use opacities derived from the following line lists/measured cross sections: H<sub>2</sub>O (POKAZATEL; Polyansky et al. 2018), CH<sub>4</sub> (MM; Yurchenko et al. 2024), NH<sub>3</sub> (CoYuTe; Coles et al. 2019), HCN (Harris; Barber et al. 2014, CO (Li2015; Li et al. 2015), CO<sub>2</sub> (UCL-4000; Yurchenko et al. 2020), C<sub>2</sub>H<sub>6</sub>S (DMS) (HITRAN measured xsec; Sharpe et al. 2004) CS<sub>2</sub> (HITRAN-2020; Gordon et al. 2022), CH<sub>3</sub>Cl (HITRAN-2020; Gordon et al. 2022), OCS (OYT8; Owens et al. 2024), and N<sub>2</sub>O (HITEMP; Hargreaves et al. 2019). We further include continuum collision-induced absorption from H<sub>2</sub>-H<sub>2</sub> and H<sub>2</sub>-He pairs (Karman et al. 2019) and Rayleigh scattering for all gases (MacDonald & Lewis 2022). We calculate model transmission spectra using opacity sampling on a wavelength grid from 0.58–5.3  $\mu\text{m}$  at a spectral resolution of  $R = 100,000$ . We adopt this exceptionally high spectral resolution for all our

<sup>5</sup> <https://github.com/MartianColonist/POSEIDON>

<sup>6</sup> <https://github.com/MartianColonist/Cthulhu>

**Table 3.** Atmospheric Retrieval Configuration Comparison

Model Setting	POSEIDON (this work)	BeAR (this work)	AURA (Madhusudhan et al. 2023)
<b>System Properties</b>			
Stellar Radius (citation)	0.4445 $R_{\odot}$ Benneke et al. (2019)	0.41 $R_{\odot}$ Benneke et al. (2017)	0.4445 $R_{\odot}$ Benneke et al. (2019)
Planetary Radius	Fit (from $\log_{10} P_{\text{ref}}$ )	Fit (free parameter)	Fit (from $\log_{10} P_{\text{ref}}$ )
Planetary Mass	Fit (free parameter)	Fit (from $\log_{10} g_{\text{p}}$ )	8.63 $M_{\oplus}$
Planetary Gravity	Fit (from $M_{\text{p}}$ )	Fit (free parameter)	12.4 $\text{ms}^{-2}$
<b>Atmospheric Model</b>			
Pressure Grid	$10^{-8}$ –10 bar	$10^{-8}$ –10 bar	?
Number of Layers	100	200	?
Background Gas	H <sub>2</sub> + He	H <sub>2</sub> + He	H <sub>2</sub> + He
Molecules Included	H <sub>2</sub> O, CH <sub>4</sub> , NH <sub>3</sub> , HCN, CO, CO <sub>2</sub> DMS, CS <sub>2</sub> , CH <sub>3</sub> Cl, OCS, N <sub>2</sub> O	H <sub>2</sub> O, CH <sub>4</sub> , NH <sub>3</sub> , HCN, CO, CO <sub>2</sub> DMS, CS <sub>2</sub> , CH <sub>3</sub> Cl, OCS	H <sub>2</sub> O, CH <sub>4</sub> , NH <sub>3</sub> , HCN, CO, CO <sub>2</sub> DMS, CS <sub>2</sub> , CH <sub>3</sub> Cl, OCS, N <sub>2</sub> O
He/H <sub>2</sub> Ratio	0.17	0.17	?
P-T Profile Treatment (citation)	Free Profile (Madhusudhan & Seager 2009)	Isotherm	Free Profile (Madhusudhan & Seager 2009)
Cloud Treatment (citation)	Patchy Clouds + Haze (MacDonald & Madhusudhan 2017)	Opaque Cloud	Patchy Clouds + Haze (MacDonald & Madhusudhan 2017)
Hydrostatic Boundary Condition	$\log_{10} P_{\text{ref}}$	$R_{\text{p, ref}}$	$\log_{10} P_{\text{ref}}$
<b>Spectral Model</b>			
Model Wavelength Grid	0.58–5.3 $\mu\text{m}$	0.5996–5.176 $\mu\text{m}$	?
Native Opacity Resolution	0.01 $\text{cm}^{-1}$	0.01 $\text{cm}^{-1}$	?
Opacity Sampling Resolution	$R = 100,000$	$R = 60,000$	?
CH <sub>4</sub> Line List (citation)	MM (Yurchenko et al. 2024)	YT10to10 (Yurchenko & Tennyson 2014)	Ames-2016 (Huang et al. 2013, 2017)
CO <sub>2</sub> Line List (citation)	UCL-4000 (Yurchenko et al. 2020)	UCL-4000 (Yurchenko et al. 2020)	HITEMP (Hargreaves et al. 2020)
DMS Cross Section (citation)	HITRAN Sharpe et al. (2004)	HITRAN Sharpe et al. (2004)	HITRAN Sharpe et al. (2004)
<b>Stellar Contamination Model</b>			
Stellar Heterogeneity Treatment	One-het	Two-het	None <sup>†</sup>
Stellar Heterogeneity Parameters	$T_{\text{phot}}, T_{\text{het}}, f_{\text{het}}$	$T_{\text{phot}}, \Delta T_{\text{spot}}, \Delta T_{\text{fac}}, f_{\text{spot}}, f_{\text{fac}}$	— <sup>†</sup>
Stellar Model Grid	PHOENIX	blackbody	— <sup>†</sup>
Stellar Metallicity ([Fe/H])	-0.08	—	— <sup>†</sup>
Stellar Surface Gravity ( $\log_{10} g_{*}$ ) (citation)	4.93 (cgs) (Taberner et al. 2024)	—	— <sup>†</sup>
<b>Retrieval Priors and Settings</b>			
Planetary Mass ( $M_{\text{p}}$ )	$\mathcal{N}(8.63, 1.35^2) M_{\oplus}$	—	8.63 $M_{\oplus}$ (fixed)
Planetary Gravity ( $\log_{10} g_{\text{p}}$ )	—	$\mathcal{N}(3.19, 0.17^2)$ (cgs)	3.09 (fixed; cgs)
Atmospheric Temperature ( $T_{\text{ref}}$ )	$\mathcal{U}(0, 800)$ K	$\mathcal{U}(50, 1000)$ K	$\mathcal{U}(0, 800)$ K
P-T Profile Curvature 1 ( $\alpha_1$ )	$\mathcal{U}(0.02, 2.00) \text{K}^{-\frac{1}{2}}$	—	$\mathcal{U}(0.02, 2.00) \text{K}^{-\frac{1}{2}}$
P-T Profile Curvature 2 ( $\alpha_2$ )	$\mathcal{U}(0.02, 2.00) \text{K}^{-\frac{1}{2}}$	—	$\mathcal{U}(0.02, 2.00) \text{K}^{-\frac{1}{2}}$
P-T Profile Region 1 ( $\log_{10}(P_1 / \text{bar})$ )	$\mathcal{U}(-8, 1)$	—	$\mathcal{U}(-6, 0)$
P-T Profile Region 2 ( $\log_{10}(P_2 / \text{bar})$ )	$\mathcal{U}(-8, 1)$	—	$\mathcal{U}(-6, 0)$
P-T Profile Region 3 ( $\log_{10}(P_3 / \text{bar})$ )	$\mathcal{U}(-2, 1)$	—	$\mathcal{U}(-2, 0)$
Molecule Volume Mixing Ratio ( $\log_{10} X_i$ )	$\mathcal{U}(-12, -0.3)$	$\mathcal{U}(-12, -0.522)$	$\mathcal{U}(-12, -0.3)$
Reference Radius ( $R_{\text{p, ref}}$ )	2.61 $R_{\oplus}$ (fixed)	$\mathcal{U}(2.0, 2.8) R_{\oplus}$	2.61 $R_{\oplus}$ (fixed)
Reference Pressure ( $\log_{10}(P_{\text{ref}} / \text{bar})$ )	$\mathcal{U}(-6, 0)$	1.0 (fixed)	$\mathcal{U}(-6, 0)$
Cloud Pressure ( $\log_{10}(P_{\text{cloud}} / \text{bar})$ )	$\mathcal{U}(-8, 1)$	$\mathcal{U}(-7, 0)$	$\mathcal{U}(-6, 1)$
Cloud Fraction ( $\bar{\phi}$ )	$\mathcal{U}(0, 1)$	—	$\mathcal{U}(0, 1)$
Haze Rayleigh Enhancement ( $\log_{10} a$ )	$\mathcal{U}(-4, 10)$	—	$\mathcal{U}(-4, 10)$
Haze Slope ( $\gamma$ )	$\mathcal{U}(-20, 2)$	—	$\mathcal{U}(-20, 2)$
Data Offset 1 ( $\delta_{\text{rel}, 1}$ )	$\mathcal{U}(-100, 100)$ ppm	$\mathcal{U}(-100, 100)$ ppm	$\mathcal{U}(-100, 100)$ ppm
Data Offset 2 ( $\delta_{\text{rel}, 2}$ )	$\mathcal{U}(-100, 100)$ ppm	$\mathcal{U}(-100, 100)$ ppm	$\mathcal{U}(-100, 100)$ ppm
$T_{\text{phot}}$	$\mathcal{N}(3563, 25^2)$ K	$\mathcal{N}(3457, 39^2)$ K	— <sup>†</sup>
$T_{\text{het}}$	$\mathcal{U}(2300, 4275.6)$ K	—	— <sup>†</sup>
$f_{\text{het}}$	$\mathcal{U}(0, 0.5)$	—	— <sup>†</sup>
$\Delta T_{\text{spot}}$	—	$\mathcal{U}(-1500, 0)$ K	—
$\Delta T_{\text{fac}}$	—	$\mathcal{U}(0, 1000)$ K	—
$f_{\text{spot}}$	—	$\mathcal{U}(0, 0.5)$	—
$f_{\text{fac}}$	—	$\mathcal{U}(0, 0.5)$	—
MultiNest Live Points	1000	1000	?
Retrieval Code Availability	POSEIDON <a href="#">GitHub</a>	BeAR <a href="#">GitHub</a>	Not Public

NOTE—“?” indicates model settings not specified in Madhusudhan et al. (2023). Line list references for other molecules included in each retrieval code are provided in Sections 4.1.1 and 4.1.2. <sup>†</sup> All the results presented in Madhusudhan et al. (2023) did not include stellar contamination, but the study stated they ran additional (not shown) retrievals considering a one-heterogeneity model. Gaussian priors are summarized as  $\mathcal{N}(\mu, \sigma^2)$ , where  $\mu$  and  $\sigma$  are the mean and standard deviation, respectively.  $T_{\text{ref}}$  refers to the top-of-atmosphere temperature for POSEIDON and Madhusudhan et al. (2023), while for BeAR it represents the isothermal temperature.

POSEIDON retrievals for three reasons: (i) to ensure negligible opacity sampling errors when interpreting pixel-level data; (ii) to consistently sample cross sections for every data combination (even at lower resolutions); and (iii) to reduce the risk of opacity accuracy differences between our work and Madhusudhan et al. (2023) (since the latter did not state their assumed sampling resolution). While our  $R = 100,000$  models impose a greater computational burden than is strictly necessary for retrievals of JWST data<sup>7</sup>, this ensures high-accuracy in our retrieved atmospheric properties.

Our POSEIDON retrievals additionally account for stellar contamination from unocculted active regions, commonly known as the transit light source effect (Rackham et al. 2018). We employ a one-heterogeneity model (e.g., Rathcke et al. 2021; Lim et al. 2023; Fournier-Tondreau et al. 2024a), defined by the stellar photosphere temperature, the heterogeneity temperature (corresponding to spots/faculae if the heterogeneity is cooler/warmer than the photosphere), and the heterogeneity covering fraction. The stellar contamination contribution is calculated by interpolating PHOENIX models (Husser et al. 2013) using the PyMSG package (Townsend & Lopez 2023). For fixed stellar properties, we adopt the stellar radius from Benneke et al. (2019) ( $R_* = 0.4445 R_\odot$ ) and the stellar surface gravity, metallicity, and effective temperature from Tabernero et al. (2024) ( $[\text{Fe}/\text{H}] = -0.08$ ,  $\log_{10} g_* = 4.93$ ,  $T_{\text{eff}} = 3563 \text{ K}$ ). These updated K2-18 stellar properties were published after Madhusudhan et al. (2023), so we adopt them for a more accurate characterization of the transit light source effect.

Our reference POSEIDON retrieval model has 28 free parameters, with priors as given in Table 3. We generally adopt the same priors as Madhusudhan et al. (2023) for consistency, with a few exceptions: (i) we adjust the pressure parameters describing the P-T profile and cloud-top pressure to span our wider atmospheric pressure range; (ii) we apply a Gaussian prior on the planetary mass, using the standard deviation from Cloutier et al. (2019); and (iii) we use newly updated constraints on the host star’s effective temperature from Tabernero et al. (2024) to set the Gaussian prior on  $T_{\text{phot}}$ . We allow for two free offsets, one between the NIRISS SOSS and NIRSpec G395H NRS1 data and one between the NIRISS and NIRSpec G395H NRS2 data, as both Madhusudhan et al. (2023) and our Appendix A demonstrate the need for at least one free offset. Alongside the refer-

ence model, we additionally ran nested retrievals, with  $\text{CH}_4$ ,  $\text{CO}_2$ , and DMS removed in turn, to calculate the Bayes factors (and hence the equivalent detection significances) for these molecules. Therefore, we ran 4 retrievals for each combination of NIRISS SOSS (6 variants: 2 reduction pipelines each with 3 resolutions) and NIRSpec G395H data (10 variants: 2 reduction pipelines each with 4 resolutions, and 2 reduction pipelines with 1 resolution), for a total of 240 retrievals spanning the 60 different data combinations. We use PyMultiNest (Feroz et al. 2009; Buchner et al. 2014) with 1,000 live points to explore the parameter space. Each retrieval took 2–5 days on 24 CPUs — with longer run-times for pixel-level data variants — for a total compute time of  $\gtrsim 50$  CPU years.

#### 4.1.2. BEAR

To validate our POSEIDON results, we also perform a second set of retrievals using the open-source Bern Atmospheric Retrieval code (BeAR<sup>8</sup>). BeAR is an updated version of the retrieval code formerly known as Helios-r2, which was originally developed for retrievals on Brown Dwarf spectra (Kitzmann et al. 2020). BeAR has been adapted for use on exoplanet spectra (Fisher et al. 2024) and has the capabilities to analyze transmission, emission, and phase curve spectra. BeAR uses opacity sampling of line-by-line cross sections to calculate model spectra, coupled to PyMultiNest (Feroz et al. 2009; Buchner et al. 2014) for statistical exploration.

Our BeAR retrievals use a similar retrieval configuration to that described above, but here we highlight differences in the model setup. First, we assume for simplicity an isothermal temperature throughout the atmosphere (with a uniform prior of 50–1000 K). The atmosphere is divided into 200 equal layers in log-pressure, ranging from  $10$ – $10^{-8}$  bar. Second, we fit for the 10 bar planet radius, rather a reference pressure, as our hydrostatic boundary condition (uniform from  $2.0$ – $2.8 R_\oplus$ ). We retrieve the planetary log-surface gravity as a proxy for the mass uncertainties (Gaussian with mean 3.19 and standard deviation 0.17, both in cgs units). Third, we restrict our aerosol model to an opaque cloud deck (with a log-uniform pressure prior of  $1.0$ – $10^{-7}$  bar). Fourth, we sample the opacities at a slightly lower resolution of  $R = 60,000$ , due to GPU memory limitations. We include the following molecules in our BeAR retrievals, with their associated line lists:  $\text{H}_2\text{O}$  (Polyansky et al. 2018),  $\text{CH}_4$  (Yurchenko & Tennyson 2014),  $\text{NH}_3$  (Coles et al. 2019),  $\text{HCN}$  (Harris et al. 2006; Barber et al. 2014),  $\text{CO}$  (Li et al. 2015),  $\text{CO}_2$  (Yurchenko et al. 2020), DMS

<sup>7</sup> Through the JWST Transiting Exoplanet Early Release Science Program, we found a useful heuristic that  $R_{\text{model}} = 20,000$  suffices for  $R_{\text{data}} = 100$  and  $R_{\text{model}} = 60,000$  suffices for  $R_{\text{data}} \sim 3,000$  (pixel-level).

<sup>8</sup> <https://newstrangeworlds.github.io/BeAR>

(Sharpe et al. 2004), CS<sub>2</sub> (Sharpe et al. 2004), CH<sub>3</sub>Cl (Owens et al. 2018), and OCS (Wilzewski et al. 2016). We also include collision-induced absorption from H<sub>2</sub>-H<sub>2</sub> (Abel et al. 2011) and H<sub>2</sub>-He (Abel et al. 2012), alongside Rayleigh scattering from H<sub>2</sub> (Vardya 1962). Our retrievals assume free chemistry, meaning the molecular abundances (aside from H<sub>2</sub> and He) are retrieved independently, making no assumptions about chemical processes. The abundances are drawn from log-uniform prior distributions, ranging from volume mixing ratios of 10<sup>-12</sup> to 0.3. The remaining atmosphere is filled with H<sub>2</sub> and He, assuming a solar He/H<sub>2</sub> ratio of 0.17 (Asplund et al. 2009). Finally, we include the effects of stellar contamination using a two-heterogeneity model with five free parameters: the stellar photosphere temperature (following a Gaussian prior with a mean of 3457 K and a standard deviation of 39 K — corresponding to the effective temperature values from Cloutier et al. 2017); the faculae fraction (uniform from 0–0.5) and temperature difference relative to the photosphere (uniform from 0–1000 K); and equivalent parameters for spots (with a temperature difference uniform from -1500–0 K). The stellar contamination is calculated assuming blackbodies for the photosphere and active regions. Alongside the atmospheric and stellar parameters described above, our BeAR retrievals account for possible offsets between different filters and instruments (e.g., Yip et al. 2021; Alderson et al. 2023) by fitting two offsets — one between NIRISS SOSS and NIRSpec G395H, and one between the NRS1 and NRS2 filters of NIRSpec G395H (both uniform from -100–100 ppm). Table 3 provides a full comparison between our BeAR and POSEIDON retrieval setups, alongside that used in Madhusudhan et al. (2023).

We applied our BeAR retrievals to a subset of our re-analyzed NIRISS SOSS and NIRSpec G395H data. Specifically, we focus on low-resolution data combinations using a single reduction code ( $R \approx 100$  FIREFLY and exoTEDRF data for both NIRISS and NIRSpec) and the highest-resolution pixel-level data produced by a common reduction code. Therefore, we considered 4 data combinations with BeAR. For each data combination, we ran 4 retrievals, a reference model and 3 nested models, as above, to calculate detection significances of CH<sub>4</sub>, CO<sub>2</sub> and DMS.

## 4.2. Retrieval Results

### 4.2.1. Molecular Detection Significances

Our atmospheric retrieval analysis confirms a strong detection of CH<sub>4</sub> in K2-18 b’s atmosphere. Figure 5 shows a grid of 180 Bayesian model comparisons from POSEIDON, colored by the detection significance corre-

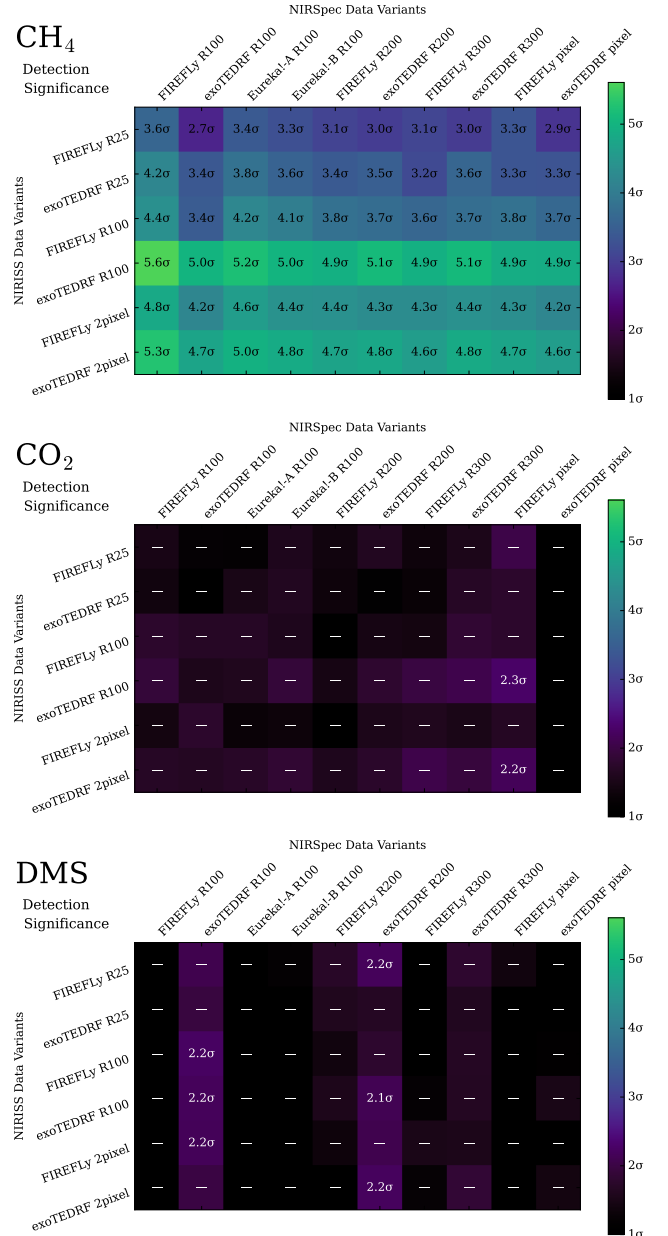


**Figure 5.** Detection significances of CH<sub>4</sub>, CO<sub>2</sub>, and DMS from POSEIDON retrievals of K2-18 b’s JWST NIRISS SOSS + NIRSpec G395H transmission spectrum. Each grid cell represents a Bayesian model comparison between two retrievals, one with and one without a molecule, for a specific NIRISS SOSS and NIRSpec G395H data variant pair. The data variants are ordered with increasing spectral resolution to the right (for NIRSpec) and down (for NIRISS). The cells are colored and annotated according to the detection significance equivalent to the calculated Bayes factor (e.g., Trotta 2008; Benneke & Seager 2013). Bayes factors < 3 (equivalent to < 2.1 $\sigma$ ), corresponding to no evidence on the Jeffreys’ scale, are denoted by ‘-’. Our retrievals demonstrate strong evidence for CH<sub>4</sub>, but find no reliable statistical evidence for CO<sub>2</sub> or DMS in K2-18 b’s atmosphere.

sponding to each Bayes factor, spanning every data combination produced in this study. We see that  $\text{CH}_4$  is detected at  $> 2.7\sigma$  for all data combinations, with most combinations favoring  $\text{CH}_4$  at  $> 4\sigma$ . Considering our  $\text{CH}_4$  significances as independent draws from the distribution of possible data-level choices, we find a detection significance of  $4.2_{-0.9}^{+0.7}\sigma$ . While slightly lower than the  $5\sigma$  detection reported in Madhusudhan et al. (2023), we consider these results a strong confirmation that  $\text{CH}_4$  is robustly present in K2-18 b’s atmosphere.

Figure 5 additionally contains a wealth of information pertaining to the sensitivity of  $\text{CH}_4$  detections to both data resolution and reduction code. First, we see that increasing the NIRISS SOSS data resolution from  $R \approx 25$  to  $R \approx 100$  leads to a clear increase in the  $\text{CH}_4$  detection significances from  $\sim 3.3\sigma$  to  $\sim 4.5\sigma$ . This behavior is not surprising, since  $R \approx 25$  NIRISS data makes it harder for retrievals to uniquely resolve  $\text{CH}_4$  bands from other molecules with similar absorption features (especially  $\text{H}_2\text{O}$ ), resulting in lower Bayes factors and hence lower significances. We generally find higher  $\text{CH}_4$  significances for the NIRISS data with **exoTEDRF** (mean significances of  $3.5\sigma$ ,  $5.0\sigma$ , and  $4.8\sigma$  for the  $R \approx 25$ ,  $R \approx 100$ , and pixel-level data, respectively) compared with **FIREFLY** ( $3.1\sigma$ ,  $3.8\sigma$ , and  $4.4\sigma$ , for the same data resolutions). We note that the pixel-level **exoTEDRF** results are in good agreement with the  $R \approx 100$  **exoTEDRF** results, while the  $R \approx 100$  **FIREFLY** results lead to notably lower detection significances. A potential reason for the discrepancies at  $R \approx 100$ , but not at pixel-level, could be differences in how each reduction code handles systematics and limb darkening, which manifests more at lower resolutions than at pixel-level.

We do not find any reliable or significant evidence for  $\text{CO}_2$  or DMS in the observed transmission spectrum of K2-18 b. Figure 5 demonstrates that almost every combination of NIRISS and NIRSpec data results in no evidence for  $\text{CO}_2$  or DMS (Bayes factors  $< 3$ , denoted by ‘—’ in Figure 5, are “not worth mentioning” according to the Jeffreys’ scale of Bayesian model comparison — see Trotta 2008). Even choosing the data combination with the maximum Bayes factors results in 4.2 for  $\text{CO}_2$  ( $2.3\sigma$ ) and 3.9 for DMS ( $2.2\sigma$ ), which are considered as “weak evidence at best” on the Jeffreys’ scale. However, one can see in Figure 5 that it is only the coupling between the **FIREFLY** pixel-level NIRSpec data and the **exoTEDRF**  $R \approx 100$  or 2-pixel NIRISS data that result in any marginal evidence for  $\text{CO}_2$ . Similarly, even the marginal evidence for DMS is only present for  $R \approx 100$  or  $R \approx 200$  NIRSpec data from **exoTEDRF** and disappears for higher data resolutions. Therefore, any marginal evidence for  $\text{CO}_2$  or DMS depends on either

the choice of a specific data reduction code or insufficient data resolution. In Appendix A, we demonstrate that if we run retrievals on the data from Madhusudhan et al. (2023) then we recover a maximum significance of  $2.5\sigma$  for  $\text{CO}_2$  — this shows that the claimed  $\text{CO}_2$  detection arises from the specific data treatments in that study. Our results demonstrate that, contrary to the findings of Madhusudhan et al. (2023), there is no robust detection of  $\text{CO}_2$  from K2-18 b’s initial NIRISS SOSS and NIRSpec G395H transmission spectra, nor are there even potential signs of DMS. Figure 5 offers a clear visual representation of the difference between a robust detection and non-detections.

Our **BeAR** retrievals similarly find strong detections of  $\text{CH}_4$  and non-detections of  $\text{CO}_2$  and DMS. For the **FIREFLY** reductions, for  $\text{CH}_4$  we obtain detection significances of  $3.5\sigma$  and  $4.5\sigma$  for the pixel-level and  $R \approx 100$  retrievals, respectively. For  $\text{CO}_2$  and DMS, the Bayes factor is  $< 3$  for both resolutions, corresponding to no evidence. The results are extremely similar for the **exoTEDRF** reductions, for which we obtain  $3.8\sigma$  and  $4.4\sigma$  for  $\text{CH}_4$  for the pixel-level and  $R \approx 100$  retrievals, respectively, and Bayes factors  $< 3$  for  $\text{CO}_2$  and DMS. These results are in good agreement with our retrievals using **POSEIDON** (Figure 5), indicating that our conclusions are robust to the choice of retrieval code.

Having established that only  $\text{CH}_4$  is evidenced by K2-18 b’s JWST NIRISS SOSS and NIRSpec G395H transmission spectrum, we now turn to present abundance constraints consistent with these data.

#### 4.2.2. Molecular Abundance Constraints

We first consider the sensitivity of the atmospheric abundances of  $\text{CH}_4$ ,  $\text{CO}_2$ , and DMS to the choice of data reduction code, data resolution, and retrieval code. Figure 6 provides a pairwise retrieval comparison of how these three factors can affect the inferred atmospheric composition of K2-18 b. First, we highlight a comparison between **POSEIDON** retrievals of the lowest-resolution **FIREFLY** and **exoTEDRF** data ( $R \approx 25$  NIRISS;  $R \approx 100$  NIRSpec). We selected these combinations to allow a clear demonstration of why the **exoTEDRF** NIRSpec  $R \approx 100$  data leads to weak evidence of DMS (per Figure 5) but **FIREFLY** does not. We see in Figure 6 (top panel) that several **exoTEDRF** data points near  $3.5\mu\text{m}$  and  $4.9\mu\text{m}$  have greater transit depths than **FIREFLY**, which coincide with opacity maxima for DMS. These transit depth differences result in a peak in the DMS mixing ratio posterior near  $\log_{10} X_{\text{DMS}} \sim -4$  for **exoTEDRF**, but an upper limit for **FIREFLY**. The non-robustness of this DMS inference can be seen in the second pairwise comparison in Figure 6 (middle panel),



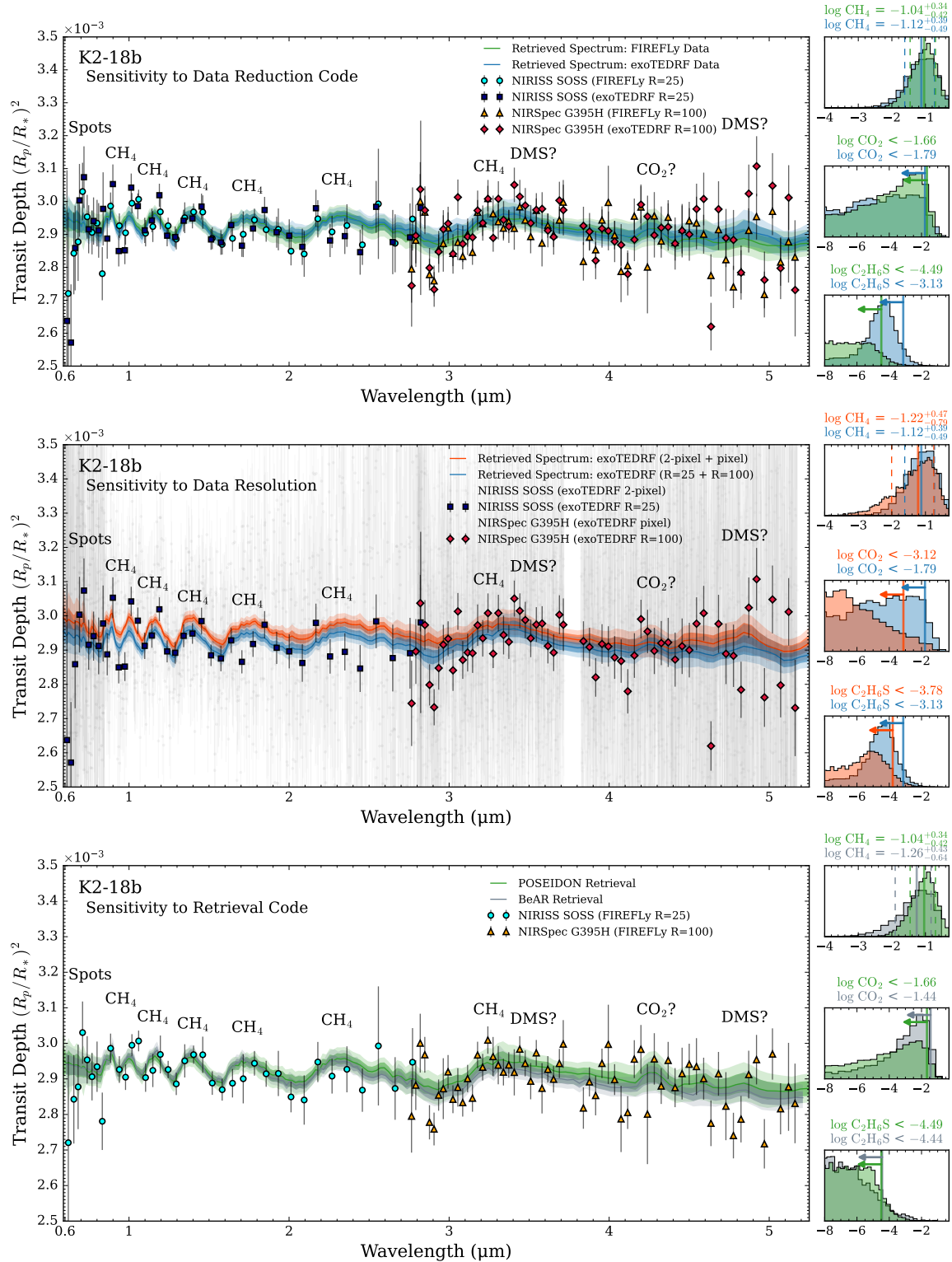


**Figure 6.** Sensitivity of K2-18b's atmospheric composition to different data treatments and retrieval configurations. Top: comparison between POSEIDON retrievals of data reduced by the FIREFLY and exoTDRF pipelines. Middle: comparison between POSEIDON retrievals of low-resolution (NIRISS SOSS:  $R \approx 25$ , NIRSpec G395H:  $R \approx 100$ ) and high-resolution (pixel-level) exoTDRF data. Bottom: comparison between the retrieval codes POSEIDON and BeAR on FIREFLY data. The retrieved model transmission spectra, plotted at  $R \approx 100$  for clarity, show the median (solid lines) and  $\pm 1\sigma$  and  $\pm 2\sigma$  credible regions (contours) corresponding to the dataset(s) shown in each panel. The median retrieved offsets have been applied to the NIRSpec G395H NRS1 and NRS2 datasets. Right: the retrieved CH<sub>4</sub>, CO<sub>2</sub>, and DMS abundances corresponding to each retrieval. Our retrievals find broadly consistent CH<sub>4</sub> abundances, indicating a robust detection (the median and  $\pm 1\sigma$  abundance constraints are represented by solid and dashed lines, respectively). However, any suggestions of CO<sub>2</sub> and DMS depend on the specific data reduction and data resolution, indicating unreliable inferences (hence the 95% upper limits, represented by arrows).

where we show that our retrieval of the highest resolution `exoTEDRF` data (2-pixel for NIRISS; pixel-level for NIRSpec) no longer favors DMS. We note that the higher model transit depths for the pixel-level retrieval arise from a higher mean transit depth in the `exoTEDRF` NIRISS data compared to the  $R \approx 25$  data variant (resulting in smaller offsets between the NIRISS and NIRSpec data for the pixel-level retrieval). Finally, we demonstrate the excellent agreement between POSEIDON and BeAR in Figure 6 (lower panel). This shows that our main results ( $\text{CH}_4$  abundance constraints, upper limits on the  $\text{CO}_2$  and DMS abundances) are robust to the different atmospheric modeling and retrieval configuration choices made by POSEIDON and BeAR (Table 3). We additionally provide the full corner plots from our POSEIDON and BeAR retrieval grids as supplementary material on Zenodo: [doi:10.5281/zenodo.14735688](https://doi.org/10.5281/zenodo.14735688).

Next, we consider the molecular abundance constraints from our full collection of POSEIDON retrievals. For this purpose, we seek a way to combine the posterior distributions corresponding to each of the 60 data combinations. Given the identical parameter space of each of the 60 reference model retrievals, we can combine the samples from each retrieval to produce a single ensemble posterior. This technique essentially marginalizes over two additional dimensions, NIRISS and NIRSpec data-level choices, and thereby folds the impacts of three different data reduction codes and different data resolutions into a single set of atmospheric abundance constraints. To our knowledge, this conceptually simple — but computationally expensive — technique is novel for atmospheric inferences from JWST data. We present our ensemble posterior for K2-18 b’s atmospheric composition, spanning over 30 million likelihood evaluations, in Figure 7.

$\text{CH}_4$  is the only molecule with an abundance lower limit — indicating a robust detection — in Figure 7. Our ensemble posterior finds a well-constrained abundance of  $\log_{10} \text{CH}_4 = -1.15^{+0.40}_{-0.52}$ , which is consistent with the value of  $-1.74^{+0.59}_{-0.69}$  reported in Madhusudhan et al. (2023) (see also Appendix A). This high abundance of  $\text{CH}_4$  in K2-18 b’s atmosphere,  $7^{+11}_{-5}\%$  by volume, is consistent with a metal-enriched mini-Neptune (as discussed in Section 5.1) and is similar to the deep abundance of  $\text{CH}_4$  on Neptune ( $4 \pm 1\%$ ; Karkoschka & Tomasko 2011).

We report upper limits on the abundances of  $\text{CO}_2$  and DMS in K2-18 b’s atmosphere:  $\log_{10} \text{CO}_2 < -1.70$  and  $\log_{10} \text{DMS} < -3.70$ . The ensemble posteriors for these molecules in Figure 7 show a weak peak for DMS, alongside an even more marginal peak for  $\text{CO}_2$ , which reflects the combination of retrieval results from different data

combinations where a few favor including DMS or  $\text{CO}_2$  but most do not (e.g. Figure 6, top panel). The blending of possible  $\text{CO}_2$  and DMS posteriors from all our data variants into a single conservative posterior, guarding against statistical artifacts from specific data-level assumptions (e.g. Figure 5), is a distinct strength of our ensemble posterior method. We stress that these upper limits do not imply that either molecule is absent at *any* atmospheric abundance, as abundance lower than our 95% limits are still compatible with the present JWST transmission spectrum. Indeed, some mini-Neptune scenarios predict  $\text{CO}_2$  abundances of  $\log_{10} \text{CO}_2 \sim -3$  (Section 5.1), consistent with our upper limit. Consequently, our non-detection of  $\text{CO}_2$  with these data does not preclude more sensitive upcoming data (e.g. JWST Program GO-2372, PI: Renyu Hu) from eventually identifying  $\text{CO}_2$  and other trace species in K2-18 b’s atmosphere.

We additionally report upper limits on several gases important for understanding the atmospheres and interiors of sub-Neptunes. Water and ammonia are depleted from the gas phase (95% upper limits of  $\log_{10} \text{H}_2\text{O} < -3.05$  and  $\log_{10} \text{NH}_3 < -5.25$ ), which can be explained by cloud condensation (Hu et al. 2021; Madhusudhan et al. 2023) and dissolution into a deep magma ocean (Shorttle et al. 2024), respectively. We show in Section 5 that neither of these non-detections requires a surface liquid ocean on K2-18 b. Alongside our non-detection of DMS, we find upper limits on four other gases proposed as biosignatures (e.g., Segura et al. 2005; Seager et al. 2013; Schwieterman et al. 2018; Madhusudhan et al. 2021):  $\log_{10} \text{CS}_2 < -3.29$ ,  $\log_{10} \text{CH}_3\text{Cl} < -2.11$ ,  $\log_{10} \text{OCS} < -3.09$ , and  $\log_{10} \text{N}_2\text{O} < -2.98$ . Therefore, there is no evidence of biosignatures in the JWST NIRISS SOSS + NIRSpec G395H transmission spectrum of K2-18 b.

#### 4.2.3. Atmospheric Temperature

K2-18 b’s transmission spectrum is consistent with an isothermal upper-atmosphere temperature structure. While our POSEIDON retrievals allow for temperature gradients, our top-of-atmosphere temperature ( $T_{10 \text{ mbar}} = 173^{+64}_{-51} \text{ K}$ ) is consistent with the temperature at significantly higher pressures (e.g.  $T_{10 \text{ mbar}} = 193^{+65}_{-49} \text{ K}$ , see Figure 7). Our temperature constraints are consistent with Madhusudhan et al. (2023), who reported  $T_{10 \text{ mbar}} = 242^{+57}_{-79} \text{ K}$ . Since low-resolution transmission spectra only probe atmospheric pressures from  $\sim 10^{-5}$ – $10^{-1}$  bar, we note that the lack of any detected temperature gradient does not preclude steep adiabatic temperature gradients at deeper pressures.

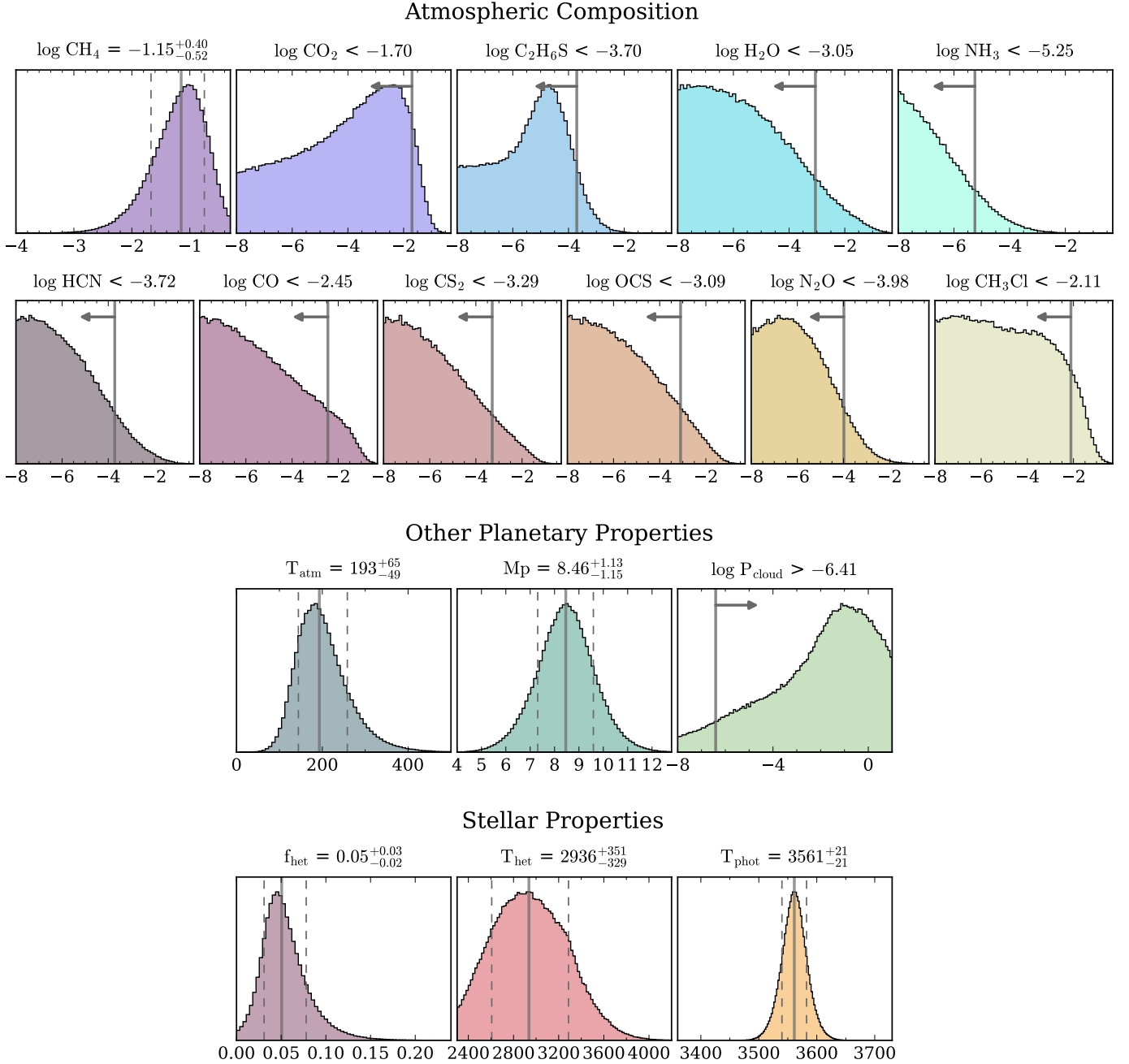


**Figure 7.** Atmospheric, planetary, and stellar properties retrieved from K2-18 b's JWST NIRISS SOSS + NIRSpec G395H transmission spectrum by POSEIDON. Top block: retrieved atmospheric  $\log_{10}$  volume mixing ratios. Middle row: retrieved 10 mbar temperature, planetary mass, and cloud-top pressure. Bottom row: retrieved starspot (stellar heterogeneity) coverage fraction, starspot temperature, and stellar photosphere temperature. Parameters with clear upper and lower limits are annotated with the median and  $\pm 1\sigma$  credible interval (vertical and dashed lines). Non-detected molecules are annotated with upper limits representing the 95% credible interval (solid lines and left-pointing arrows). The non-detected cloud pressure is annotated with the lower limit representing the 5% credible interval (solid line with right-pointing arrow). The POSEIDON posteriors shown here are the combined retrieval results from 60 NIRISS SOSS and NIRSpec G395H data variants (spanning different reduction codes and final spectral resolution); thus, they represent the marginalized posterior over all data-level analysis choices considered in this study.

#### 4.2.4. Aerosols

We do not detect any evidence of aerosols in K2-18 b’s atmosphere. Figure 7 highlights that any optically-thick cloud deck must reside deep in the atmosphere, but the present JWST data can only place a very loose lower limit ( $\log_{10}(P/\text{bar}) > -6.41$ ). Our retrievals offer no constraints (either upper or lower limits) on the haze parameters or the terminator cloud fraction. Madhusudhan et al. (2023) similarly reported a non-detection of aerosols. Since scattering hazes can play an important role in moderating K2-18 b’s temperature under a hycean interpretation (Madhusudhan et al. 2023), our non-detection of a haze — based on data that include the bluer 0.6–0.8  $\mu\text{m}$  2<sup>nd</sup> order NIRISS SOSS data that are in theory more sensitive to a haze slope — provides important context for the viability of a liquid water ocean. However, given the present signal-to-noise ratio at the shortest wavelengths (e.g. Figure 6), additional observations with NIRISS SOSS would be required before hazes can be definitively ruled out.

#### 4.2.5. Planetary Mass

Our retrieval analysis also offers an updated constraint on K2-18 b’s planetary mass. Transmission spectra can, in principle, constrain an exoplanet’s mass through the amplitude and shape of absorption features (de Wit & Seager 2013), with the tightest constraints arising for cloud-free atmospheres (Batalha et al. 2019a). Given the lack of detected aerosols in K2-18 b’s transmission spectrum, this technique provides the opportunity to potentially improve the mass determination from radial velocity measurements (Cloutier et al. 2019; Radica et al. 2022a). Our POSEIDON retrievals adopt a Gaussian prior on the planetary mass to reflect our existing knowledge from radial velocities ( $8.63 \pm 1.35 M_{\oplus}$ ; Cloutier et al. 2019), such that any additional information in the JWST spectrum would result in a tighter constraint. Our ensemble posterior (Figure 7) offers a new constraint on K2-18 b’s mass,  $8.46^{+1.13}_{-1.15} M_{\oplus}$ , which slightly decreases the mass uncertainty from 16% to 13%. This updated mass determination can be used to inform interior structure models of K2-18 b.

#### 4.2.6. Unocculted Starspots

By including stellar contamination in our retrievals, we obtain constraints of unocculted active regions on K2-18. Our ensemble posterior (Figure 7) generally indicates a small coverage fraction ( $5^{+3}_{-2}\%$ ) of cool spots ( $\Delta T \approx 500 \pm 350$  K cooler than the photosphere). While this may appear contrary to the finding of no stellar contamination reported by Madhusudhan et al. (2023), we note that our inclusion of the 2<sup>nd</sup> order NIRISS

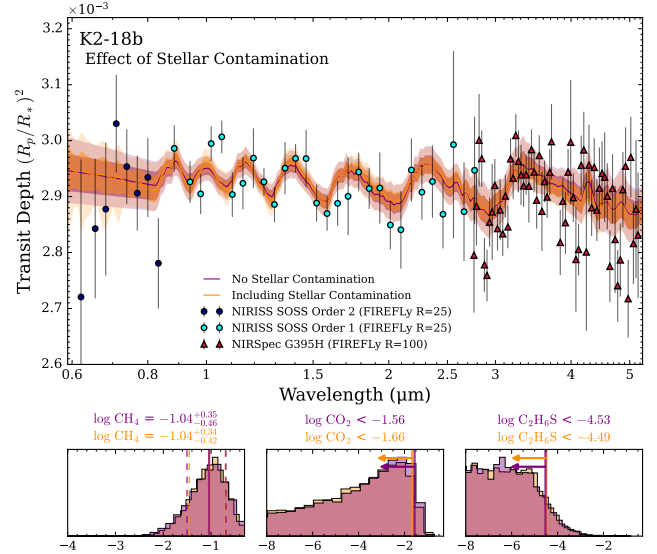


**Figure 8.** Influence of stellar contamination on K2-18 b retrievals. Top: two POSEIDON retrieval models for the low-resolution FIREFLY data variant, one including a planetary atmosphere and stellar contamination (orange) and an alternative atmosphere-only model (purple). Bottom: corresponding posterior distributions for the CH<sub>4</sub>, CO<sub>2</sub>, and DMS abundances. The inferred atmospheric composition is insensitive to whether or not stellar contamination is included.

data provides coverage of shorter wavelengths where starspot contamination is more prominent (e.g., Lim et al. 2023; Fournier-Tondreau et al. 2024a; Cadieux et al. 2024; Radica et al. 2024a). We investigated the impact of stellar contamination by running several additional POSEIDON retrievals with stellar contamination excluded, with one example shown in Figure 8. We find that this potential low-level stellar contamination does not notably affect the inferred atmospheric composition of K2-18 b. However, given the stochastic nature of the transit light source effect, further repeat observations will be necessary to confirm this. Therefore, while it is likely that future transit observations of K2-18 b will be able to be stacked to increase the transmission spectrum precision, it would be prudent to continue observations with NIRISS SOSS (as opposed to only observing at longer wavelengths) to further constrain the possibility of stellar heterogeneities.

With our inferences from K2-18 b’s JWST transmission spectrum in hand, we next turn to an assessment of viable atmospheric and interior structures.

## 5. ATMOSPHERE AND INTERIOR MODELING: THE NATURE OF K2-18 b

K2-18 b's mass and radius allow a wide range of planetary structures, with the most widely considered scenarios being a mini-Neptune or a hycean world. Here we conduct a careful assessment of the range of planetary structures and climates compatible with our retrieved composition (Section 5.1). We also calculate interior models to assess which planetary structures are compatible with the observed mass and radius (Section 5.2). We proceed to elucidate viable natures for K2-18 b.

### 5.1. Atmosphere Modeling

We first quantify the expected compositional and climate properties for K2-18 b across various proposed scenarios and compare them to our retrieved atmospheric abundance constraints. Our analysis builds upon a similar narrative to Wogan et al. (2024), but here we use our revised retrieved abundances to evaluate if a hydrogen-rich mini-Neptune or a hycean planet with a liquid water surface is favored. We consider four scenarios: (i) a mini-Neptune with water clouds; (ii) an oxygen-poor mini-Neptune; (iii) a hycean planet; and (iv) a supercritical ocean.

#### 5.1.1. Mini-Neptune with Water Clouds

First, we consider K2-18 b as a mini-Neptune with a thick hydrogen envelope. The key distinction from previous studies (Tsai et al. 2021a; Wogan et al. 2024; Cooke & Madhusudhan 2024) is that here we compute temperature profiles consistent with the disequilibrium composition predicted by photochemistry and vertical mixing. We simulate mini-Neptune atmospheres with two independent sets of coupled photochemical-climate models: (1) *Photochem* (v0.6.2, Wogan 2024; Wogan et al. 2024) & *PICASO* (v3.3.0, Batalha et al. 2024; Mukherjee et al. 2024); and (2) *VULCAN* (Tsai et al. 2017, 2021b) & *HELIOS* (Malik et al. 2017, 2019). For each simulation, we iterate between the photochemical and climate models, passing the chemical composition and temperature profiles between the codes until a photochemical-climate steady-state is achieved.

Figure 9 (upper panel) illustrates the temperature and chemical composition computed by our self-consistent models, assuming  $100\times$  solar metallicity, an intrinsic temperature of 60 K, and a uniform eddy diffusion coefficient ( $K_{zz}$ ) of  $10^7$  cm<sup>2</sup>/s (similar to Hu et al. 2021; Tsai et al. 2021a). The simulated CH<sub>4</sub> matches the retrieved abundance, while the modeled CO and CO<sub>2</sub> remain compatible with their respective 2- $\sigma$  upper limits of  $\log_{10}$  CO = -2.45 and  $\log_{10}$  CO<sub>2</sub> = -1.70. However, the modeled H<sub>2</sub>O and NH<sub>3</sub> exceed our inferred upper lim-

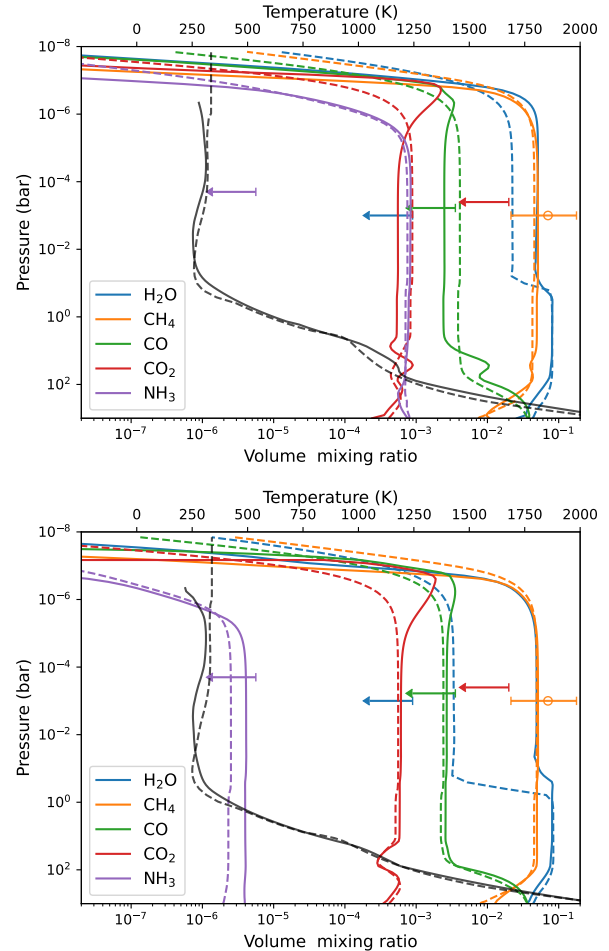


**Figure 9.** Self-consistent mini-Neptune models of K2-18 b's atmosphere. Upper panel:  $100\times$  solar metallicity case. Lower panel: the same metallicity, but with  $5000\times$  nitrogen depletion. The temperature (black lines) and composition profiles (colored lines) from *VULCAN-HELIOS* (solid lines) and *Photochem-PICASO* (dashed lines) with the  $1\sigma$  CH<sub>4</sub> constraint (orange error bar) and 95% upper limits for other molecules (arrows) from the ensemble retrieval posterior (Figure 7).

its. Cooke & Madhusudhan (2024) highlighted that K2-18 b's temperature as a mini-Neptune with  $100\times$  solar metallicity equilibrium composition is too high to condense enough water to meet the H<sub>2</sub>O upper limit, unless the stellar irradiation is artificially reduced by 40%. Our self-consistent calculations yield similar results, with the temperature remaining too warm and the H<sub>2</sub>O mixing ratio only reduced by a factor of a few due to condensation. The *Photochem-PICASO* model produces a slightly cooler temperature than *VULCAN-HELIOS* and, hence, a marginally lower water abundance. Without ad hoc irradiation reduction, the predicted H<sub>2</sub>O abundance exceeds the  $2\sigma$  upper limit by more than an order of magnitude for both simulations.

Secondly, the lack of detected  $\text{NH}_3$  is one of the main arguments against a mini-Neptune scenario, as  $\text{NH}_3$  is hypothesized to be present at detectable abundances ( $\log_{10} \text{NH}_3 \approx -3$ , see Figure 9) in a thick  $\text{H}_2$ -dominated atmosphere (Yu et al. 2021; Hu et al. 2021; Tsai et al. 2021a). A potential explanation for lower  $\text{NH}_3$  abundances, suggested by Shorttle et al. (2024), is that a reducing magma layer at the bottom of the gaseous envelope can efficiently dissolve nitrogen into the magma and hence deplete  $\text{NH}_3$  from the gas phase.

We explore the extent of nitrogen depletion required to explain our non-detection of  $\text{NH}_3$  in the lower panel of Figure 9. This second mini-Neptune model also has a  $100\times$  metallicity atmosphere, but with the total nitrogen depleted by a factor of 5000 (i.e.,  $\text{N}/\text{H} = 0.02\times$  solar) to account for nitrogen dissolution into a magma ocean. Such a low  $\text{N}/\text{H}$  ratio is close to, but within the lower bound, of expected nitrogen abundances under low magma oxygen fugacity (Shorttle et al. 2024; Rigby et al. 2024). This nitrogen-depletion factor lowers the atmospheric  $\text{NH}_3$  abundance at the pressure probed by transmission spectroscopy to  $< 10$  ppm, compatible with our retrieved 95% upper limit. Furthermore, a depleted  $\text{NH}_3$  abundance moves the stratosphere to a slightly higher pressure, which allows additional  $\text{H}_2\text{O}$  condensation (especially for the Photochem-PICASO model). The condensed water would form clouds around 0.1 bar, which is consistent with our retrieval constraints (see Figure 7) without damping the  $\text{CH}_4$  features over the NIRISS spectral range.

Should K2-18 b’s atmosphere possess a scattering haze (not considered in these models), the tropopause could be cooler than shown in Figure 9 with a corresponding lower  $\text{H}_2\text{O}$  abundance in the upper atmosphere (Piette & Madhusudhan 2020). However, a fine balance is needed to avoid producing a sufficiently strong haze that would dampen the shortest wavelength  $\text{CH}_4$  bands to a degree not seen in the JWST NIRISS transmission spectrum (Leconte et al. 2024). These considerations motivate additional modeling efforts under the mini-Neptune scenario to explore the sensitivity of the  $\text{H}_2\text{O}$  and  $\text{CH}_4$  abundance to aerosols. Nevertheless, these results demonstrate that a mini-Neptune scenario for K2-18 b, including nitrogen depletion from a basal magma ocean, is a plausible interpretation of our retrieved atmospheric abundances – though an additional albedo source is required to cold-trap water.

### 5.1.2. Mini-Neptune with high C/O ratio

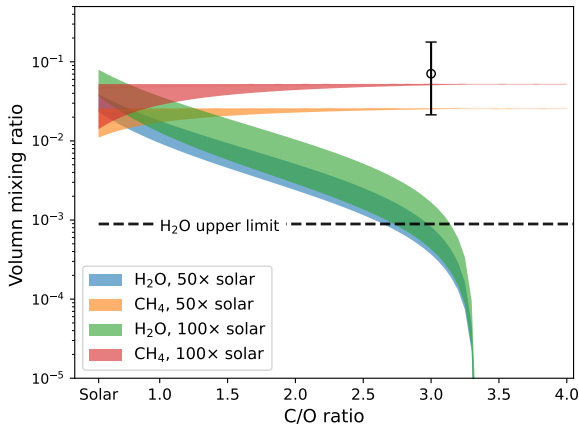
An alternative way to explain the low water abundance on K2-18 b is an oxygen-poor atmosphere with a high carbon-to-oxygen (C/O) ratio. K2-18 b’s current

orbit sits between the soot (Li et al. 2021) and water ice lines. If the planet migrated early to its present location within the ice line, it is plausible to form a carbon-rich and oxygen-poor envelope (Bergin et al. 2023; Yang & Hu 2024). We now consider the necessary C/O ratio to explain our non-detection of  $\text{H}_2\text{O}$  under the mini-Neptune scenario without an additional albedo source.

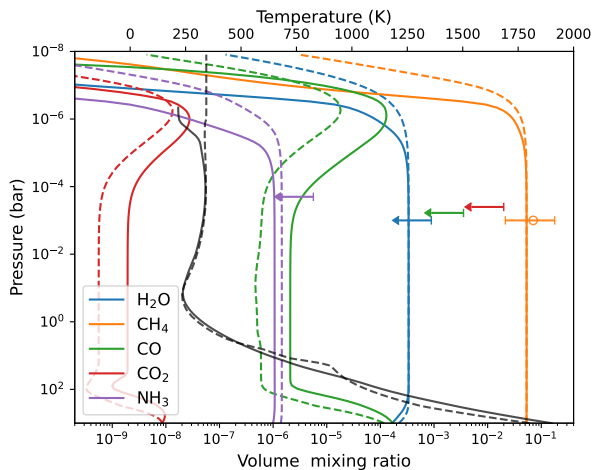
We first consider the simplest calculation of thermochemical equilibrium to illustrate the impact of the C/O ratio on the atmospheric  $\text{CH}_4$  and  $\text{H}_2\text{O}$  abundances. We perform these equilibrium calculations using Fastchem (Stock et al. 2022; Kitzmann et al. 2024) over the 1–100 bar pressure range in the deep atmosphere for a range of temperatures. Since this pressure range encloses possible quench points, these deep equilibrium abundances should broadly reflect the abundances from  $\sim 10^{-4}$ – $10^{-1}$  bar probed by the JWST spectrum — as confirmed by the rather uniform vertical distributions of  $\text{CH}_4$  and  $\text{H}_2\text{O}$  within this region in the absence of condensation (e.g. Figure 9; see also Tsai et al. 2021a; Yu et al. 2021; Cooke & Madhusudhan 2024).

Figure 10 shows the equilibrium  $\text{H}_2\text{O}$  and  $\text{CH}_4$  abundances as C/O varies. For simplicity, we fixed carbon and only changed the oxygen abundance. From the reasoning above, the equilibrium  $\text{H}_2\text{O}$  and  $\text{CH}_4$  abundances shown by the shaded regions in Figure 10 can be considered as the observable abundances. We see that  $\text{H}_2\text{O}$  decreases with increasing C/O — well-known from previous studies (e.g. Madhusudhan 2012; Mollière et al. 2015), as oxygen is preferentially sequestered within silicates — while  $\text{CH}_4$  remains nearly constant. We require  $\text{C}/\text{O} \gtrsim 3$  under equilibrium chemistry to lower the  $\text{H}_2\text{O}$  abundance below the 95% upper limit from our retrievals. This simple analysis suggests that an oxygen-depleted (high C/O ratio) mini-Neptune scenario, without effective water condensation, can be consistent with the observed  $\text{H}_2\text{O}$  and  $\text{CH}_4$  constraints. Having demonstrated  $\text{H}_2\text{O}$  depletion under equilibrium conditions, we next turn to self-consistent photochemical-climate models for a high C/O ratio.

Figure 11 shows our self-consistent photochemical climate models for K2-18 b under a high C/O ratio mini-Neptune scenario. The atmospheric properties are the same as Section 5.1.1 ( $100\times$  solar metallicity and  $5000\times$  N depletion), but with  $\text{C}/\text{O} = 3.25$ . We see that this oxygen-poor scenario naturally explains the retrieved  $\text{CH}_4$  abundance, alongside the non-detections of  $\text{H}_2\text{O}$  and  $\text{CO}_2$ , without invoking water condensation. Additionally,  $\text{CO}_2$  is negligible due to the scarcity of oxygen. Future observations with tighter constraints on  $\text{CO}_2$  could help differentiate this oxygen-depleted sce-



**Figure 10.** The equilibrium abundances of  $\text{H}_2\text{O}$  and  $\text{CH}_4$  as a function of C/O ratio. The shaded regions represent the range across pressures from 100–1 bar and temperatures from 800–1000 K, which cover the expected quench levels. The dashed line is the  $2\text{-}\sigma$  upper limit of  $\text{H}_2\text{O}$  from our combined retrieval analysis (Figure 7), and the open circle with an error bar represented our retrieved  $1\sigma$   $\text{CH}_4$  abundance.



**Figure 11.** Self-consistent mini-Neptune models for K2-18 b with an oxygen-depleted atmosphere. The atmospheric conditions and models are the same as the lower panel in Figure 9, but with  $\text{C/O} = 3.25$ .

nario from the cold-trapped water scenario discussed in Section 5.1.1.

### 5.1.3. Hycean Scenario

Previous arguments for hycean atmospheres have emphasized the presence of  $\text{CO}_2$  (Hu et al. 2021; Madhusudhan et al. 2023), since  $\text{CO}_2$  is expected to be the dominant carbon-bearing molecule. Its abundance, possibly ranging from  $\sim 1$  ppm to 1%, would be controlled by the solubility balance with the ocean (Hu et al. 2021;

Kite & Ford 2018). Conversely,  $\text{CH}_4$  is not photochemically stable in a small atmosphere. The high amount of  $\text{CH}_4$  ( $7_{-5}^{+11}\%$  from our retrievals) requires an additional supply, as demonstrated by Wogan et al. (2024).<sup>9</sup>

Given our non-detection of  $\text{CO}_2$  from K2-18 b's JWST transmission spectrum, while  $\text{CH}_4$  is robustly detected, we now consider whether a hycean scenario remains viable for K2-18 b. Since a hycean world possesses a thin  $\text{H}_2$  atmosphere to sustain a liquid water ocean,  $\text{CH}_4$  is expected to be photochemically converted to  $\text{CO}_2$  in the upper atmosphere, as discussed in Tsai et al. (2021a) and Wogan et al. (2024). To explore whether our  $\text{CH}_4$  and  $\text{CO}_2$  constraints fit the hycean scenario, we conducted a test to demonstrate how  $\text{CH}_4$  undergoes such conversion. We adopted a representative temperature profile for a hycean atmosphere from Tsai et al. (2024) (assuming a surface albedo of 0.3) and fixed the surface  $\text{CH}_4$  abundance at 1%, without any initial  $\text{CO}_2$ , representing a surface source continuously replenishing  $\text{CH}_4$ .

The resulting steady-state composition and the evolution are shown in the upper panel of Figure 12. Compared to the mini-Neptune scenario (Figures 9 and 11),  $\text{CO}_2$  and  $\text{CO}$  exhibit significantly higher abundances.

The evolution in the lower panel of Figure 12 illustrates the photochemical conversion of  $\text{CH}_4$  into  $\text{CO}_2$ , occurring on a geologically short timescale of  $\sim 10\text{--}100$  Myr. While the exact  $\text{CO}_2$  abundance depends on the precise levels of  $\text{H}_2\text{O}$ ,  $\text{CH}_4$ , and the surface temperature, the main takeaway of our test is that  $\text{CO}_2$  and  $\text{CO}$  are expected to have comparable abundances to  $\text{CH}_4$  within a  $\text{CH}_4$ -rich ( $\sim 1\%$ ) and thin atmosphere. Therefore, regardless of the source of  $\text{CH}_4$ , our well-constrained measured  $\text{CH}_4$  abundance, which lies above the 95% upper limits for both  $\text{CO}_2$  and  $\text{CO}$ , poses a challenge to reconcile the absence of  $\text{CO}_2$ , as  $\text{CH}_4$  should naturally convert to  $\text{CO}_2$  in a hycean atmosphere.

### 5.1.4. Supercritical Oceans

Should K2-18 b indeed have a water-rich interior covered by a hydrogen-helium envelope, as allowed by the observed mass and radius, the water will most likely exist in a supercritical state. This water phase arises from the greenhouse effect of  $\text{H}_2$  collision-induced absorption and the suppression of moist convection (Pierrehumbert 2023; Innes et al. 2023). Under such a super-runaway scenario, supercritical  $\text{H}_2\text{O}$  becomes miscible with  $\text{H}_2$ , as recently proposed by Benneke et al. (2024) for TOI-270 d. Without an appropriate climate model to track the transition from the supercritical ocean to the sub-

<sup>9</sup> See also Cooke & Madhusudhan (2024) for a thorough analysis of its dependence on various parameters.

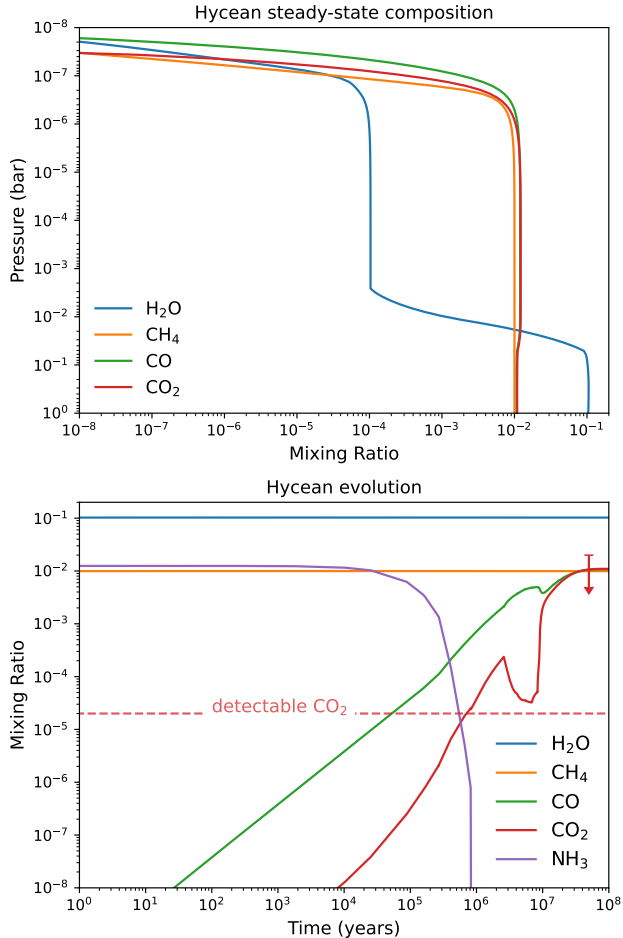


**Figure 12.** Atmospheric composition over time for a hycean scenario for K2-18 b. Upper panel: the steady-state composition profiles computed by VULCAN in our hycean scenario. Lower panel: the composition evolution at 0.1 bar. The red arrow corresponds to the  $2\sigma$  upper limit of  $\text{CO}_2$  from our retrievals, while the dashed line indicates the  $\text{CO}_2$  abundance required to produce a potentially detectable ( $\sim 100$  ppm) transmission feature at  $4.2\ \mu\text{m}$ .

critical upper atmosphere, it is unclear whether the temperature in the upper atmosphere allows a condensing layer can form to cold-trap water sufficiently to match our retrieved abundances.

Under a supercritical ocean scenario, a wide range of  $\text{CH}_4/\text{CO}_2$  ratios are allowed due to the unknown hydrogen molarity of K2-18 b (Luu et al. 2024). Consequently, it is not currently possible to conduct a detailed comparison between our retrieved  $\text{CH}_4$  abundance and the  $\text{CO}_2$  upper limit. Future observations that provide a tighter  $\text{CO}_2$  abundance constraint would offer useful insights into the potential thermal properties of a supercritical ocean.

## 5.2. Interior Structure Modeling

To aid in evaluating the possibility of a liquid water ocean on K2-18 b, we also construct several interior structure models of the planet which match its observed mass and radius ( $M_p = 8.63 \pm 1.35M_\oplus$ ,  $R_p = 2.61 \pm 0.087R_\oplus$ ). We use the mass and radius presented by Benneke et al. (2019) as the basis of our models<sup>10</sup>. We prefer this set of planet parameters due to the use of a Gaia parallax in their calculation, though we note that this mass is also consistent with the mass recovered from our atmosphere retrievals (Section 4.2.5). These interior models typically solve the equations of hydrostatic equilibrium, mass conservation, and the material equations of state. We used the Chabrier & Debras (2021) equation of state for H/He, the Mazevet et al. (2019) equation of state for water, ANEOS (Thompson 1990) for rock, and SESAME (Lyon & Johnson 1992) for iron, and thermally evolve the planet using atmosphere models from Fortney et al. (2007) to regulate heat flow from the interior.

We ran an MCMC to find compositions of the planet which match the planet’s observed properties, with the radius being of particular importance. Figure 13 shows the results as a ternary diagram of the mass fractions of rock (and iron, assuming an Earth-like ratio), water, and H/He (at a solar ratio). Our models find H/He makes up less than 10% of the planet’s mass, with the exact limit varying with the water abundance. Any of the models along the shaded region in Figure 13 fits the observed data, but we identify a few specific cases of interest (denoted with circles) for further discussion.

First, we consider the ice-poor case, which represents a typical Neptune-like planet that could form within the ice line, experiencing limited volatile accretion. In this case, approximately 6% of the mass must be H/He to match the observed radius. Such a planet features a deep envelope (due to the low gravity) on top of a solid (possibly molten) surface. If water is mixed into the envelope, it could result in water clouds and rain in the atmosphere, but the envelope is too deep to allow for a water ocean—any falling rain would pass into the supercritical phase and dissolve back into the ambient gas.

We next consider a more ice-rich structure, similar to outer solar system moons like Ganymede, with a 50-50 rock-to-water mass ratio and a structure that is stratified into separate layers (iron, rock, water, H/He). Such a planet requires a H/He envelope of about 1%

<sup>10</sup> If the planet were smaller, as reported in earlier work, the required water fraction for a thin H/He atmosphere drops to a more plausible range.



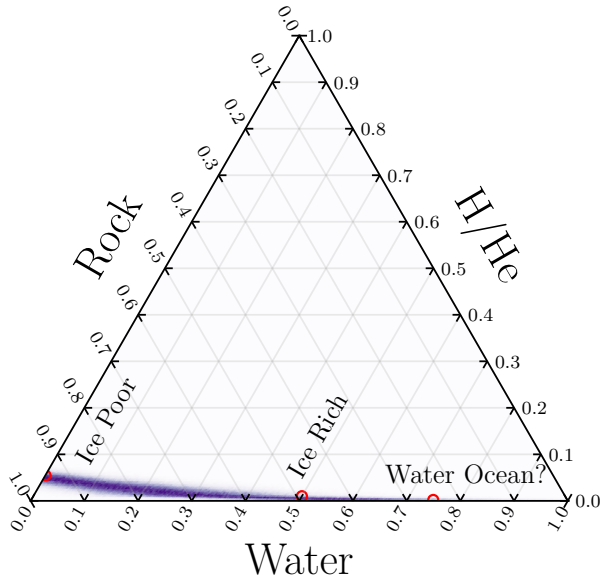


**Figure 13.** Potential interior compositions for K2-18 b. The ternary diagram shows the range of compositions (purple shading) consistent with K2-18 b’s mass, radius, the host star’s flux, and the system’s age from evolution models assuming fully separate layers. Three potential interiors are highlighted (red circles): (i) an ice-poor case, with an Earth-like composition that formed inside the ice line; (ii) an ice-rich case, with a Ganymede-like composition that formed outside the ice line; and (iii) a potential liquid water ocean. Only an unexpectedly high water fraction ( $> 70\%$ ) provides a sufficiently thin H/He layer to allow a liquid water ocean while still matching the observed radius.

of the planet’s mass. This results in the surface of the water layer occurring at about  $2.21 R_{\oplus}$ , a pressure of 100 kbar and a temperature of 3200 K. This temperature and pressure are high enough that the water is a supercritical fluid rather than a liquid phase.

To find a model which allows for a liquid water ocean, we must consider cases where the H/He layer is very thin. This possibility occurs only at very high water fractions, at least 70%, beyond what one would expect from planetary formation models. In this case, the water layer may extend to temperatures below the critical point of 647 K. However, the H/He adiabats produced by our evolution model reach this temperature at 220 bar, approximately passing through the critical point; thus, the H/He layer must not pressurize the surface to more than 220 bars. This corresponds with a H/He layer mass fraction of no more than about 0.03%. The stability of such an arrangement would depend strongly on the tendency of H/He to dissolve in water or the water to evaporate into the atmosphere (e.g. [Pierrehumbert 2023](#)), but that is outside the scope of this work.

Overall, we conclude that the most likely scenarios are the water-poor and Ganymede-like 50-50 composition models, neither of which features a water ocean. While we are able to construct models that feature a water ocean via heavy water enrichment, it is not clear how planetary formation could achieve such a high water fraction, nor whether the correspondingly thin H/He atmosphere would be stable. Given our non-detection of  $\text{CO}_2$  already disfavors the hycean model for K2-18 b (as discussed above in Section 5.1), our findings from these interior structure models are further evidence that K2-18 b’s structure is more Neptune-like in nature.

## 6. SUMMARY & DISCUSSION

The nature of K2-18 b is of broad interest for sub-Neptune studies and for exoplanet habitability. We have conducted a comprehensive reanalysis of the JWST transmission spectrum of K2-18 b from NIRISS SOSS and NIRSpec G395H. Our approach considers multiple well-tested data reduction and atmospheric retrieval codes to ensure robust and reliable results. Thus, our analysis assessed what can be confidently inferred about K2-18 b’s atmosphere and interior from the initial JWST observations. Our main results are as follows:

- We confirm the detection of  $\text{CH}_4$  in K2-18 b’s atmosphere ( $\approx 4\sigma$ ), with a volume mixing ratio of  $\log_{10} \text{CH}_4 = -1.15^{+0.40}_{-0.52}$  ( $7^{+11}\%$ ).
- We do not detect  $\text{CO}_2$  or DMS, contrary to the findings of [Madhusudhan et al. \(2023\)](#), placing 95% confidence upper limits of  $\log_{10} \text{CO}_2 < -1.70$  and  $\log_{10} \text{DMS} < -3.70$ .
- Any inferences of  $\text{CO}_2$  and DMS from these JWST data are unreliable and low-significance, exhibiting high sensitivity to specific data reduction codes and spectral resolutions (Figure 5).
- We present a simple technique to account for data-level choices across a grid of atmospheric retrievals. The resulting ‘ensemble posterior’ folds uncertainties from data processing into atmospheric inferences (Figure 7).
- K2-18 b’s retrieved atmospheric composition can be explained by a  $100\times$  solar mini-Neptune with an oxygen-poor and nitrogen depleted (e.g. from a magma ocean) composition.
- A hycean scenario for K2-18 b is only viable with an anonymously high water-to-rock ratio, a low H/He fraction, atmospheric hazes, and positing a substantial  $\text{CH}_4$  flux. We regard the necessary fine-tuning as an unlikely product of nature.

Based on our reanalysis, we summarize the observational constraints, challenges, and viability for each interpretation of K2-18 b in Table 4. Our findings raise many implications about K2-18 b, and the sub-Neptune population more broadly, as we now discuss.

### 6.1. *Plausibility of Hycean Scenarios for K2-18 b*

The debate surrounding K2-18 b’s nature since the initial JWST transmission spectrum was published has relied on the abundance constraints reported by Madhusudhan et al. (2023). Shorttle et al. (2024), Yang & Hu (2024), and Wogan et al. (2024) all showed that variations on mini-Neptune scenarios can explain the abundances from Madhusudhan et al. (2023). Wogan et al. (2024) additionally showed that an ‘inhabited’ hycean scenario (with a large CH<sub>4</sub> surface flux) is consistent with the chemical abundances from Madhusudhan et al. (2023), but favored the mini-Neptune scenario based on the fewer required assumptions. Recently, Cooke & Madhusudhan (2024) argued that a mini-Neptune scenario is “not compatible” with the retrieved abundances from Madhusudhan et al. (2023), but either lifeless or inhabited hycean scenarios are viable (depending on specific photochemical model assumptions). We argue here that much of this debate stems from taking the 1 $\sigma$  abundance constraints and upper limits from Madhusudhan et al. (2023) as the ‘ground truth’ composition of K2-18 b. Since the original retrieval analysis of Madhusudhan et al. (2023) did not explore the sensitivity of the atmospheric composition to data-level or retrieval-level assumptions, the abundances quoted in that study are not sufficiently reliable for discrimination of whether K2-18 b is a mini-Neptune or a hycean planet.

Our revised atmospheric composition of K2-18 b, accounting for data-level uncertainties, can be naturally explained by a mini-Neptune without requiring a liquid water ocean or life. Our non-detection of CO<sub>2</sub> lowers the potential CO<sub>2</sub>/CH<sub>4</sub> from  $\sim 1$  to  $< 0.3$  (95% confidence), whereas a high CO<sub>2</sub>/CH<sub>4</sub> is one of the primary lines of evidence for a liquid water ocean underlying a thin H<sub>2</sub>-dominated envelope (Hu et al. 2021; Tsai et al. 2021a). However, absence of evidence is not evidence of absence, and we stress that even mini-Neptune scenarios will contain some level of CO<sub>2</sub> (e.g., Figure 9 predicts  $\log_{10} \text{CO}_2 \sim -3$ ). Consequently, should future, more sensitive, JWST observations result in a CO<sub>2</sub> detection with an abundance lower than our upper limit ( $\log_{10} \text{CO}_2 < -1.7$ ), this would be an additional line of evidence *against* a hycean interpretation (see also Section 6.4). Our photochemical modeling offers an addi-

tional line of evidence against inhabited hycean scenarios. We show in Figure 12 that, even if one assumes a hycean scenario with a large unknown CH<sub>4</sub> flux (e.g. from methane-producing life), over time the atmospheric CO<sub>2</sub> and CO abundances would build to levels comparable to or above our upper limits. Consequently, our non-detections of CO<sub>2</sub> and CO are not consistent with the observed CH<sub>4</sub> abundance under an inhabited hycean scenario. Our results, therefore, render the mini-Neptune scenario the most likely interpretation for K2-18 b, given current observational constraints.

### 6.2. *Viability of a Biosphere on K2-18 b*

The potential evidence for a biosphere on K2-18 b has revolved around the large CH<sub>4</sub> abundance, requiring a significant surface flux under a hycean scenario, and the claimed spectral signature of the biosignature candidate DMS (Madhusudhan et al. 2023). Glein (2024) showed that metabolic reactions consuming CO<sub>2</sub> and/or DMS and producing CH<sub>4</sub> can potentially produce sufficient free energy to sustain a biosphere under a hycean scenario on K2-18 b. Glein (2024) highlighted that DMS should not strictly be considered a biosignature under this metabolic pathway, as DMS would be an energy source for methane-producing life rather than a product of life. The calculations from Glein (2024) took the retrieved abundances from Madhusudhan et al. (2023) as the present-day atmospheric composition and assumed K2-18 b is a hycean world.

Our revised atmospheric composition motivates a careful reassessment of the viability of methanogenesis on K2-18 b. Our non-detections of CO<sub>2</sub> and DMS prompt a re-assessment of whether a sufficient free energy source exists for methane-producing life under the metabolic pathway studied by Glein (2024), rendering it less plausible that K2-18 b sustains a biosphere. Further, our models in Figure 12 demonstrate that a hycean scenario with the CH<sub>4</sub> abundance we retrieve would necessarily have a high  $\sim 1\%$  CO<sub>2</sub> abundance that is in tension with our non-detection of CO<sub>2</sub>. Updated metabolic calculations, considering the minimum viable CO<sub>2</sub> abundance to sustain methanogenesis, will be required to assess whether a biosphere is ruled out by our revised atmospheric composition.

### 6.3. *On Establishing Robust and Reliable Molecular Detections from Atmospheric Retrievals*

Our revised atmospheric composition for K2-18 b demonstrates the critical importance of using multiple data reductions and multiple retrieval codes to establish which molecular detections are robust. In particular, our non-detection of CO<sub>2</sub> stands in stark contrast

**Table 4.** Mini-Neptune vs Hycean interpretations for K2-18 b

Scenario Constraint	mini-Neptune	Hycean
Climate	Compatible	Requires high-albedo aerosols
Interior	Compatible	Requires high water-to-rock ratio
H <sub>2</sub> O	Requires high-albedo aerosols or oxygen depletion	Requires high-albedo aerosols
CH <sub>4</sub>	Compatible	Requires external source
CO <sub>2</sub>	Compatible	Compatible, but not compatible with the coexistence with CH <sub>4</sub>
NH <sub>3</sub>	Requires high depletion from a basal magma ocean	Compatible through dissolution into the water

to the finding of a robust detection reported by [Madhusudhan et al. \(2023\)](#). However, this is not the first time that reported molecular detections in K2-18 b’s atmosphere have proven unreliable. Pre-JWST, multiple studies reported detections of H<sub>2</sub>O vapor from HST WFC3 transmission spectroscopy at compelling statistical significances:  $3.6\sigma$  ([Tsiaras et al. 2019](#)),  $3.9\sigma$  ([Benneke et al. 2019](#)), and  $3.3\sigma$  ([Madhusudhan et al. 2020](#)). We now know from the JWST spectrum of K2-18 b that the spectral feature seen by WFC3 was, in fact, CH<sub>4</sub> masquerading as H<sub>2</sub>O (likely due to WFC3 edge effects near  $1.7\mu\text{m}$ ). One naturally wonders how so many  $> 3\sigma$  retrieval ‘detections’ could prove unreliable. Thus, we examine here how future retrieval analyses can safeguard against overstating the statistical evidence of a molecular detection.

First, our grid of retrievals demonstrates that detection significances naturally possess their own uncertainty due to data-level assumptions. Figure 5 clearly illustrates a spread of CH<sub>4</sub> significances (clustered around  $4\sigma$ ) as a function of the data reduction code and the degree of spectral binning pre-retrieval. We propose that visualizations such as Figure 5 are a valuable tool to intuitively establish if a molecular detection is robust (as with CH<sub>4</sub>) or whether there is no reliable statistical evidence (as with CO<sub>2</sub> and DMS). An additional value of Figure 5 is the clear representation of lost information when retrieving NIRISS spectra at  $R = 25$  rather than  $R = 100$ , resulting in a significantly lower CH<sub>4</sub> detection significance, which suggests  $R = 100$  is a safe minimum resolution for inferring atmospheric properties from JWST transmission spectra. Our first takeaway is thus that the term ‘robust’ must be reserved for molecular detections that have been explicitly demonstrated to hold across multiple data reduction and retrieval codes.

Second, we argue that the retrieval literature tends to present overconfident detection significances and inconsistent terminology from Bayesian model comparisons. When establishing if a molecule is present in an atmosphere, the common practice is to conduct a Bayesian model comparison between a retrieval model containing

the molecule in question and one with it removed, calculate the Bayes factor, and then convert the Bayes factor into an ‘equivalent detection significance’ (using the inverse of Equation 27 in [Trotta 2008](#)). This approach was first introduced in the exoplanet retrieval context by [Benneke & Seager \(2013\)](#) and has been widely used in retrieval codes since (e.g., [Waldmann et al. 2015](#); [MacDonald & Madhusudhan 2017](#); [Welbanks & Madhusudhan 2021](#)). This procedure often provides useful insights, provided that: (i) both the Bayes factor and equivalent significance are provided, and (ii) well-defined terminology is adopted (e.g. the Jeffreys’ scale; see [Trotta 2008](#)). Not providing Bayes factors can produce overconfidence in a result due to common intuition for the meaning of an ‘ $N\sigma$ ’ result. For example, a Bayes factor of 3 corresponds to an equivalent significance of  $2.1\sigma$ , such that readers with frequentist training may construe the detection confidence to be a  $> 95\%$  result, when the model containing the molecule is actually only favored at a 3:1 odds ratio. Similarly, a claim of a  $3\sigma$  ‘detection’ from a Bayesian model comparison is only a Bayes factor of 21. [Trotta \(2008\)](#) highlights this issue by recommending that an ‘ $N\sigma$ ’ result should be thought of as an ‘ $(N - 1)\sigma$ ’ result to calibrate the frequentist measure for what the Bayes factor represents. Using the same logic, the ‘ $3\sigma$  detection’ of CO<sub>2</sub> in K2-18 b’s atmosphere reported by [Madhusudhan et al. \(2023\)](#) (without quoted Bayes factors) should be better thought of as a  $2\sigma$  result, for which the term ‘detection’ is too strong. It is for this reason that we report all Bayes factors  $< 3$  (equivalent to  $< 2.1\sigma$ ) as non-detections in Figure 5, since in reality these represent odds ratios closer to a ‘ $1\sigma$ ’ result via the ‘ $(N - 1)\sigma$ ’ calibration. Clearly, the conflation of a  $3\sigma$  equivalent significance from Bayesian model comparisons as being equivalent to a 99.7% detection confidence has proven especially problematic in the case of K2-18 b — as illustrated by the reported  $3\sigma$  ‘detections’ of both H<sub>2</sub>O ([Benneke et al. 2019](#); [Tsiaras et al. 2019](#); [Madhusudhan et al. 2020](#)) and CO<sub>2</sub> ([Madhusudhan et al. \(2023\)](#)) proving unreliable for K2-18 b following new observations and/or a revised retrieval analysis.

**Table 5.** Evidence for Molecular Signatures in K2-18 b’s JWST Transmission Spectrum

Molecule	This Work				Madhusudhan et al. (2023)				
	$\mathcal{B}_{\text{Ref}, i}$	$N\sigma$	$(N-1)\sigma$	Our Classification	$\mathcal{B}_{\text{Ref}, i}$	$N\sigma$	$(N-1)\sigma$	Their Classification	Our Classification
CH <sub>4</sub>	86–10 <sup>6</sup>	3.4–5.6 $\sigma$	2.4–4.6 $\sigma$	robust detection	11,000–44,000 <sup>†</sup>	4.7–5.0 $\sigma$	3.7–4.0 $\sigma$	robust detection	detection <sup>‡</sup>
CO <sub>2</sub>	0.6–4.2	< 2.3 $\sigma$	< 1.3 $\sigma$	no evidence	18–40 <sup>†</sup>	2.9–3.2 $\sigma$	1.9–2.2 $\sigma$	robust detection	moderate evidence
DMS	0.6–3.9	< 2.2 $\sigma$	< 1.2 $\sigma$	no evidence	~1–5 <sup>†</sup>	< 2.4 $\sigma$	< 1.4 $\sigma$	potential signs	no evidence

NOTE— $\mathcal{B}_{\text{Ref}, i}$  is the Bayes factor between models with and without molecule ‘i’. Our classification uses the following terms: ‘no evidence’ ( $\mathcal{B}_{\text{Ref}, i} < 3$ ), ‘weak evidence’ ( $3 < \mathcal{B}_{\text{Ref}, i} < 12$ ), ‘moderate evidence’ ( $12 < \mathcal{B}_{\text{Ref}, i} < 150$ ), ‘strong evidence’ ( $150 < \mathcal{B}_{\text{Ref}, i} < 600$ ), and ‘detection’ ( $\mathcal{B}_{\text{Ref}, i} > 600$ ). We reserve ‘robust detection’ for cases where a grid of retrievals across multiple data-level and model-level configurations all find  $\mathcal{B}_{\text{Ref}, i} > 600$ . For cases with some retrievals in a grid reside in one category but others fall in another category, the category label corresponding to most of the Bayesian model comparisons takes precedence over outliers. <sup>†</sup>Bayes factors were not provided by Madhusudhan et al. (2023), so we compute them from their quoted detection significances. The range of Bayes factors and significances quoted for Madhusudhan et al. (2023) correspond to their no offset, one offset, and two offsets cases. <sup>‡</sup>The CH<sub>4</sub> detection from Madhusudhan et al. (2023) does not qualify for the ‘robust’ label under our classification (even though  $\mathcal{B}_{\text{Ref}, i} > 600$ ), because their three retrievals only considered a single data reduction and retrieval code. We exclude  $R = 25$  NIRISS data from our quoted CH<sub>4</sub> Bayes factor and significance ranges, since data with  $R < 100$  incurs degeneracies that hinder CH<sub>4</sub> detectability (see Section 4.2.1 and Figure 5). Since the formula mapping Bayes factors to significances breaks down for low Bayes factors ( $\lesssim 3$ ), we quote only the highest significance for CO<sub>2</sub> and DMS.

We propose a straightforward classification scheme for communicating atmospheric retrieval results to mitigate these issues. Our starting point is the widely used Jeffreys’ scale, which speaks only to Bayes factors and not equivalent significances. We propose the following terms for low-statistical significances: ‘no evidence’ (Bayes factor  $< 3$ ), ‘weak evidence’ ( $3 < \text{Bayes factor} < 12$ ), ‘moderate evidence’ ( $12 < \text{Bayes factor} < 150$ ), and ‘strong evidence’ ( $150 < \text{Bayes factor} < 600$ ). We propose that a Bayes factor of 600 should represent the terminology transition from ‘evidence’ to ‘detection’, since this Bayes factor corresponds to an odds ratio of 99.8% — close to the traditional understanding of what a  $3\sigma$  result represents. Where ‘equivalent detection significances’ ( $N\sigma$ ) are reported, we advocate for also reporting the  $(N-1)\sigma$  significance. Finally, we propose that the term ‘robust detection’ be reserved for when the vast majority of Bayesian model comparisons for a molecule result in detections (i.e. Bayes factor  $> 600$  across a range of data-level and model-level configurations). Consequently, under our proposed classification scheme, a detection can *only* be considered robust if it is confirmed with multiple data reduction and retrieval codes.

Table 5 demonstrates the application of our molecular detection classification scheme to K2-18 b transmission spectra retrievals. We compare the Bayes factors, equivalent significances ( $N\sigma$ ), and calibrated significances ( $(N-1)\sigma$ ) from Madhusudhan et al. (2023) and our study. For the statistics from Madhusudhan et al. (2023), we also compare the detection terminology used in that study with our proposed classification under the scheme outlined above. First, let us consider the evidence for CH<sub>4</sub> in K2-18 b’s atmosphere. Figure 5 shows that 33/40 Bayesian model comparisons

with  $R_{\text{data}} \geq 100$  have  $N\sigma > 4.0\sigma$ , corresponding to Bayes factors  $> 600$ , which we regard as sufficient to ascribe CH<sub>4</sub> as a ‘robust detection’ (only the FIREFLY  $R = 100$  NIRISS data results in slightly lower significances). The CH<sub>4</sub> significances from Madhusudhan et al. (2023) meet our threshold for ‘detection’, but do not qualify as a ‘robust detection’ under our classification due to the use of a single data reduction code and a single retrieval code. Second, we see that the statistics reported for CO<sub>2</sub> by Madhusudhan et al. (2023) would be downgraded from ‘robust detection’ to ‘moderate evidence’ under our scheme, while our retrievals are classified as ‘no evidence’ for CO<sub>2</sub> (see Figure 5). The CO<sub>2</sub> classification demonstrates the utility of our proposed scheme, since the terminology readily discriminates between the reliable CH<sub>4</sub> inference and the significantly lower evidence for CO<sub>2</sub> in the JWST data from Madhusudhan et al. (2023) (see also Appendix A). Finally, we see that our classification scheme reports ‘no evidence’ for DMS for both our retrieval results and those from Madhusudhan et al. (2023). We highlight that the  $(N-1)\sigma$  column in Table 5 intuitively maps to the corresponding evidence classification for each molecule. We therefore advocate for adopting this more measured terminology for Bayesian model comparisons to avoid overstating the statistical evidence for molecular detections from JWST spectra of exoplanet atmospheres.

#### 6.4. Upcoming JWST Observations of K2-18 b

JWST will continue to observe spectra of K2-18 b, offering deeper insights into its atmospheric composition and internal structure. Two approved JWST programs are undertaking additional reconnaissance of K2-18 b’s atmosphere: Program GO-2372 (PI: Renyu Hu) and Program GO-2722 (PI: Nikku Madhusudhan). We

briefly discuss how our results relate to potential outcomes from these upcoming observations.

Program GO-2372 is in the process of observing 4 additional transits with NIRSpec G395H (with 2 pending at the time of writing) and 2 transits with NIRSpec G235H. These observations will significantly improve the observational precision over the 1.7–5.2  $\mu\text{m}$  wavelength range, offering additional sensitivity to the allowed abundances of molecules including  $\text{CH}_4$ ,  $\text{CO}_2$ , DMS, CO,  $\text{H}_2\text{O}$ ,  $\text{NH}_3$ , and HCN. The improved precision of these observations may allow the detection of  $\text{CO}_2$ , which would be expected for a mini-Neptune with a slightly lower abundance than our present  $\text{CO}_2$  upper limit (see Figures 7 and 9). Therefore, a detection of  $\text{CO}_2$  in new multi-transit JWST data is not at odds with the non-detection of  $\text{CO}_2$  from the single NIRISS SOSS and NIRSpec G395H transits we report here.

Program GO-2722 has observed two transits with MIRI LRS, which will offer the first transmission spectrum of K2-18 b from 5–12  $\mu\text{m}$ . These MIRI observations are anticipated to be especially sensitive to an array of sulfur-bearing species, including DMS and  $\text{CS}_2$  (Tsai et al. 2024). However, the low signal-to-noise ratio in MIRI LRS transmission spectra at wavelengths near 10  $\mu\text{m}$  (e.g., Powell et al. 2024), where DMS absorption has a strong absorption feature, may preclude any significant detections of DMS from MIRI LRS spectra alone. Therefore, any claim of a DMS detection from MIRI LRS observations must rely on additional information content from the shorter near-infrared wavelengths (i.e. NIRSpec G395H). Since our results demonstrate that the present JWST observations of K2-18 b do not provide any reliable statistical evidence for DMS, it is unlikely that these MIRI observations can further elucidate whether or not DMS is present in K2-18 b's atmosphere. We also stress that any inference of DMS must be considered in light of the poor availability of opacity data for this molecule, as the DMS cross section from Sharpe et al. (2004), used in all K2-18 b retrievals, has no temperature and pressure dependence. A variety of other chemical species with C-S bonds should also be considered when modeling MIRI LRS transmission spectra to cover degenerate interpretations. Consequently, we regard further observations of K2-18 b, beyond the two Programs described above, as being necessary to achieve the necessary sensitivity to unambiguously detect sulfur-bearing molecules in K2-18 b's atmosphere.

Our finding that K2-18 b is unlikely to be a hycean planet adds to the current dearth of observational evidence for the existence of hycean planets. A similar example is provided by JWST transmission spectra of the sub-Neptune TOI-270 d, which Holmberg & Madhusud-

han (2024) identified as a hycean candidate using only NIRSpec data, but Benneke et al. (2024), using both NIRISS and NIRSpec data, found is better explained via a miscible supercritical envelope. Future JWST observations of sub-Neptunes will have a valuable role to play in assessing the existence of hycean worlds. Our results provide a cautionary tale for the value of exploring a spread of data-level and model-level approaches when retrieving sub-Neptune transmission spectra, with the consequence that there is currently no spectroscopic evidence for the existence of hycean planets in nature.

#### ACKNOWLEDGMENTS

We thank Adina Feinstein, Duncan Christie, Emma Esparza-Borges, Evert Nasedkin, and Jake Taylor for helpful comments. We thank Hamish Innes for an illuminating discussion on the supercritical ocean scenario. This work is based in part on observations made with the NASA/ESA/CSA JWST. The data were obtained from the Mikulski Archive for Space Telescopes at the Space Telescope Science Institute, which is operated by the Association of Universities for Research in Astronomy, Inc., under NASA contract NAS 5-03127 for JWST. The specific observations analyzed can be accessed via DOI:10.17909/3ds1-8z15. S.P.S. is supported by the National Science Foundation Graduate Research Fellowship Program under Grant No. DGE2139757. Any opinions, findings, and conclusions or recommendations expressed in this material are those of the author and do not necessarily reflect the views of the National Science Foundation. R.J.M. is supported by NASA through the NASA Hubble Fellowship grant HST-HF2-51513.001, awarded by the Space Telescope Science Institute, which is operated by the Association of Universities for Research in Astronomy, Inc., for NASA, under contract NAS 5-26555. S.-M.T. acknowledges support from NASA Exobiology grant No. 80NSSC20K1437 and the University of California, Riverside. M.R. acknowledges support from the Natural Sciences and Engineering Research Council of Canada (NSERC). T.J.B. acknowledges funding support from the NASA Next Generation Space Telescope Flight Investigations program (now JWST) via WBS 411672.07.04.01.02. This research was supported in part through computational resources and services provided by Advanced Research Computing at the University of Michigan, Ann Arbor. This research has made use of the NASA Exoplanet Archive, which is operated by the California Institute of Technology, under contract with the National Aeronautics and Space Administration under the Exoplanet Exploration Program. This research has made use of NASA's Astrophysics Data System.

*Facilities:* JWST, MAST, ADS

*Software:*

Eureka! (Bell et al. 2022),  
 exoTEDRF (Feinstein et al. 2023; Radica et al. 2023),  
 FIREFLY (Rustamkulov et al. 2022, 2023),  
 BeAR (Kitzmann et al. 2020),  
 POSEIDON (MacDonald & Madhusudhan 2017; MacDonald 2023),  
 Photochem (Wogan 2024; Wogan et al. 2024),  
 PICASO (Batalha et al. 2019b; Mukherjee et al. 2023),

VULCAN (Tsai et al. 2017, 2021b),  
 HELIOS (Malik et al. 2017, 2019),  
 IPython (Perez & Granger 2007),  
 astropy (Astropy Collaboration et al. 2013, 2018, 2022),  
 batman (Kreidberg 2015),  
 dynesty (Speagle 2020),  
 ExoTiC-LD (Grant & Wakeford 2024),  
 lacosmic (van Dokkum 2001),  
 lmfit (Newville et al. 2024),  
 matplotlib (Hunter 2007),  
 numpy (Harris et al. 2020),  
 PyMultiNest (Feroz et al. 2009; Buchner et al. 2014),  
 scipy (Jones et al. 2024; Virtanen et al. 2020)

## REFERENCES

- Abel, M., Frommhold, L., Li, X., & Hunt, K. L. C. 2011, The Journal of Physical Chemistry A, 115, 6805, doi: [10.1021/jp109441f](https://doi.org/10.1021/jp109441f)
- . 2012, The Journal of Chemical Physics, 136, 044319, doi: [10.1063/1.3676405](https://doi.org/10.1063/1.3676405)
- Agrawal, A., & MacDonald, R. 2024, The Journal of Open Source Software, 9, 6894, doi: [10.21105/joss.06894](https://doi.org/10.21105/joss.06894)
- Albert, L., Lafrenière, D., René, D., et al. 2023, PASP, 135, 075001, doi: [10.1088/1538-3873/acd7a3](https://doi.org/10.1088/1538-3873/acd7a3)
- Alderson, L., Wakeford, H. R., Alam, M. K., et al. 2023, Nature, 614, 664, doi: [10.1038/s41586-022-05591-3](https://doi.org/10.1038/s41586-022-05591-3)
- Alderson, L., Batalha, N. E., Wakeford, H. R., et al. 2024, AJ, 167, 216, doi: [10.3847/1538-3881/ad32c9](https://doi.org/10.3847/1538-3881/ad32c9)
- Asplund, M., Grevesse, N., Sauval, A. J., & Scott, P. 2009, ARA&A, 47, 481, doi: [10.1146/annurev.astro.46.060407.145222](https://doi.org/10.1146/annurev.astro.46.060407.145222)
- Astropy Collaboration, Robitaille, T. P., Tollerud, E. J., et al. 2013, A&A, 558, A33, doi: [10.1051/0004-6361/201322068](https://doi.org/10.1051/0004-6361/201322068)
- Astropy Collaboration, Price-Whelan, A. M., Sipőcz, B. M., et al. 2018, AJ, 156, 123, doi: [10.3847/1538-3881/aabc4f](https://doi.org/10.3847/1538-3881/aabc4f)
- Astropy Collaboration, Price-Whelan, A. M., Lim, P. L., et al. 2022, ApJ, 935, 167, doi: [10.3847/1538-4357/ac7c74](https://doi.org/10.3847/1538-4357/ac7c74)
- Baines, T., Espinoza, N., Filippazzo, J., & Volk, K. 2023, arXiv e-prints, arXiv:2311.07769, doi: [10.48550/arXiv.2311.07769](https://doi.org/10.48550/arXiv.2311.07769)
- Banerjee, A., Barstow, J. K., Gressier, A., et al. 2024, ApJL, 975, L11, doi: [10.3847/2041-8213/ad73d0](https://doi.org/10.3847/2041-8213/ad73d0)
- Barber, R. J., Strange, J. K., Hill, C., et al. 2014, MNRAS, 437, 1828, doi: [10.1093/mnras/stt2011](https://doi.org/10.1093/mnras/stt2011)
- Barclay, T., Kostov, V. B., Colón, K. D., et al. 2021, AJ, 162, 300, doi: [10.3847/1538-3881/ac2824](https://doi.org/10.3847/1538-3881/ac2824)
- Barnes, I., Hjorth, J., & Mihalopoulos, N. 2006, Chem. Rev., 106, 940, doi: [10.1021/cr020529+](https://doi.org/10.1021/cr020529+)
- Batalha, N., Rooney, C., Mukherjee, S., et al. 2024, Picaso: Release 3.3, v3.3, Zenodo, doi: [10.5281/zenodo.14160128](https://doi.org/10.5281/zenodo.14160128)
- Batalha, N. E., Lewis, T., Fortney, J. J., et al. 2019a, ApJL, 885, L25, doi: [10.3847/2041-8213/ab4909](https://doi.org/10.3847/2041-8213/ab4909)
- Batalha, N. E., Marley, M. S., Lewis, N. K., & Fortney, J. J. 2019b, ApJ, 878, 70, doi: [10.3847/1538-4357/ab1b51](https://doi.org/10.3847/1538-4357/ab1b51)
- Beatty, T. G., Welbanks, L., Schlawin, E., et al. 2024, ApJL, 970, L10, doi: [10.3847/2041-8213/ad55e9](https://doi.org/10.3847/2041-8213/ad55e9)
- Béky, B., Kipping, D. M., & Holman, M. J. 2014, MNRAS, 442, 3686, doi: [10.1093/mnras/stu1061](https://doi.org/10.1093/mnras/stu1061)
- Bell, T., Ahrer, E.-M., Brande, J., et al. 2022, The Journal of Open Source Software, 7, 4503, doi: [10.21105/joss.04503](https://doi.org/10.21105/joss.04503)
- Benneke, B., & Seager, S. 2013, ApJ, 778, 153, doi: [10.1088/0004-637X/778/2/153](https://doi.org/10.1088/0004-637X/778/2/153)
- Benneke, B., Werner, M., Petigura, E., et al. 2017, ApJ, 834, 187, doi: [10.3847/1538-4357/834/2/187](https://doi.org/10.3847/1538-4357/834/2/187)
- Benneke, B., Wong, I., Piaulet, C., et al. 2019, ApJL, 887, L14, doi: [10.3847/2041-8213/ab59dc](https://doi.org/10.3847/2041-8213/ab59dc)
- Benneke, B., Roy, P.-A., Coulombe, L.-P., et al. 2024, arXiv e-prints, arXiv:2403.03325, doi: [10.48550/arXiv.2403.03325](https://doi.org/10.48550/arXiv.2403.03325)
- Bergin, E. A., Kempton, E. M. R., Hirschmann, M., et al. 2023, ApJL, 949, L17, doi: [10.3847/2041-8213/acd377](https://doi.org/10.3847/2041-8213/acd377)
- Birkmann, S. M., Ferruit, P., Alves de Oliveira, C., et al. 2014, in Society of Photo-Optical Instrumentation Engineers (SPIE) Conference Series, Vol. 9143, Space Telescopes and Instrumentation 2014: Optical, Infrared, and Millimeter Wave, ed. J. Oschmann, Jacobus M., M. Clampin, G. G. Fazio, & H. A. MacEwen, 914308, doi: [10.1117/12.2054642](https://doi.org/10.1117/12.2054642)
- Blain, D., Charnay, B., & Bézard, B. 2021, A&A, 646, A15, doi: [10.1051/0004-6361/202039072](https://doi.org/10.1051/0004-6361/202039072)
- Buchner, J., Georgakakis, A., Nandra, K., et al. 2014, A&A, 564, A125, doi: [10.1051/0004-6361/201322971](https://doi.org/10.1051/0004-6361/201322971)

- Cadieux, C., Doyon, R., MacDonald, R. J., et al. 2024, *ApJL*, 970, L2, doi: [10.3847/2041-8213/ad5afa](https://doi.org/10.3847/2041-8213/ad5afa)
- Chabrier, G., & Debras, F. 2021, *ApJ*, 917, 4, doi: [10.3847/1538-4357/abfc48](https://doi.org/10.3847/1538-4357/abfc48)
- Charlson, R. J., Warren, S. G., Lovelock, J. E., & Andreae, M. O. 1987, *Nature*, 326, 655, doi: [10.1038/326655a0](https://doi.org/10.1038/326655a0)
- Cloutier, R., Astudillo-Defru, N., Doyon, R., et al. 2017, *A&A*, 608, A35, doi: [10.1051/0004-6361/201731558](https://doi.org/10.1051/0004-6361/201731558)
- . 2019, *A&A*, 621, A49, doi: [10.1051/0004-6361/201833995](https://doi.org/10.1051/0004-6361/201833995)
- Coles, P. A., Yurchenko, S. N., & Tennyson, J. 2019, *MNRAS*, 490, 4638, doi: [10.1093/mnras/stz2778](https://doi.org/10.1093/mnras/stz2778)
- Cooke, G. J., & Madhusudhan, N. 2024, *ApJ*, 977, 209, doi: [10.3847/1538-4357/ad8cda](https://doi.org/10.3847/1538-4357/ad8cda)
- Coulombe, L.-P., Benneke, B., Challener, R., et al. 2023, *Nature*, 620, 292, doi: [10.1038/s41586-023-06230-1](https://doi.org/10.1038/s41586-023-06230-1)
- Damiano, M., Bello-Arufe, A., Yang, J., & Hu, R. 2024, *ApJL*, 968, L22, doi: [10.3847/2041-8213/ad5204](https://doi.org/10.3847/2041-8213/ad5204)
- Darveau-Bernier, A., Albert, L., Talens, G. J., et al. 2022, *PASP*, 134, 094502, doi: [10.1088/1538-3873/ac8a77](https://doi.org/10.1088/1538-3873/ac8a77)
- de Wit, J., & Seager, S. 2013, *Science*, 342, 1473, doi: [10.1126/science.1245450](https://doi.org/10.1126/science.1245450)
- Doyon, R., Hutchings, J. B., Beaulieu, M., et al. 2012, in *Society of Photo-Optical Instrumentation Engineers (SPIE) Conference Series*, Vol. 8442, *Space Telescopes and Instrumentation 2012: Optical, Infrared, and Millimeter Wave*, ed. M. C. Clampin, G. G. Fazio, H. A. MacEwen, & J. Oschmann, Jacobus M., 84422R, doi: [10.1117/12.926578](https://doi.org/10.1117/12.926578)
- Doyon, R., Willott, C. J., Hutchings, J. B., et al. 2023, *PASP*, 135, 098001, doi: [10.1088/1538-3873/acd41b](https://doi.org/10.1088/1538-3873/acd41b)
- Dyrek, A., Min, M., Decin, L., et al. 2024, *Nature*, 625, 51, doi: [10.1038/s41586-023-06849-0](https://doi.org/10.1038/s41586-023-06849-0)
- Feinstein, A. D., Radica, M., Welbanks, L., et al. 2023, *Nature*, 614, 670, doi: [10.1038/s41586-022-05674-1](https://doi.org/10.1038/s41586-022-05674-1)
- Feroz, F., Hobson, M. P., & Bridges, M. 2009, *MNRAS*, 398, 1601, doi: [10.1111/j.1365-2966.2009.14548.x](https://doi.org/10.1111/j.1365-2966.2009.14548.x)
- Ferruit, P., Bagnasco, G., Barho, R., et al. 2012, in *Society of Photo-Optical Instrumentation Engineers (SPIE) Conference Series*, Vol. 8442, *Space Telescopes and Instrumentation 2012: Optical, Infrared, and Millimeter Wave*, ed. M. C. Clampin, G. G. Fazio, H. A. MacEwen, & J. Oschmann, Jacobus M., 84422O, doi: [10.1117/12.925810](https://doi.org/10.1117/12.925810)
- Fisher, C., Taylor, J., Parmentier, V., et al. 2024, *MNRAS*, 535, 27, doi: [10.1093/mnras/stae2240](https://doi.org/10.1093/mnras/stae2240)
- Foreman-Mackey, D., Hogg, D. W., Lang, D., & Goodman, J. 2013, *PASP*, 125, 306, doi: [10.1086/670067](https://doi.org/10.1086/670067)
- Fortney, J. J., Marley, M. S., & Barnes, J. W. 2007, *ApJ*, 659, 1661, doi: [10.1086/512120](https://doi.org/10.1086/512120)
- Fournier-Tondreau, M., MacDonald, R. J., Radica, M., et al. 2024a, *MNRAS*, 528, 3354, doi: [10.1093/mnras/stad3813](https://doi.org/10.1093/mnras/stad3813)
- Fournier-Tondreau, M., Pan, Y., Morel, K., et al. 2024b, *arXiv e-prints*, arXiv:2412.17072, doi: [10.48550/arXiv.2412.17072](https://doi.org/10.48550/arXiv.2412.17072)
- Fu, G., Stevenson, K. B., Sing, D. K., et al. 2025, *arXiv e-prints*, arXiv:2501.02081, <https://arxiv.org/abs/2501.02081>
- Glein, C. R. 2024, *ApJL*, 964, L19, doi: [10.3847/2041-8213/ad3079](https://doi.org/10.3847/2041-8213/ad3079)
- Gordon, I. E., Rothman, L. S., Hargreaves, R. J., et al. 2022, *JQSRT*, 277, 107949, doi: [10.1016/j.jqsrt.2021.107949](https://doi.org/10.1016/j.jqsrt.2021.107949)
- Grant, D., & Wakeford, H. 2024, *The Journal of Open Source Software*, 9, 6816, doi: [10.21105/joss.06816](https://doi.org/10.21105/joss.06816)
- Grant, D., Lewis, N. K., Wakeford, H. R., et al. 2023, *ApJL*, 956, L32, doi: [10.3847/2041-8213/acfc3b10.3847/2041-8213/acfdab](https://doi.org/10.3847/2041-8213/acfc3b10.3847/2041-8213/acfdab)
- Gressier, A., MacDonald, R. J., Espinoza, N., et al. 2024, *arXiv e-prints*, arXiv:2410.08149, doi: [10.48550/arXiv.2410.08149](https://doi.org/10.48550/arXiv.2410.08149)
- Hänni, N., Altwegg, K., Combi, M., et al. 2024, *ApJ*, 976, 74, doi: [10.3847/1538-4357/ad8565](https://doi.org/10.3847/1538-4357/ad8565)
- Hargreaves, R. J., Gordon, I. E., Rey, M., et al. 2020, *ApJS*, 247, 55, doi: [10.3847/1538-4365/ab7a1a](https://doi.org/10.3847/1538-4365/ab7a1a)
- Hargreaves, R. J., Gordon, I. E., Rothman, L. S., et al. 2019, *JQSRT*, 232, 35, doi: [10.1016/j.jqsrt.2019.04.040](https://doi.org/10.1016/j.jqsrt.2019.04.040)
- Harris, C. R., Millman, K. J., van der Walt, S. J., et al. 2020, *Nature*, 585, 357, doi: [10.1038/s41586-020-2649-2](https://doi.org/10.1038/s41586-020-2649-2)
- Harris, G. J., Tennyson, J., Kaminsky, B. M., Pavlenko, Y. V., & Jones, H. R. A. 2006, *MNRAS*, 367, 400, doi: [10.1111/j.1365-2966.2005.09960.x](https://doi.org/10.1111/j.1365-2966.2005.09960.x)
- Holmberg, M., & Madhusudhan, N. 2023, *MNRAS*, 524, 377, doi: [10.1093/mnras/stad1580](https://doi.org/10.1093/mnras/stad1580)
- . 2024, *A&A*, 683, L2, doi: [10.1051/0004-6361/202348238](https://doi.org/10.1051/0004-6361/202348238)
- Horne, K. 1986, *PASP*, 98, 609, doi: [10.1086/131801](https://doi.org/10.1086/131801)
- Hu, R., Damiano, M., Scheucher, M., et al. 2021, *ApJL*, 921, L8, doi: [10.3847/2041-8213/ac1f92](https://doi.org/10.3847/2041-8213/ac1f92)
- Huang, X., Freedman, R. S., Tashkun, S. A., Schwenke, D. W., & Lee, T. J. 2013, *JQSRT*, 130, 134, doi: [10.1016/j.jqsrt.2013.05.018](https://doi.org/10.1016/j.jqsrt.2013.05.018)
- Huang, X., Schwenke, D. W., Freedman, R. S., & Lee, T. J. 2017, *JQSRT*, 203, 224, doi: [10.1016/j.jqsrt.2017.04.026](https://doi.org/10.1016/j.jqsrt.2017.04.026)
- Hunter, J. D. 2007, *Computing in science & engineering*, 9, 90
- Husser, T. O., Wende-von Berg, S., Dreizler, S., et al. 2013, *A&A*, 553, A6, doi: [10.1051/0004-6361/201219058](https://doi.org/10.1051/0004-6361/201219058)
- Inglis, J., Batalha, N. E., Lewis, N. K., et al. 2024, *ApJL*, 973, L41, doi: [10.3847/2041-8213/ad725e](https://doi.org/10.3847/2041-8213/ad725e)

- Innes, H., Tsai, S.-M., & Pierrehumbert, R. T. 2023, *ApJ*, 953, 168, doi: [10.3847/1538-4357/ace346](https://doi.org/10.3847/1538-4357/ace346)
- Jones, E., Oliphant, T., Peterson, P., et al. 2024, *SciPy*: Open source scientific tools for Python. <http://www.scipy.org/>
- Karkoschka, E., & Tomasko, M. G. 2011, *Icarus*, 211, 780, doi: [10.1016/j.icarus.2010.08.013](https://doi.org/10.1016/j.icarus.2010.08.013)
- Karman, T., Gordon, I. E., van der Avoird, A., et al. 2019, *Icarus*, 328, 160, doi: [10.1016/j.icarus.2019.02.034](https://doi.org/10.1016/j.icarus.2019.02.034)
- Kipping, D. M. 2013, *MNRAS*, 435, 2152, doi: [10.1093/mnras/stt1435](https://doi.org/10.1093/mnras/stt1435)
- Kite, E. S., & Ford, E. B. 2018, *ApJ*, 864, 75, doi: [10.3847/1538-4357/aad6e0](https://doi.org/10.3847/1538-4357/aad6e0)
- Kitzmann, D., Heng, K., Oreshenko, M., et al. 2020, *ApJ*, 890, 174, doi: [10.3847/1538-4357/ab6d71](https://doi.org/10.3847/1538-4357/ab6d71)
- Kitzmann, D., Stock, J. W., & Patzer, A. B. C. 2024, *MNRAS*, 527, 7263, doi: [10.1093/mnras/stad3515](https://doi.org/10.1093/mnras/stad3515)
- Kostogryz, N., Shapiro, A. I., Witzke, V., et al. 2023, *Research Notes of the American Astronomical Society*, 7, 39, doi: [10.3847/2515-5172/acc180](https://doi.org/10.3847/2515-5172/acc180)
- Kreidberg, L. 2015, *PASP*, 127, 1161, doi: [10.1086/683602](https://doi.org/10.1086/683602)
- Leconte, J., Spiga, A., Clément, N., et al. 2024, *A&A*, 686, A131, doi: [10.1051/0004-6361/202348928](https://doi.org/10.1051/0004-6361/202348928)
- Li, G., Gordon, I. E., Rothman, L. S., et al. 2015, *The Astrophysical Journal Supplement Series*, 216, 15, doi: [10.1088/0067-0049/216/1/15](https://doi.org/10.1088/0067-0049/216/1/15)
- Li, J., Bergin, E. A., Blake, G. A., Ciesla, F. J., & Hirschmann, M. M. 2021, *Science Advances*, 7, eabd3632, doi: [10.1126/sciadv.abd3632](https://doi.org/10.1126/sciadv.abd3632)
- Lim, O., Benneke, B., Doyon, R., et al. 2023, *ApJL*, 955, L22, doi: [10.3847/2041-8213/acf7c4](https://doi.org/10.3847/2041-8213/acf7c4)
- Lustig-Yaeger, J., Fu, G., May, E. M., et al. 2023, *Nature Astronomy*, 7, 1317, doi: [10.1038/s41550-023-02064-z](https://doi.org/10.1038/s41550-023-02064-z)
- Luu, C. N., Yu, X., Glein, C. R., et al. 2024, *ApJL*, 977, L51, doi: [10.3847/2041-8213/ad9eb1](https://doi.org/10.3847/2041-8213/ad9eb1)
- Lyon, S. P., & Johnson, J. D. 1992, *SESAME: The Los Alamos National Laboratory Equation of State Database*, Tech. Rep. LA-UR-92-3407, Los Alamos National Laboratory
- MacDonald, R. J. 2023, *The Journal of Open Source Software*, 8, 4873, doi: [10.21105/joss.04873](https://doi.org/10.21105/joss.04873)
- MacDonald, R. J., & Lewis, N. K. 2022, *ApJ*, 929, 20, doi: [10.3847/1538-4357/ac47fe](https://doi.org/10.3847/1538-4357/ac47fe)
- MacDonald, R. J., & Madhusudhan, N. 2017, *MNRAS*, 469, 1979, doi: [10.1093/mnras/stx804](https://doi.org/10.1093/mnras/stx804)
- Madhusudhan, N. 2012, *ApJ*, 758, 36, doi: [10.1088/0004-637X/758/1/36](https://doi.org/10.1088/0004-637X/758/1/36)
- Madhusudhan, N., Nixon, M. C., Welbanks, L., Piette, A. A., & Booth, R. A. 2020, *ApJL*, 891, L7, doi: [10.3847/2041-8213/ab7229](https://doi.org/10.3847/2041-8213/ab7229)
- Madhusudhan, N., Piette, A. A., & Constantinou, S. 2021, *ApJ*, 918, 1, doi: [10.3847/1538-4357/abfd9c](https://doi.org/10.3847/1538-4357/abfd9c)
- Madhusudhan, N., Sarkar, S., Constantinou, S., et al. 2023, *ApJL*, 956, L13, doi: [10.3847/2041-8213/acf577](https://doi.org/10.3847/2041-8213/acf577)
- Madhusudhan, N., & Seager, S. 2009, *ApJ*, 707, 24, doi: [10.1088/0004-637X/707/1/24](https://doi.org/10.1088/0004-637X/707/1/24)
- Magic, Z., Chiavassa, A., Collet, R., & Asplund, M. 2015, *A&A*, 573, A90, doi: [10.1051/0004-6361/201423804](https://doi.org/10.1051/0004-6361/201423804)
- Malik, M., Kitzmann, D., Mendonça, J. M., et al. 2019, *AJ*, 157, 170, doi: [10.3847/1538-3881/ab1084](https://doi.org/10.3847/1538-3881/ab1084)
- Malik, M., Grosheintz, L., Mendonça, J. M., et al. 2017, *AJ*, 153, 56, doi: [10.3847/1538-3881/153/2/56](https://doi.org/10.3847/1538-3881/153/2/56)
- May, E. M., MacDonald, R. J., Bennett, K. A., et al. 2023, *ApJL*, 959, L9, doi: [10.3847/2041-8213/ad054f](https://doi.org/10.3847/2041-8213/ad054f)
- Mazevet, S., Licari, A., Chabrier, G., & Potekhin, A. Y. 2019, *A&A*, 621, A128, doi: [10.1051/0004-6361/201833963](https://doi.org/10.1051/0004-6361/201833963)
- Mollière, P., van Boekel, R., Dullemond, C., Henning, T., & Mordasini, C. 2015, *ApJ*, 813, 47, doi: [10.1088/0004-637X/813/1/47](https://doi.org/10.1088/0004-637X/813/1/47)
- Montet, B. T., Morton, T. D., Foreman-Mackey, D., et al. 2015, *ApJ*, 809, 25, doi: [10.1088/0004-637X/809/1/25](https://doi.org/10.1088/0004-637X/809/1/25)
- Moran, S. E., Stevenson, K. B., Sing, D. K., et al. 2023, *ApJL*, 948, L11, doi: [10.3847/2041-8213/acbc9c](https://doi.org/10.3847/2041-8213/acbc9c)
- Mukherjee, S., Batalha, N. E., Fortney, J. J., & Marley, M. S. 2023, *ApJ*, 942, 71, doi: [10.3847/1538-4357/ac9f48](https://doi.org/10.3847/1538-4357/ac9f48)
- Mukherjee, S., Fortney, J. J., Wogan, N. F., Sing, D. K., & Ohno, K. 2024, *arXiv e-prints*, arXiv:2410.17169, doi: [10.48550/arXiv.2410.17169](https://doi.org/10.48550/arXiv.2410.17169)
- Mullens, E., Lewis, N. K., & MacDonald, R. J. 2024, *ApJ*, 977, 105, doi: [10.3847/1538-4357/ad8575](https://doi.org/10.3847/1538-4357/ad8575)
- Newville, M., Otten, R., Nelson, A., et al. 2024, *lmfit/lmfit-py*: 1.3.2, 1.3.2, Zenodo, doi: [10.5281/zenodo.598352](https://doi.org/10.5281/zenodo.598352)
- Nixon, M. C., & Madhusudhan, N. 2021, *MNRAS*, 505, 3414, doi: [10.1093/mnras/stab1500](https://doi.org/10.1093/mnras/stab1500)
- Owens, A., Yachmenev, A., Thiel, W., et al. 2018, *MNRAS*, 479, 3002, doi: [10.1093/mnras/sty1542](https://doi.org/10.1093/mnras/sty1542)
- Owens, A., Yurchenko, S. N., & Tennyson, J. 2024, *MNRAS*, 530, 4004, doi: [10.1093/mnras/stae1110](https://doi.org/10.1093/mnras/stae1110)
- Perez, F., & Granger, B. E. 2007, *Computing in Science and Engineering*, 9, 21, doi: [10.1109/MCSE.2007.53](https://doi.org/10.1109/MCSE.2007.53)
- Piaulet-Ghorayeb, C., Benneke, B., Radica, M., et al. 2024, *ApJL*, 974, L10, doi: [10.3847/2041-8213/ad6f00](https://doi.org/10.3847/2041-8213/ad6f00)
- Pierrehumbert, R. T. 2023, *ApJ*, 944, 20, doi: [10.3847/1538-4357/acafdf](https://doi.org/10.3847/1538-4357/acafdf)
- Piette, A. A., & Madhusudhan, N. 2020, *ApJ*, 904, 154, doi: [10.3847/1538-4357/abfbf1](https://doi.org/10.3847/1538-4357/abfbf1)
- Polyansky, O. L., Kyuberis, A. A., Zobov, N. F., et al. 2018, *MNRAS*, 480, 2597, doi: [10.1093/mnras/sty1877](https://doi.org/10.1093/mnras/sty1877)



- Powell, D., Feinstein, A. D., Lee, E. K. H., et al. 2024, *Nature*, 626, 979, doi: [10.1038/s41586-024-07040-9](https://doi.org/10.1038/s41586-024-07040-9)
- Rackham, B. V., Apai, D., & Giampapa, M. S. 2018, *ApJ*, 853, 122, doi: [10.3847/1538-4357/aaa08c](https://doi.org/10.3847/1538-4357/aaa08c)
- Radica, M. 2024, *Journal of Open Source Software*, 9, 6898, doi: [10.21105/joss.06898](https://doi.org/10.21105/joss.06898)
- Radica, M. 2024, *radicamc/exoUPRF: v1.0.1, v1.0.1*, Zenodo, doi: [10.5281/zenodo.12628066](https://doi.org/10.5281/zenodo.12628066)
- Radica, M., Artigau, É., Lafrenière, D., et al. 2022a, *MNRAS*, 517, 5050, doi: [10.1093/mnras/stac3024](https://doi.org/10.1093/mnras/stac3024)
- Radica, M., Albert, L., Taylor, J., et al. 2022b, *PASP*, 134, 104502, doi: [10.1088/1538-3873/ac9430](https://doi.org/10.1088/1538-3873/ac9430)
- Radica, M., Welbanks, L., Espinoza, N., et al. 2023, *MNRAS*, 524, 835, doi: [10.1093/mnras/stad1762](https://doi.org/10.1093/mnras/stad1762)
- Radica, M., Piaulet-Ghorayeb, C., Taylor, J., et al. 2024a, *arXiv e-prints*, arXiv:2409.19333, doi: [10.48550/arXiv.2409.19333](https://doi.org/10.48550/arXiv.2409.19333)
- Radica, M., Coulombe, L.-P., Taylor, J., et al. 2024b, *ApJL*, 962, L20, doi: [10.3847/2041-8213/ad20e4](https://doi.org/10.3847/2041-8213/ad20e4)
- Rathcke, A. D., MacDonald, R. J., Barstow, J. K., et al. 2021, *AJ*, 162, 138, doi: [10.3847/1538-3881/ac0e99](https://doi.org/10.3847/1538-3881/ac0e99)
- Rigby, F. E., Pica-Ciamarra, L., Holmberg, M., et al. 2024, *ApJ*, 975, 101, doi: [10.3847/1538-4357/ad6c38](https://doi.org/10.3847/1538-4357/ad6c38)
- Rustamkulov, Z., Sing, D. K., Liu, R., & Wang, A. 2022, *ApJL*, 928, L7, doi: [10.3847/2041-8213/ac5b6f](https://doi.org/10.3847/2041-8213/ac5b6f)
- Rustamkulov, Z., Sing, D. K., Mukherjee, S., et al. 2023, *Nature*, 614, 659, doi: [10.1038/s41586-022-05677-y](https://doi.org/10.1038/s41586-022-05677-y)
- Sarkis, P., Henning, T., Kürster, M., et al. 2018, *AJ*, 155, 257, doi: [10.3847/1538-3881/aac108](https://doi.org/10.3847/1538-3881/aac108)
- Scheucher, M., Wunderlich, F., Grenfell, J. L., et al. 2020, *ApJ*, 898, 44, doi: [10.3847/1538-4357/ab9084](https://doi.org/10.3847/1538-4357/ab9084)
- Schlawin, E., Ohno, K., Bell, T. J., et al. 2024, *ApJL*, 974, L33, doi: [10.3847/2041-8213/ad7fef](https://doi.org/10.3847/2041-8213/ad7fef)
- Schwieterman, E. W., Kiang, N. Y., Parenteau, M. N., et al. 2018, *Astrobiology*, 18, 663, doi: [10.1089/ast.2017.1729](https://doi.org/10.1089/ast.2017.1729)
- Seager, S., Bains, W., & Hu, R. 2013, *ApJ*, 775, 104, doi: [10.1088/0004-637X/775/2/104](https://doi.org/10.1088/0004-637X/775/2/104)
- Segura, A., Kasting, J. F., Meadows, V., et al. 2005, *Astrobiology*, 5, 706, doi: [10.1089/ast.2005.5.706](https://doi.org/10.1089/ast.2005.5.706)
- Sharpe, S. W., Johnson, T. J., Sams, R. L., et al. 2004, *Applied Spectroscopy*, 58, 1452, doi: [10.1366/0003702042641281](https://doi.org/10.1366/0003702042641281)
- Shorttle, O., Jordan, S., Nicholls, H., Lichtenberg, T., & Bower, D. J. 2024, *ApJL*, 962, L8, doi: [10.3847/2041-8213/ad206e](https://doi.org/10.3847/2041-8213/ad206e)
- Sing, D. K., Rustamkulov, Z., Thorngren, D. P., et al. 2024, *Nature*, 630, 831, doi: [10.1038/s41586-024-07395-z](https://doi.org/10.1038/s41586-024-07395-z)
- Speagle, J. S. 2020, *MNRAS*, 493, 3132, doi: [10.1093/mnras/staa278](https://doi.org/10.1093/mnras/staa278)
- Stock, J. W., Kitzmann, D., & Patzer, A. B. C. 2022, *MNRAS*, 517, 4070, doi: [10.1093/mnras/stac2623](https://doi.org/10.1093/mnras/stac2623)
- Tabernerero, H. M., Shan, Y., Caballero, J. A., et al. 2024, *A&A*, 689, A223, doi: [10.1051/0004-6361/202450054](https://doi.org/10.1051/0004-6361/202450054)
- Taylor, J., Radica, M., Welbanks, L., et al. 2023, *MNRAS*, 524, 817, doi: [10.1093/mnras/stad1547](https://doi.org/10.1093/mnras/stad1547)
- Thompson, S. L. 1990, *ANEOS Analytic Equations of State for Shock Physics Codes Input Manual*, Tech. Rep. SAND-89-2951, 6939284, Sandia National Laboratory, doi: [10.2172/6939284](https://doi.org/10.2172/6939284)
- Townsend, R., & Lopez, A. 2023, *The Journal of Open Source Software*, 8, 4602, doi: [10.21105/joss.04602](https://doi.org/10.21105/joss.04602)
- Trotta, R. 2008, *Contemporary Physics*, 49, 71, doi: [10.1080/00107510802066753](https://doi.org/10.1080/00107510802066753)
- Tsai, S.-M., Innes, H., Lichtenberg, T., et al. 2021a, *ApJL*, 922, L27, doi: [10.3847/2041-8213/ac399a](https://doi.org/10.3847/2041-8213/ac399a)
- Tsai, S.-M., Innes, H., Wogan, N. F., & Schwieterman, E. W. 2024, *ApJL*, 966, L24, doi: [10.3847/2041-8213/ad3801](https://doi.org/10.3847/2041-8213/ad3801)
- Tsai, S.-M., Lyons, J. R., Grosheintz, L., et al. 2017, *ApJS*, 228, 20, doi: [10.3847/1538-4365/228/2/20](https://doi.org/10.3847/1538-4365/228/2/20)
- Tsai, S.-M., Malik, M., Kitzmann, D., et al. 2021b, *ApJ*, 923, 264, doi: [10.3847/1538-4357/ac29bc](https://doi.org/10.3847/1538-4357/ac29bc)
- Tsai, S.-M., Lee, E. K. H., Powell, D., et al. 2023, *Nature*, 617, 483, doi: [10.1038/s41586-023-05902-2](https://doi.org/10.1038/s41586-023-05902-2)
- Tsiaras, A., Waldmann, I. P., Tinetti, G., Tennyson, J., & Yurchenko, S. N. 2019, *Nature Astronomy*, 3, 1086, doi: [10.1038/s41550-019-0878-9](https://doi.org/10.1038/s41550-019-0878-9)
- van Dokkum, P. G. 2001, *PASP*, 113, 1420, doi: [10.1086/323894](https://doi.org/10.1086/323894)
- Vardya, M. S. 1962, *ApJ*, 135, 303, doi: [10.1086/147269](https://doi.org/10.1086/147269)
- Virtanen, P., Gommers, R., Oliphant, T. E., et al. 2020, *Nature Methods*, 17, 261, doi: [10.1038/s41592-019-0686-2](https://doi.org/10.1038/s41592-019-0686-2)
- Waldmann, I. P., Tinetti, G., Rocchetto, M., et al. 2015, *ApJ*, 802, 107, doi: [10.1088/0004-637X/802/2/107](https://doi.org/10.1088/0004-637X/802/2/107)
- Wallack, N. L., Batalha, N. E., Alderson, L., et al. 2024, *AJ*, 168, 77, doi: [10.3847/1538-3881/ad3917](https://doi.org/10.3847/1538-3881/ad3917)
- Welbanks, L., & Madhusudhan, N. 2021, *ApJ*, 913, 114, doi: [10.3847/1538-4357/abee94](https://doi.org/10.3847/1538-4357/abee94)
- Welbanks, L., Bell, T. J., Beatty, T. G., et al. 2024, *Nature*, 630, 836, doi: [10.1038/s41586-024-07514-w](https://doi.org/10.1038/s41586-024-07514-w)
- Wilzewski, J. S., Gordon, I. E., Kochanov, R. V., Hill, C., & Rothman, L. S. 2016, *Journal of Quantitative Spectroscopy and Radiative Transfer*, 168, 193, doi: [10.1016/j.jqsrt.2015.09.003](https://doi.org/10.1016/j.jqsrt.2015.09.003)
- Wogan, N. 2024, *Photochem v0.6.2, v0.6.2*, Zenodo, doi: [10.5281/zenodo.14032108](https://doi.org/10.5281/zenodo.14032108)
- Wogan, N. F., Batalha, N. E., Zahnle, K. J., et al. 2024, *ApJL*, 963, L7, doi: [10.3847/2041-8213/ad2616](https://doi.org/10.3847/2041-8213/ad2616)

- Yang, J., & Hu, R. 2024, ApJL, 971, L48,  
doi: [10.3847/2041-8213/ad6b25](https://doi.org/10.3847/2041-8213/ad6b25)
- Yip, K. H., Changeat, Q., Edwards, B., et al. 2021, AJ,  
161, 4, doi: [10.3847/1538-3881/abc179](https://doi.org/10.3847/1538-3881/abc179)
- Yu, X., Moses, J. I., Fortney, J. J., & Zhang, X. 2021, ApJ,  
914, 38, doi: [10.3847/1538-4357/abfdc7](https://doi.org/10.3847/1538-4357/abfdc7)
- Yurchenko, S. N., Mellor, T. M., Freedman, R. S., &  
Tennyson, J. 2020, MNRAS, 496, 5282,  
doi: [10.1093/mnras/staa1874](https://doi.org/10.1093/mnras/staa1874)
- Yurchenko, S. N., Owens, A., Kefala, K., & Tennyson, J.  
2024, MNRAS, 528, 3719, doi: [10.1093/mnras/stae148](https://doi.org/10.1093/mnras/stae148)
- Yurchenko, S. N., & Tennyson, J. 2014, MNRAS, 440, 1649,  
doi: [10.1093/mnras/stu326](https://doi.org/10.1093/mnras/stu326)

## APPENDIX

## A. REPRODUCTION OF THE RETRIEVAL RESULTS FROM MADHUSUDHAN ET AL. (2023)

Here we show that our atmospheric retrieval framework can reproduce consistent results to those presented in Madhusudhan et al. (2023), if we use the same full-resolution data presented in that study. This demonstrates that the non-detections of CO<sub>2</sub> and DMS presented above are primarily driven by differences in the data reduction and/or light curve fitting approaches from our respective studies, rather than differences in the atmospheric modelling and/or retrieval approaches.

We used POSEIDON to replicate the results of Madhusudhan et al. (2023). For this purpose, we used the exact same atmospheric model configuration as the ‘canonical’ model described in Madhusudhan et al. (2023). To summarise, this retrieval model fits for the log<sub>10</sub> volume mixing ratios of H<sub>2</sub>O, CH<sub>4</sub>, NH<sub>3</sub>, HCN, CO, CO<sub>2</sub>, DMS, CS<sub>2</sub>, CH<sub>3</sub>Cl, OCS, and N<sub>2</sub>O, the 6-parameter P-T profile from Madhusudhan & Seager (2009), the 4-parameter inhomogeneous cloud and haze parameterisation from MacDonald & Madhusudhan (2017), and the reference pressure corresponding to 2.61  $R_{\oplus}$ . We consider three retrieval models: (i) no offset between the NIRISS and NIRSpec G395H data; (ii) one offset between NIRISS and NIRSpec G395H; and (iii) two offsets, one offset between NIRISS and the NIRSpec G395H NRS1 detector and one offset between NIRISS and the NIRSpec G395H NRS2 detector. Therefore, the three models have 22, 23, and 24 free parameters, respectively. We use identical priors for these parameters as in Table 4 from Madhusudhan et al. (2023). For fixed system properties (e.g. planetary mass, stellar radius), we used the values from Benneke et al. (2019) for consistency with Madhusudhan et al. (2023).

Several important retrieval model settings were not mentioned by Madhusudhan et al. (2023). Therefore, we adopted conservative choices to ensure the reliability of our retrieval results. Our opacities are sampled on a model wavelength grid with a resolution of  $R = \lambda/\Delta\lambda = 100,000$ , ensuring negligible errors from opacity sampling. We used 100 atmospheric layers from 10<sup>-6</sup>–10 bar, spaced uniformly in log-pressure. We note that the minimum atmospheric pressure used here differs from the value of 10<sup>-8</sup> bar we adopt for our main retrieval results, but we chose 10<sup>-6</sup> bar here to match the value implied in Table 4 of Madhusudhan et al. (2023). The line lists in POSEIDON (described in the main text and Table 3) do differ from Madhusudhan et al. (2023) for several important molecules (in particular CH<sub>4</sub> and CO<sub>2</sub>), but we stress that POSEIDON v1.2 is a state-of-the-art opacity database with the latest ExoMol line lists (as of 2024). Finally, we used 1,000 MultiNest live points to ensure fine sampling of the parameter space.

Table 6 summarises the retrieval model statistics from our analysis using the data from Madhusudhan et al. (2023). We find that only CH<sub>4</sub> is robustly detected, with a detection significance  $> 4.5\sigma$  across the different offset treatments. None of our retrievals provide notable evidence for CO<sub>2</sub> or DMS, with peak Bayes factors of  $\approx 6$  and  $\approx 3$ , respectively (compared to  $\mathcal{B}_{\text{Ref},i} > 12$  for ‘moderate evidence’ and  $\mathcal{B}_{\text{Ref},i} > 150$  for ‘strong evidence’ on the Jeffreys’ scale, see Trotta 2008). Our retrievals favour a single offset between the NIRISS SOSS and NIRSpec G395H data (44<sup>+13</sup><sub>-12</sub> ppm), consistent with Madhusudhan et al. (2023). The statistically preferred ‘one offset’ model has a Bayes factor of  $\approx 5$  for CO<sub>2</sub> (2.4 $\sigma$ ), corresponding to ‘weak evidence’ at best, while there is no evidence for DMS (Bayes factor  $\approx 1$ ).

Figure 14 provides a reproduction of Madhusudhan et al. (2023)’s Figure 4. We find broadly consistent posterior distributions to Madhusudhan et al. (2023) when using their data. Our CH<sub>4</sub> abundances are higher by  $\approx 0.8$  dex, but consistent within 1 $\sigma$ . We note that our CO<sub>2</sub> posterior for the ‘no offset’ case has a more prominent tail to low abundances than Figure 4 in Madhusudhan et al. (2023). This difference arises because Madhusudhan et al. (2023) renormalised the probability densities for each retrieval in their Figure 4 to have the same peak probability density, while our Figure 14 preserves the relative probability density differences between the retrievals. We highlight that our visualisation method has the advantage of ensuring the same integrated area for each distribution (i.e. total probability), which Madhusudhan et al. (2023)’s Figure 4 does not respect. We stress this point because it artificially suppresses the CO<sub>2</sub> tail for the ‘no offset’ case in Madhusudhan et al. (2023)’s Figure 4, which consequently oversells the confidence of their claimed CO<sub>2</sub> detection.

Finally, Figure 15 shows correlations between notable atmospheric properties from these retrievals on the Madhusudhan et al. (2023) data. We highlight a strong correlation between the CO<sub>2</sub> abundance and the temperature at the top of the atmosphere ( $T_{\text{ref}}$ ), with most of the parameter space that favours a high CO<sub>2</sub> abundance corresponding to temperatures far in excess of the planetary equilibrium temperature ( $\approx 250$  K). Thus, even if one assumes CO<sub>2</sub> is present in K2-18 b’s atmosphere, the planet would be far too warm to support habitable liquid water surface conditions.

**Table 6.** Bayesian model comparison using the [Madhusudhan et al. \(2023\)](#) data

Retrieval Model	Bayesian Evidence ( $\ln \mathcal{Z}$ )	Bayes Factor ( $\mathcal{B}_{\text{Ref}, i}$ )	Detection Significance	Classification
<b>No Offset</b>				
Ref.	28826.8	—	—	—
No CH <sub>4</sub>	28818.2	5541	4.5 $\sigma$	Strong Evidence
No CO <sub>2</sub>	28825.7	3.1	2.1 $\sigma$	Weak Evidence
No DMS	28825.6	3.2	2.1 $\sigma$	Weak Evidence
<b>One Offset</b>				
Ref.	28830.5	—	—	—
No CH <sub>4</sub>	28820.4	25848	4.9 $\sigma$	Strong Evidence
No CO <sub>2</sub>	28828.9	5.2	2.4 $\sigma$	Weak Evidence
No DMS	28830.2	1.3	N/A	No Evidence
<b>Two Offsets</b>				
Ref.	28829.9	—	—	—
No CH <sub>4</sub>	28819.6	30638	4.9 $\sigma$	Strong Evidence
No CO <sub>2</sub>	28828.0	6.4	2.5 $\sigma$	Weak Evidence
No DMS	28829.8	1.1	N/A	No Evidence

NOTE— $\mathcal{Z}$  is the Bayesian evidence of each retrieval,  $\mathcal{B}_{\text{Ref}, i}$  is the Bayes factor between the reference model and the nested model without molecule ‘ $i$ ’, and the ‘classification’ follows the Jeffreys’ scale (e.g. [Trotta 2008](#)).

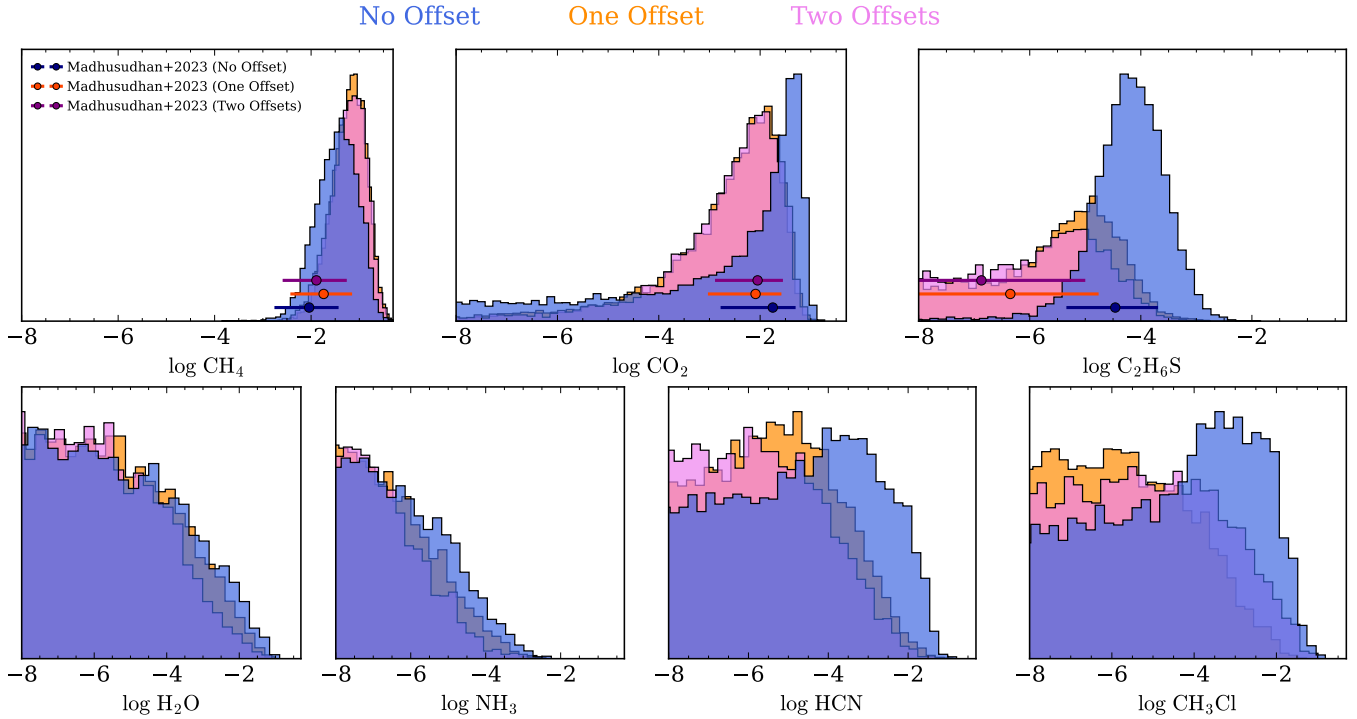


**Figure 14.** Reproduction of the results from [Madhusudhan et al. \(2023\)](#) using their full-resolution NIRISS + NIRSpec data. Retrieval results are overplotted for three retrieval models: (i) with no offset between NIRISS and NIRSpec (blue), (ii) an offset between NIRISS and NIRSpec (orange), and (iii) two offsets, one between NIRISS and NIRSpec G395H NRS1 and one between NIRISS and NIRSpec G395H NRS2 (violet). The statistically favoured retrieval model has a single offset. Our POSEIDON retrieval framework produces consistent results with [Madhusudhan et al. \(2023\)](#) when using the same priors and data. Any differences in detections for our other retrievals are therefore due to differences in data reduction rather than differences inherent to our retrieval approach.

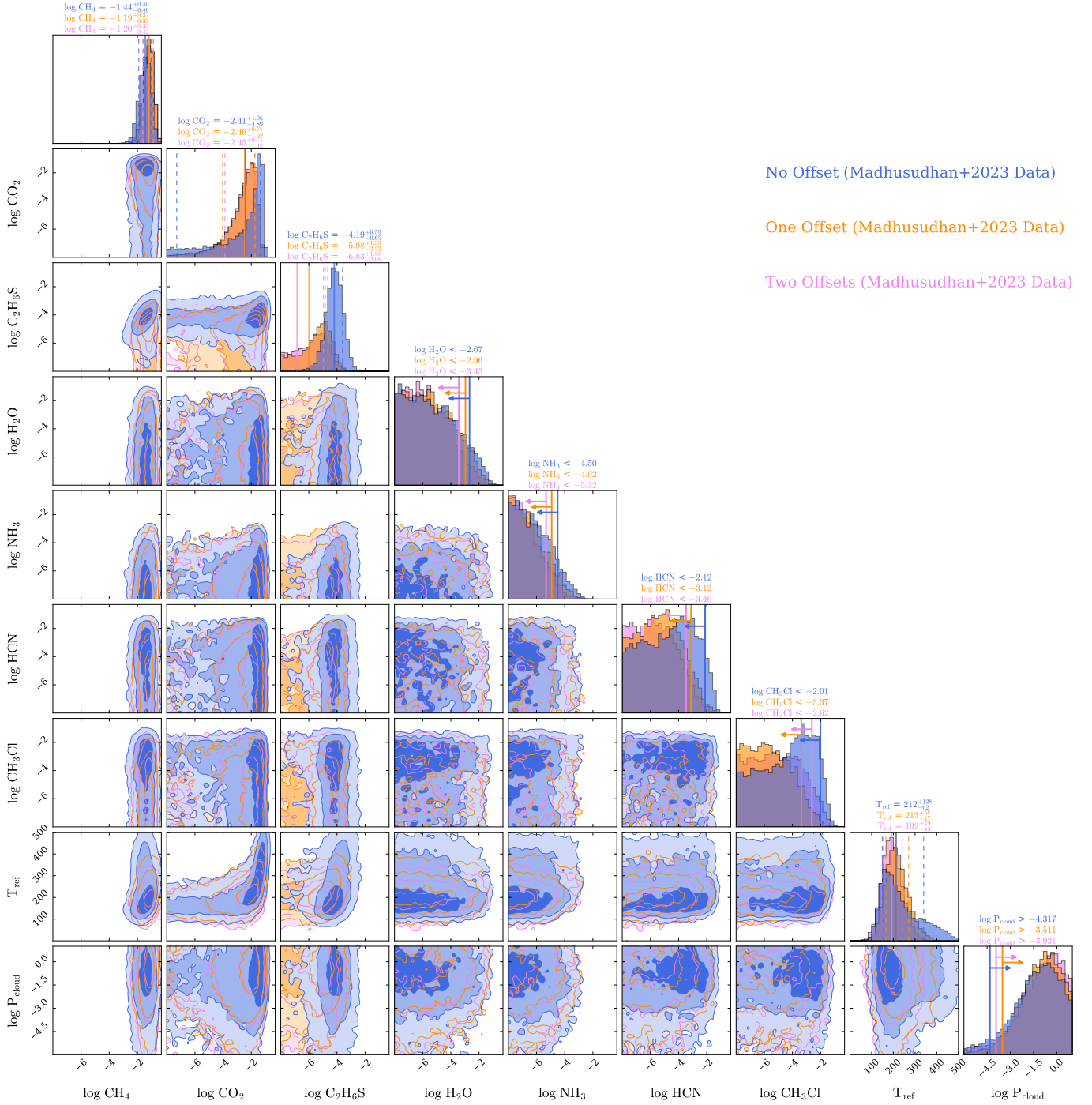


**Figure 15.** Corner plots corresponding to Figure 14, showing correlations between key atmospheric parameters. Parameters with only an upper or lower limit are marked by a vertical line and arrow at the 95% credible interval. We include  $1\sigma$  credible regions for  $\text{CO}_2$  and DMS, even though they are not robustly detected, for comparison with Madhusudhan et al. (2023).

## B. SPECTROPHOTOMETRIC LIGHT CURVE FITS WITH FIREFLY

Here we present the spectroscopic light curve fits and residuals for our  $R \approx 100$  FIREFLY reduction. We show the NRS1 fits in Figure 16 and the NRS2 fits in Figure 17. Additionally, we show the residuals of the NRS1 fits in Figure 18 and the residuals of the NRS2 fits in Figure 19. Each figure's panels all have the same x and y limits. The lack of trends in each bin demonstrates the fidelity of our spectrophotometric fits.

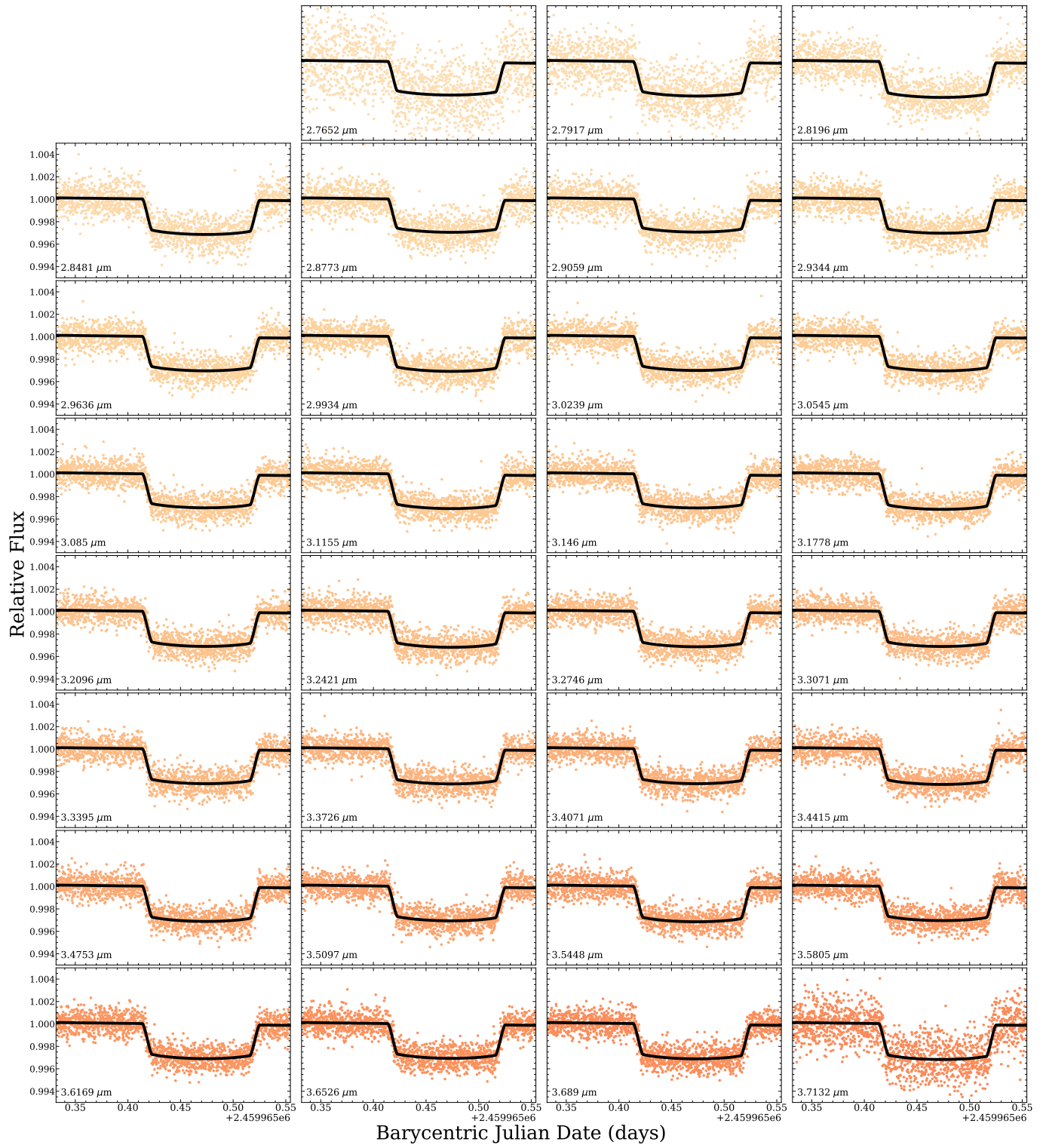


Figure 16. FIREFLY Spectroscopic light light curve fits for NRS1.

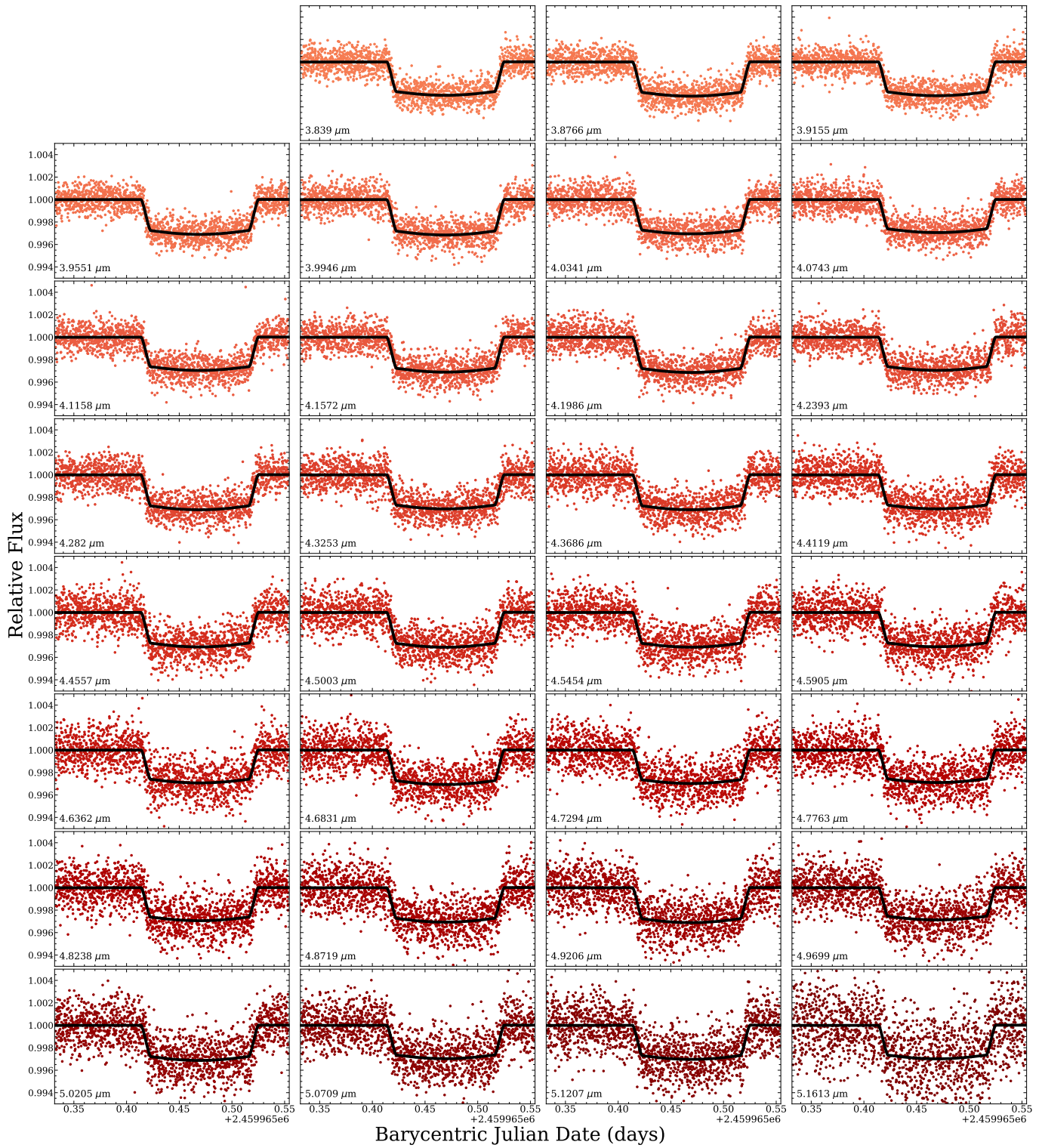


Figure 17. FIREFLY Spectroscopic light light curve fits for NRS2.

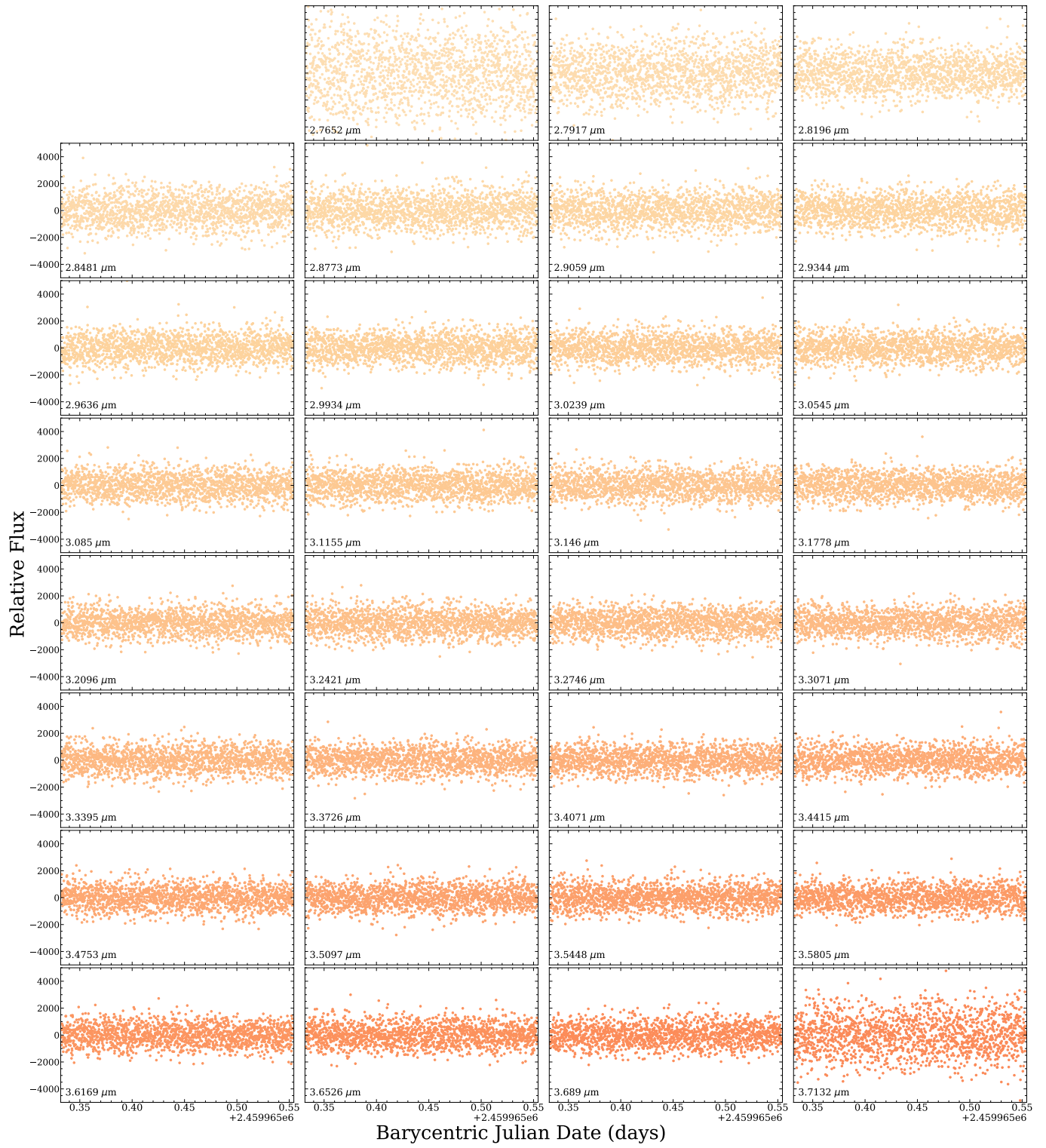


Figure 18. FIREFLY Spectroscopic light light curve residuals for NRS1.



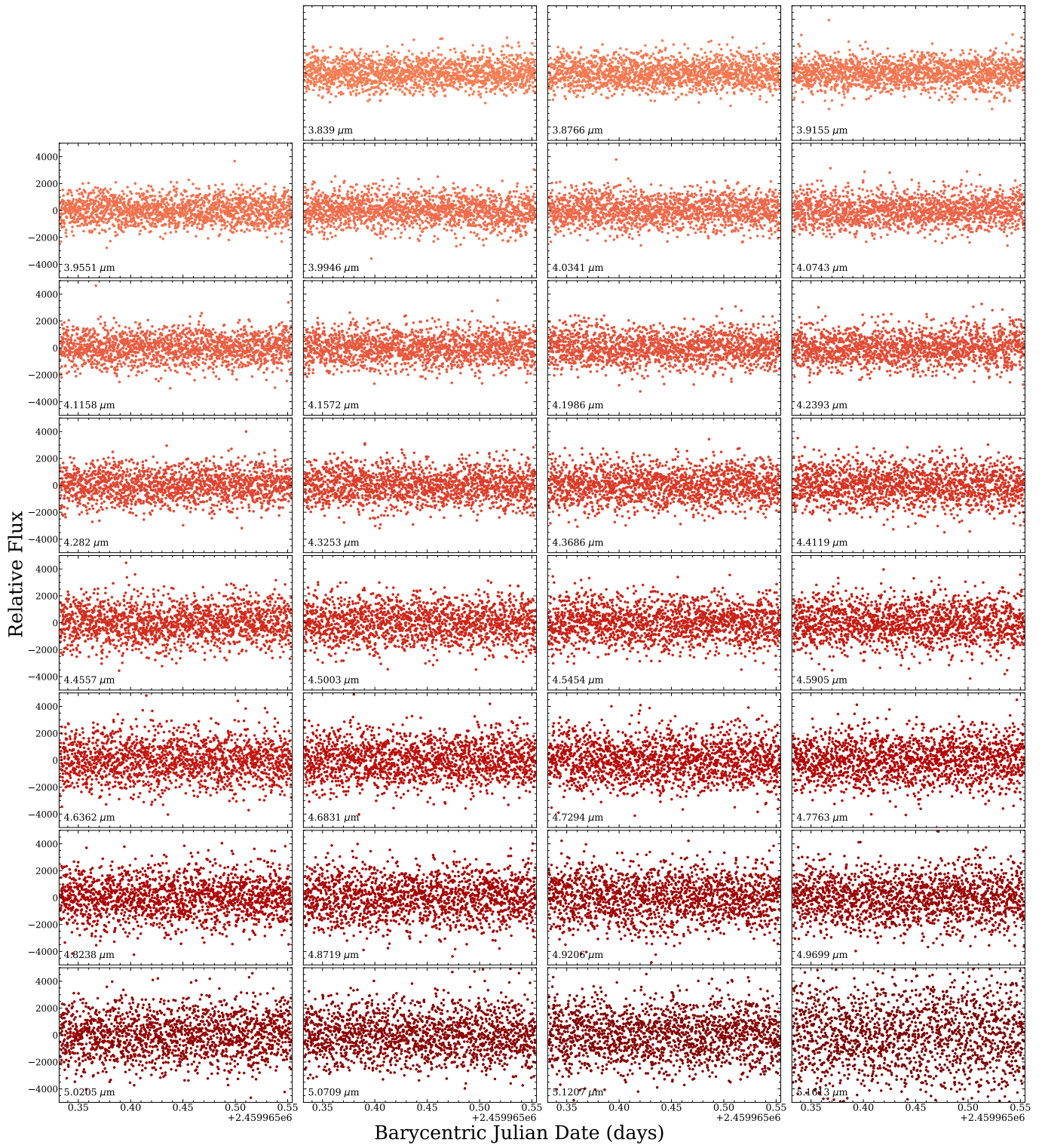
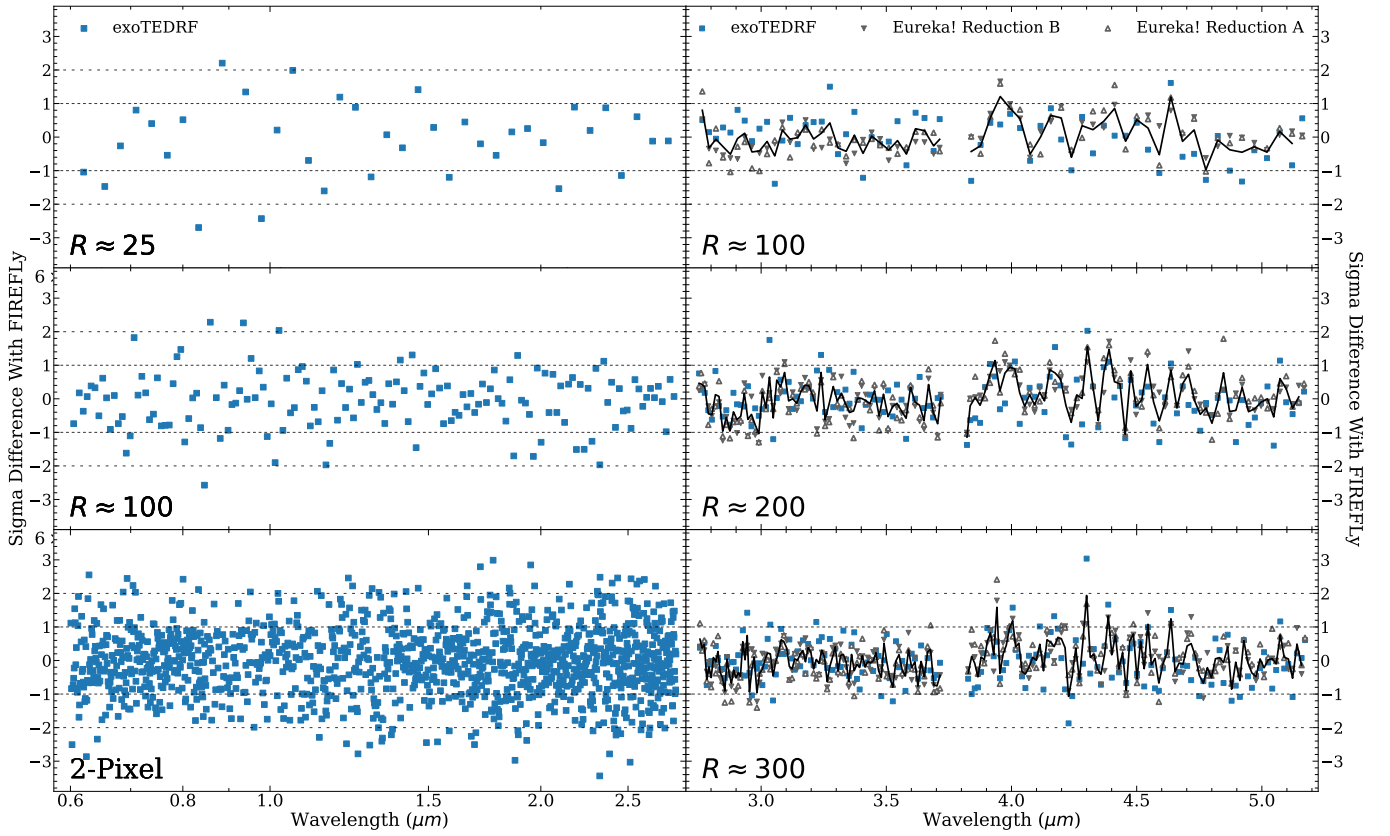


Figure 19. FIREFLY Spectroscopic light light curve residuals for NRS2.

## C. SIGNIFICANCE COMPARISON BETWEEN NIRSPEC AND NIRISS REDUCTIONS

For illustrative purposes, we perform an comparison between reductions in which we calculate the significance of the discrepancy in the transmission spectrum between the FIREFLY NIRSpec reduction and the other three reductions at  $R \approx 100$ ,  $R \approx 200$ , and  $R \approx 300$ . We do the same for NIRISS, but at  $R \approx 25$ ,  $R \approx 100$ , and 2-pixel binning. We show the results of this in Figure 20. We attribute the higher number of  $> 2\sigma$  outliers at shorter wavelengths between our  $R \approx 25$  NIRISS reductions to slight differences in our NIRISS binning scheme that are more pronounced there. Our reductions are consistent with one another, typically within a 1 to  $1.5\text{-}\sigma$  range of the FIREFLY reduction. The higher resolving power reductions have more outliers, but we expect this due to the larger number of data points. This indicates that the differing choices we apply in our reductions each yield consistent results and are reasonable for the purposes of marginalizing over in our retrieval analysis.



**Figure 20.** Significance of the discrepancy in transit depths between the FIREFLY reduction and the three other independent reductions. On the left three panels, we plot the significance between NIRISS reduction at  $R \approx 25$  (top),  $R \approx 100$  (middle), and at the 2-pixel level (bottom). On the right three panels, we plot the significance between NIRSpec reductions at  $R \approx 100$  (top),  $R \approx 200$  (middle), and  $R \approx 300$  (bottom). Using the same color scheme as Figure 3, we plot as blue squares the exoTEDRF reduction and as gray triangles the Eureka! reductions, distinguishing between the two with unfilled downward-pointing (A) and filled upward-pointing (B) triangles. We plot as a black solid line on the right three panels the average deviation between the three, and as gray horizontal lines the  $1\text{-}\sigma$  (densely-dashed) and  $2\text{-}\sigma$  (sparsely-dashed) cutoffs. Our reductions are consistent with one another, though the rate of  $> 2\sigma$  outliers increases with higher resolution.